ADVANCED MATERIALS
www.advmat.de

# Direct Laser Writing: From Materials Synthesis and Conversion to Electronic Device Processing

*Tomás Pinheiro,* Maria Morais, Sara Silvestre, Emanuel Carlos, João Coelho, Henrique V. Almeida, Pedro Barquinha, Elvira Fortunato,* and Rodrigo Martins**

**Direct Laser Writing (DLW) has been increasingly selected as a microfabrication route for efficient, cost-effective, high-resolution material synthesis and conversion. Concurrently, lasers participate in the patterning and assembly of functional geometries in several fields of application, of which electronics stand out. In this review, recent advances and strategies based on DLW for electronics microfabrication are surveyed and outlined, based on laser material growth strategies. First, the main DLW parameters influencing material synthesis and transformation mechanisms are summarized, aimed at selective, tailored writing of conductive and semiconducting materials. Additive and transformative DLW processing mechanisms are discussed, to open space to explore several categories of materials directly synthesized or transformed for electronics microfabrication. These include metallic conductors, metal oxides, transition metal chalcogenides and carbides, laser-induced graphene, and their mixtures. By accessing a wide range of material types, DLW-based electronic applications are explored, including processing components, energy harvesting and storage, sensing, and bioelectronics. The expanded capability of lasers to participate in multiple fabrication steps at different implementation levels, from material engineering to device processing, indicates their future applicability to next-generation electronics, where more accessible, green microfabrication approaches integrate lasers as comprehensive tools.**

## 1. Introduction to Laser Material Processing

Since the first developments in laser technologies that occurred in the 1960s,[1] great advances have been made in the capability of generating these coherent, monochromatic, directional electromagnetic radiation beams with different properties, including a wide range of radiation wavelengths, pulsing capabilities, temporal, frequency and spatial characteristics, and distinct energy profiles.[2] Accompanied by this progress, application areas for laser technologies also expanded, encompassing fields as distinct as communication, medical care, and analytical chemistry.[3] Concurrently, intense study on laser-material interactions has been in progress, opening new avenues for electronics microfabrication. The ever-growing demand for electronic devices and our societal dependency on these systems and their interconnectivity are leading to novel requirements that need to be considered at different implementation levels. On the side of materials, processing paradigms require compatibility with conventional rigid conductors, semiconductors, and insulators, but also present capabilities for processing mechanically flexible materials. With the increase in interconnectivity promoted by the Internet-of-Things (IoT), electronic devices need to be present in diverse settings, requiring mechanically robust, but flexible substrates, compatible materials, and manufacturing processes.[4] Even though several conventional microfabrication techniques for semiconductor devices and integrated circuits (ICs) fabrication, such as lithography techniques, chemical vapor deposition (CVD), and physical vapor deposition (PVD) methods, have shown great capabilities for flexible inorganic device manufacturing,[5] they are incompatible with many emerging electronic-grade organic materials and the paradigm shift from rigid to flexible electronics, due to high-vacuum and temperature requirements.[6] Several fabrication routes capable of increasing the range of processable materials and enabling large-area production using both rigid and flexible substrates have arisen. One such alternative is solution processing for thin film technologies,[7] which gives prospects for high processability and throughput, with expanded control of the

T. Pinheiro, M. Morais, S. Silvestre, E. Carlos, J. Coelho[+], H. V. Almeida, P. Barquinha, E. Fortunato, R. Martins
i3N|CENIMAT
Department of Materials Science
NOVA School of Science and Technology and CEMOP/UNINOVA
Campus de Caparica, Caparica 2829-516, Portugal
E-mail: tp.pinheiro@campus.fct.unl.pt; emf@fct.unl.pt; rfpm@fct.unl.pt

The ORCID identification number(s) for the author(s) of this article can be found under https://doi.org/10.1002/adma.202402014

[+]Present address: Departamento Física de la Materia Condensada and Instituto de Ciencia de Materiales de Sevilla, Universidad de Sevilla–CSIC, Avenida Reina Mercedes s/n, Sevilla 41012, Spain



**DOI: 10.1002/adma.202402014**

composition of processable solutions, while opening up routes for low-temperature processing. Great advances have been made using solution-processable techniques, including in thin-film transistors (TFTs),[8] resistive switching (RS) devices,[9] and solar cells[10] fabrication, among others. In addition, other fabrication technologies within additive manufacturing (AM) approaches have appeared as a good solution for fabricating several electronic component categories. These include batteries, solar cells, and other energy management applications,[11,12] as well as communication, sensing, processing, memory, and interface components.[13,14] Such technologies overcome the dependency on subtractive processes, circumventing the need for toxic etching chemicals, photoresists, and the wastage of deposited metals and semiconductors. 3D printing and its several modalities, including extrusion-based, vat polymerization and powder bed fusion processes have allowed for the manipulation of a wide range of materials, from metals to ceramics and polymers, both for layer fabrication as well as complex 3D geometries.[15] Alternatively, printed electronics have also been performed through planar printing processes, highly compatible with solution processability. Several printing modalities, including screen-printing, flexographic and gravure printing, and inkjet or aerosol printing, allow for layer-by-layer printing of conductor, semiconductor, and dielectric materials within complex planar geometries, as well as vertical layered devices.[16] Furthermore, these printing techniques can be a valuable resource for scalability, lower cost, and waste reduction, due to their compatibility with sheet-to-sheet (S2S) and roll-to-roll (R2R) manufacturing for large-area device fabrication.[6,16] However, for complex geometric patterns, some of these techniques have drawbacks since they need masters or plates for patterning. On the other hand, while 3D printing and inkjet printing are digital and allow for patterning with complex shapes and a wide range of resolutions, complex ink formulation and rheological control of printed material are required, while in some cases, multi-step post-processing is necessary.[17] Although solution processing and additive printing technologies have occupied an important part in flexible electronics fabrication, alternative techniques that further improve versatility and efficiency in large-area processing are sought after, capable of simultaneously performing multiple fabrication steps with energy, time, and resource efficiency, within multi-material processing systems. Lasers and their high-throughput material processing capabilities have amassed a great focus of research over the years, as a comprehensive resource to complement and substitute many manufacturing paradigms for more versatile approaches. The integrated capability of laser systems to participate in several fabrication stages, from synthesis,[18] doping,[19] polymerization,[20] and curing,[21] simultaneously with patterning,[22] and assembly,[23] has made laser technologies an important asset in material engineering and processing.

Relying on thermal-induced effects, the ablation capabilities of lasers have been extensively studied for the synthesis of nanostructures, such as metallic nanoparticles (NPs) or semiconducting quantum dots (QDs).[24] With the further coupling of control systems capable of directing laser beams, paired with computer-aided designing (CAD), many fields have taken lasers as reliable tools for manufacturing, both in subtractive and additive frameworks.[25] Hence, Direct laser writing (DLW) has appeared in several fabrication settings, which include micromachining, lithographic-based techniques, and 3D printing approaches. In this context, DLW can be distinguished into three categories, depending on the desired effect promoted by the interaction between the laser beam and processable materials and substrate. First, subtractive DLW (SDLW) relies on ablation and etching principles, by removing selective areas of deposited materials (**Figure 1a**), such as in photothermal ablation mechanisms for micromachining[26] or material drilling.[27] Second, additive DLW (ADLW), relies on several mechanisms aiming at synthesis and simultaneous patterning of material geometries, employing a precursor formulation (Figure 1b). This modality has been prolifically employed in 3D printing paradigms, such as in photon-induced polymerization reactions of photoinitiators and monomers, at the voxels created by focused beam paths.[28] Finally, transformative DLW (TDLW), is based on the direct irradiation of materials to transform their chemical or structural properties, without significant ablation and the need for external precursors (Figure 1c). Examples of transformative approaches include the crystallization of amorphous materials,[29] laser-promoted reversible structural transformations of carbon-based materials,[30] or laser doping of semiconductors.[19]

Some distinguishing features can be drawn between SDLW and the remaining processes. For ADLW and TDLW, the laser stimulus directly affects and dictates the resulting outcomes of irradiation over the processed substrate or precursor, in terms of its physical state, crystallinity, and other properties, such as mechanical resistance and electrical or thermal conductance. For SDLW, the purpose is only to shape the geometry and architecture of solid materials with pre-defined properties and functions.[31–34] This is fundamental for several processes, including geometry definition in micromachining, but also in cutting processes used for mask manufacturing or via hole establishment.[27,35] However, other techniques must be used to synthesize and deposit materials with pre-determined properties, also generating ablation waste. Thus, ADLW and TDLW present improved degrees of freedom for material processing, since manipulated laser stimuli provide tailoring capabilities for synthesis and conversion, while the writing and patterning tasks occur simultaneously. Additionally, not only solid materials may be engineered, but also aqueous precursor formulation, liquid polymers, and other material sources can be subjected to laser irradiation. Because of this versatility, ADLW and TDLW have increasingly been explored as an alternative to conventional physical and chemical deposition, as well as additive printing technologies in electronics. The plethora of different laser types and their associated beam properties results in advantageous features when selecting microfabrication approaches, related to material processability, device prototyping, fabrication throughput, and other relevant aspects. This is outlined in Figure 1d, where a comparison is drawn between several popular microfabrication approaches and their key characteristics. Even though lithography techniques (e.g., nanoimprint lithography) present outstanding resolution in the low nanometer range, several laser systems allow for sub-micron resolution, mostly the ones promoting two-photon absorption (TPA) and polymerization processes.[20] However, DLW achieves this resolution with improved material processability, throughput, and facile prototyping, due to the digital patterning capabilities. Conversely, DLW also improves some aspects when compared to

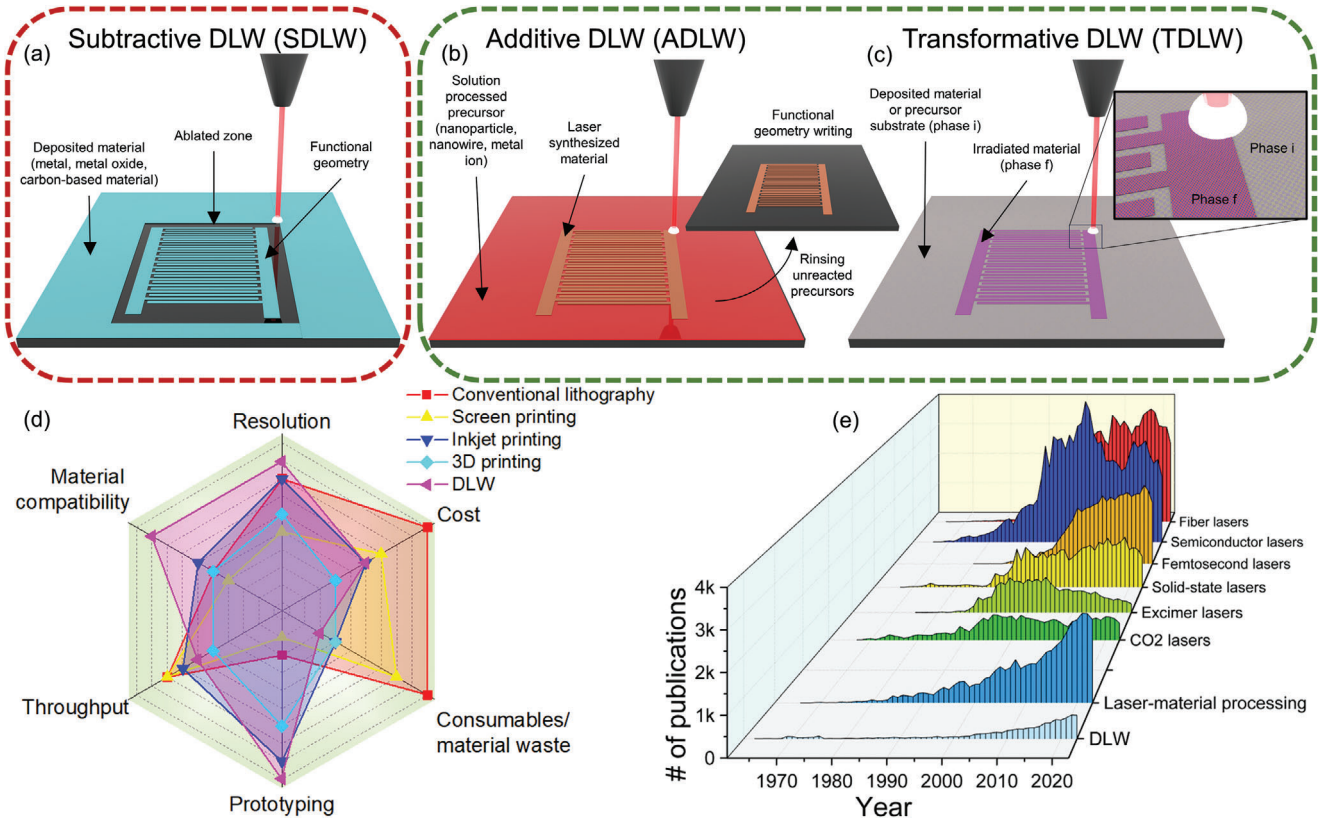


**Figure 1.** Modalities of DLW, comparison with established microfabrication technologies, and literature outlook. a) Schematic of subtractive DLW (ADLW) for ablation-based geometry writing. b) Schematic of additive DLW (ADLW) for simultaneous material synthesis and patterning. c) Schematic of transformative DLW (TDLW), characterized by selective chemical and structural material transformation. d) Spider chart comparing DLW with lithography techniques, inkjet, screen, and 3D printing, in relation to key fabrication and implementation characteristics. e) Scopus literature survey, portraying the evolution of publication for various laser systems, laser-material processing, and DLW.

printing technologies, namely the reduced consumable needs of laser systems at similar equipment costs, while also improving processability and prototyping, by incorporating several stages of fabrication in one-step processes. When studying multiparametric influences of fabrication variables in conventional fabrication strategies, such processes are strenuous and very resource and energy-consuming, while for laser systems, facile manipulation of irradiation and writing parameters is straightforward. This greatly improves the prototyping and implementation from lab to fab. Concurrently, most laser fabrication paradigms also present higher processability when compared to these printing techniques, since they are compatible with almost any type of material of interest for electronic device fabrication, from liquid precursors manipulated using solution processing, to direct solid substrate engineering. This high adaptability of lasers for very distinct tasks is represented by the immense exploration of their different configurations and capabilities in the scientific literature, presented in a literature survey portrayed in Figure 1e. The development of lasers with distinct gain medium or pumping operations has been ongoing for several decades, promoting the exploration of laser-based material processing and engineering for different purposes, reflected in the increasing interest of the scientific and industrial community in DLW paradigms.

In this review, we summarize and analyze recent progress in laser synthesis, conversion, and patterning paradigms for multimaterial electronics microfabrication by DLW (**Figure 2**).

Focus is given to ADLW and TDLW techniques and their ability to synthesize, convert, and write electronic-grade materials. Efficient synthesis, conversion, transformation, and writing of conductors and semiconductors for different purposes have been pursued, including for microelectronics, energy harvesting, storage, sensing, and integrated electronic and bioelectronic applications. Therefore, the fundamental principles of laser-material interactions for material engineering based on synthesis and conversion principles are explored, regarding the compatibility of distinct laser systems, their fabrication parameters, and the resulting capability to provide photochemical or photothermal stimuli. Furthermore, the most prevalent laser-material processing mechanisms within ADLW and TDLW and resulting concepts are discussed, in terms of their capability to synthesize and engineer materials with tailored properties. These include laser sintering of metal nanostructures and metal oxides, laser-induced reduction and oxidation reactions, and laser graphitization, among other photochemical and thermolysis mechanisms.

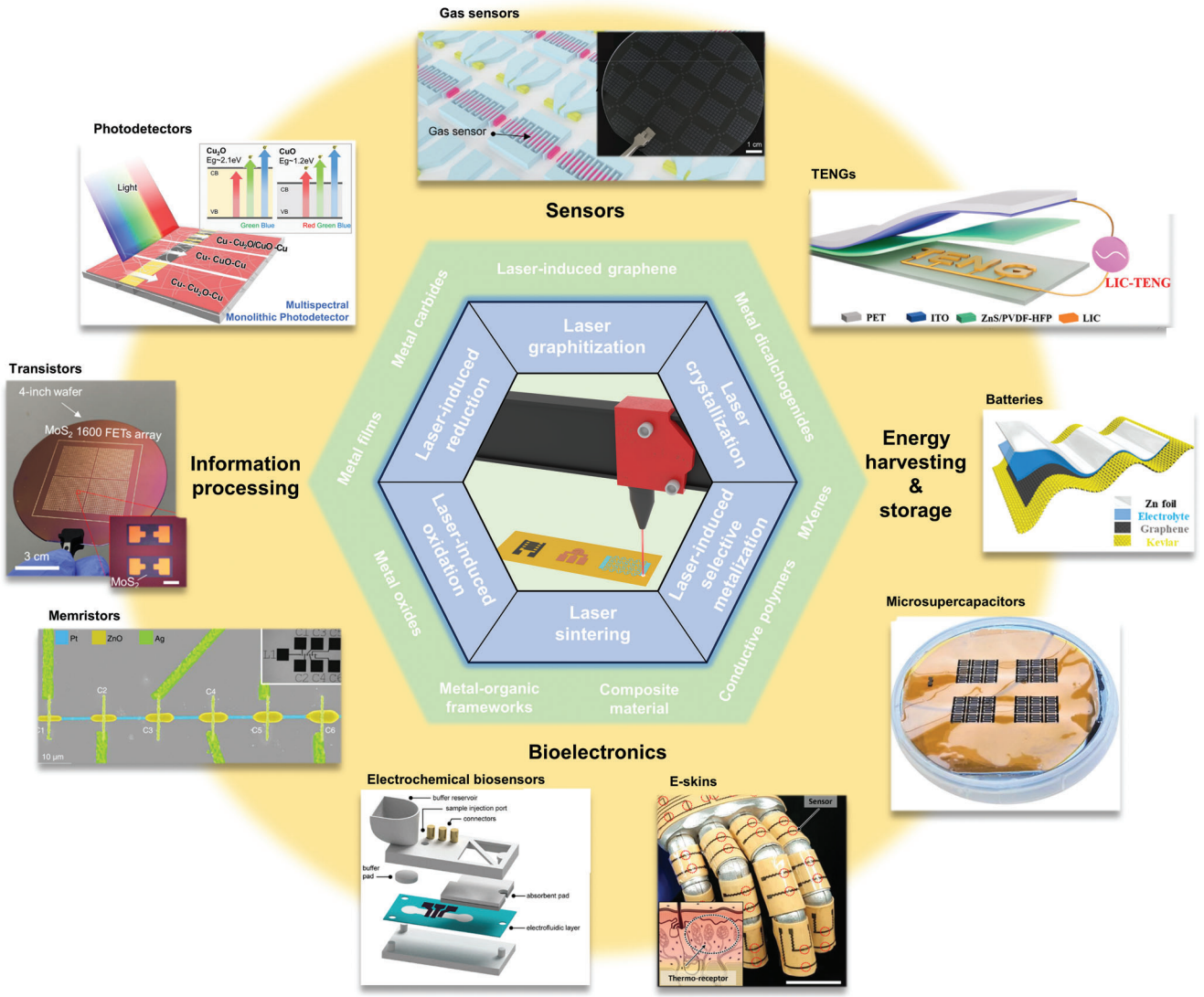


**Figure 2.** DLW mechanisms, synthesized materials, and applications for electronics. Image for "photodetectors". Reproduced with permission.[36] Copyright 2022, Springer Nature. Image for "gas sensors". Reproduced with permission.[37] Copyright 2022, Wiley-VCH. Image for "TENGs". Reproduced with permission.[38] Copyright 2022, Elsevier B.V. Image for "batteries". Reproduced with permission.[39] Copyright 2020, American Chemical Society. Image for "microsupercapacitors". Reproduced with permission.[40] Copyright 2019, Wiley-VCH. Image for "transistors". Reproduced with permission.[41] Copyright 2020, American Chemical Society. Image for "memristors". Reproduced with permission.[42] Copyright 2023, Springer Nature. Image for "electrochemical biosensors". Reproduced with permission.[43] Copyright 2023, Wiley-VCH. Image for "e-skins". Reproduced with permission.[44] Copyright 2019, Wiley-VCH.

## 2. DLW Principles for Electronics Microfabrication

### 2.1. Early Application of Lasers in Electronics Microfabrication

Regarding laser material processing in the setting of electronics, most of the early applications were developed within conventional, high-vacuum thin film deposition and machining approaches. A timeline of important breakthroughs and representative literature advances is presented in **Figure 3**. Some of the earliest applications were the machining and mask patterning for IC fabrication, using laser ablation principles.[45,46] DLW also found relevant use for laser lithography in these early stages, to expose photoresist coated substrates within microfabrication processes.[47] Other relevant uses of lasers were also found for the deposition of dielectric and semiconducting films, using laser-promoted evaporation of targets under high vacuum.[48,49] Moreover, another early application was the crystallization of semiconducting materials, including amorphous silicon, through laser annealing at lower temperatures, below the melting threshold.[50–52] Thereafter, pulsed laser annealing (PLA) and pulsed laser deposition (PLD) techniques have become very attractive for semiconducting material processing with much lower thermal budgets, capable of developing different functional homo and heterojunctions for applications such as diodes, TFTs, and solar cells.[53–56] Then, interestingly, some works demonstrated that thorough control of laser irradiation schemes and

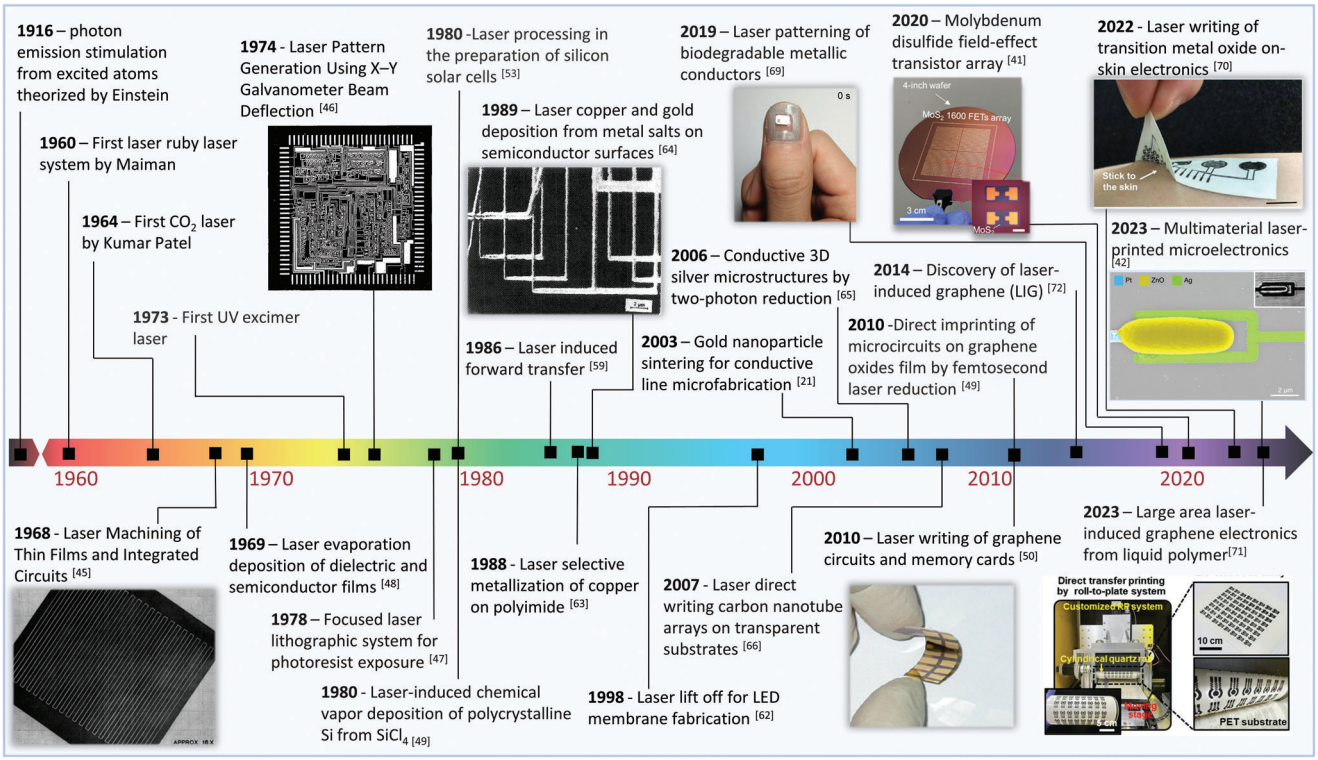


**Figure 3.** Timeline of breakthroughs and literature advances on laser-material processing in the framework of electronics microfabrication. Image for "laser machining". Reproduced with permission.[45] Copyright 1969, Wiley-VCH. Image for "laser pattern generation". Reproduced with permission.[46] Copyright 1974, Optica Publishing Group. Image for "laser copper deposition". Reproduced with permission.[64] Copyright 1989, AIP Publishing. Image for "laser writing of graphene circuits". Reproduced with permission.[68] Copyright 2010, America Chemical Society. Image for "biodegradable conductors". Reproduced with permission.[69] Copyright 2019, American Chemical Society. Image for "wafer transistor array". Reproduced with permission.[41] Copyright 2020 American Chemical Society. Image for "laser writing of transition metal oxide". Reproduced with permission.[70] Copyright 2022, AAAS. Image for "laser printed microelectronics". Reproduced with permission.[42] Copyright 2023, Springer Nature. Image for "large-area laser-induced graphene". Reproduced with permission.[71] Copyright 2023 Wiley-VCH.

resulting temperatures enabled solution processing frameworks with flexible polymeric substrates, such as polyimide (PI), without their thermal degradation,[54,57,58] opening the door for laser processing in flexible electronics. Besides these direct material-laser interactions, aiming at selective decomposition or phase shifts, other appealing techniques based on laser-induced transfer, printing, and assembly gained preponderance in electronics microfabrication. These rely on interfacial interactions between a donor material deposited over a transparent substrate, to transfer irradiated material geometries to a receiver substrate, such as laser-induced forward and backward transfer.[59–61] Another possibility is to use pulsed lasers with short wavelengths to perform laser lift-off techniques and separate support materials from rigid carriers, including lift-off of flexible substrates such as PI.[23,62] New paradigms of material processing for electronics have evolved over the years, taking full advantage of the capabilities of lasers for manufacturing.[63,64] Allied to their energy efficiency, lack of consumable needs and chemicals for processing, engineering of conducting, semiconducting, and insulating materials from different origins have created new opportunities to expand the range of techniques and processable materials employing more versatile approaches. An example is the production of metal lines and other geometries from metal salt precursors, by reduction mechanisms,[64] that also benefited from the development of TPA processes for 3D metal microstructure printing.[65] Other important metal processing mechanism using alternative material sources has been the laser sintering of nanomaterials, such as gold NPs.[21] The discovery of many carbon-based electronic grade materials, such as carbon nanotubes (CNTs) or graphene, opened new opportunities for flexible electronics processed by DLW, including controlled growth,[66] patterned reduction for graphene oxide (GO),[67] or ablation.[68]

Underpinned by these developments over the decades, recent developments on ADLW and TDLW for the synthesis of distinct materials have been developed, besides metal conductors and common semiconductors beyond silicon. For carbon-based materials, the direct irradiation of polymeric substrates has created the capability for producing a vast array of carbonized and graphitized conductors and semiconductors, where the discovery of laser-induced graphene stands out.[72] At the same time, advancements are being made for the laser synthesis of multifunctional materials employed for electronic device fabrication by ADLW and TDLW, including biodegradable metallic conductors,[69] transition metal dichalcogenide,[41] and several metal oxide semiconductors.[42,70] These synthesis and conversion paradigms are being employed in large-area fabrication, including wafer-scale arrays of transistors[41] and memristors,[42] as well as implementing laser-processed products within R2R

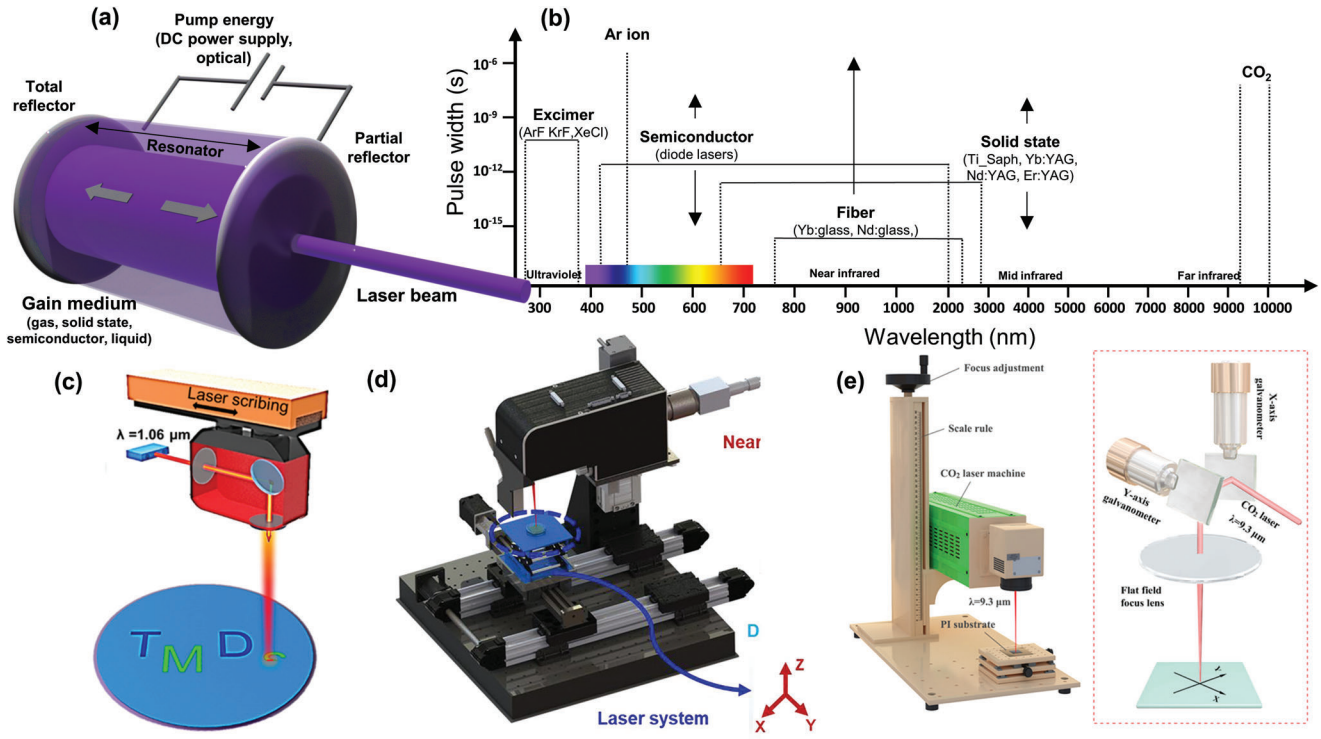


**Figure 4.** Schematic of laser setups for DLW microfabrication tasks. a) Representation of a generic laser source and its components. b) Graph relating wavelength and PW of common laser sources employed for DLW and material processing, depending on their gain medium. c) Representation of a scribing system based on moving optics system. Reproduced with permission.[41] Copyright 2020, American Chemical Society. d) Representation of a scribing system based on movable stage and static optics. Reproduced with permission.[75] Copyright 2022, American Chemical Society. e) Representation of a writing system based on the use of a galvanometer system. Reproduced with permission.[76] Copyright 2021, American Chemical Society.

manufacturing.[71] This demonstrates the ongoing attempt for large-scale, mass-production implementation of laser-processed electronics reviewed hereon, especially for flexible devices with novel architectures and more accessible material sources, crucial for the progressing IoT.[4]

## 2.2. Laser Systems and Operating Principles for DLW Microfabrication

Physical and chemical phenomena governing laser beam-material interactions are complex and depend on the multiparametric characteristics of laser beams and the absorption and thermal coefficients of irradiated materials. In this section, an overview of key fabrication factors is outlined, establishing some considerations for compatible laser systems and resources for DLW microfabrication paradigms, aiming toward customizable material properties, writing resolutions, and resulting functional material designs.

### *2.2.1. Laser Setups for DLW*

Laser systems are usually characterized by fundamental components in their setup. Depending on the active medium used as the radiation source, lasers can be divided into gas (e.g., $CO^2$ and excimer lasers), liquid (dye lasers), solid-state (e.g., fiber lasers), and semiconductor (e.g., diode) lasers.[2] Besides the laser gain medium, different configurations of pumping energy sources and resonators can be deployed (**Figure 4a**), to create laser beams with different characteristics, including wavelengths, energy levels, and time development. For radiation wavelengths, lasers mostly range from ultraviolet (UV) to far infrared (IR), leading to photons with corresponding energies according to Planck's equation: $E = h{\cdot}\nu$ (Figure 4b). For the temporal characteristics, laser systems can be divided into two main categories, namely continuous wave (CW) and pulsed lasers. While CW lasers emit steady beams with consistent energy characteristics over time, pulsed lasers allow for a train of individual pulses to be emitted with different pulse widths and frequencies. For example, $CO_2$ lasers are very limited regarding pulse width (PW) in the millisecond to microsecond range,[73] while other laser configurations allow for very short laser pulses in the pico to femtosecond range, using different pulsing strategies such as q-switching and mode-locking[74] (Figure 4b). For writing and patterning tasks, the optics systems that shape the laser beam must be coupled with control systems, capable of directing it at determined locations. Movable laser beams have been produced through several routes, each one relying on different hardware assemblies and their coupling with the laser source.

A common approach is to integrate mirrors and lens setups with motors that move them, while computer-controlled designs dictate when the laser beam is turned on or off (Figure 4c). These motion systems are common in many commercial flatbed laser

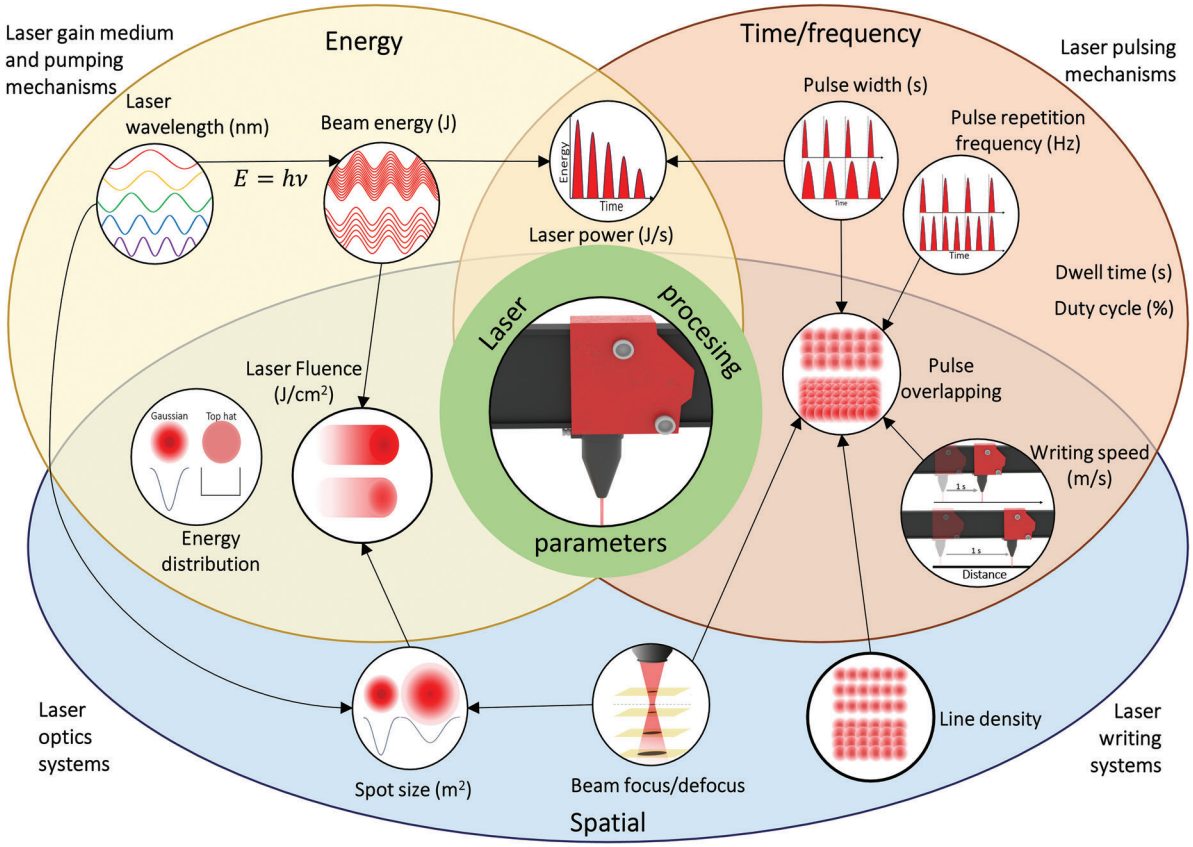


**Figure 5.** Scheme of DLW fabrication parameters in the energy, time/frequency and spatial domains and their interdependence.

cutting and engraving machines, that have been prolifically employed in DLW tasks.[77–81] Another alternative is the assembly of servo or stepper motors in linear configurations, to build translation stages that move the irradiated substrate, while the optics system is static (Figure 4d).[75,82–85] Both these approaches result in adequate processing speeds in the meter-per-second range. Besides motion systems, a different approach is the use of scanning systems, such as galvanometers,[18,76,86–89] that directly manipulate laser beam propagation direction towards selective locations, also allowing for higher processing speeds (Figure 4e). They can also be used to overcome some of the physical limitations of deflecting ultra-short pulse beams as well as high-frequency pulsed lasers.[90] In some cases, tilt stages are also needed in galvanometer-based configurations, to ensure a parallel irradiation surface.[86,87]

### 2.2.2. Fabrication Parameters for DLW Microfabrication

Depending on the characteristics of a laser system, control of laser material interactions and resulting irradiation outcomes is intrinsically dependent on fabrication parameters (e.g., power or writing speed, points per inch, or defocus value, among others). In turn, these parameters control physically significant variables, that dictate the type of phenomenon occurring during irradiation, such as photon flux or temperature accumulation over the laser irradiated surface. This is important since researchers can either use commercial or custom-made laser systems, digitally controlled through different fabrication parameters, that may not directly translate to physically meaningful variables (e.g., pulse power, pulse width, repetition frequency, or spot size). As such, physically meaningful fabrication parameters must be used in process-property studies, so that significant comparisons may be drawn between studies employing distinct laser systems or irradiation schemes.[91] Thus, an overview of energy, time, frequency, and spatial domain variables of laser operation and their interdependence is presented in **Figure 5** and variables are further explored in the following sections in terms of their importance in DLW fabrication tasks.

*Laser Wavelength*: Laser wavelength is a key feature determining the nature of reactions occurring upon irradiation of dissimilar materials. For lower wavelengths, such as in UV excimer lasers, the absorption of radiation is highly dependent on the chemical and electronic structure of irradiated materials, dictating the photochemical phenomenon occurring during irradiation. Low wavelength radiation usually presents higher absorptivity for organic materials and semiconductors, due to the resonant range of chemical bond energies or electronic band structures matching with the photonic excitation energy of the laser photons.[92] For organic materials, different phenomena can occur, including bond forming, isomerization, and breaking.[93] In the case of semiconductor materials, photon energy can differently stimulate the excitation of electrons and have other effects, including thermalization, carrier removal, and thermal and

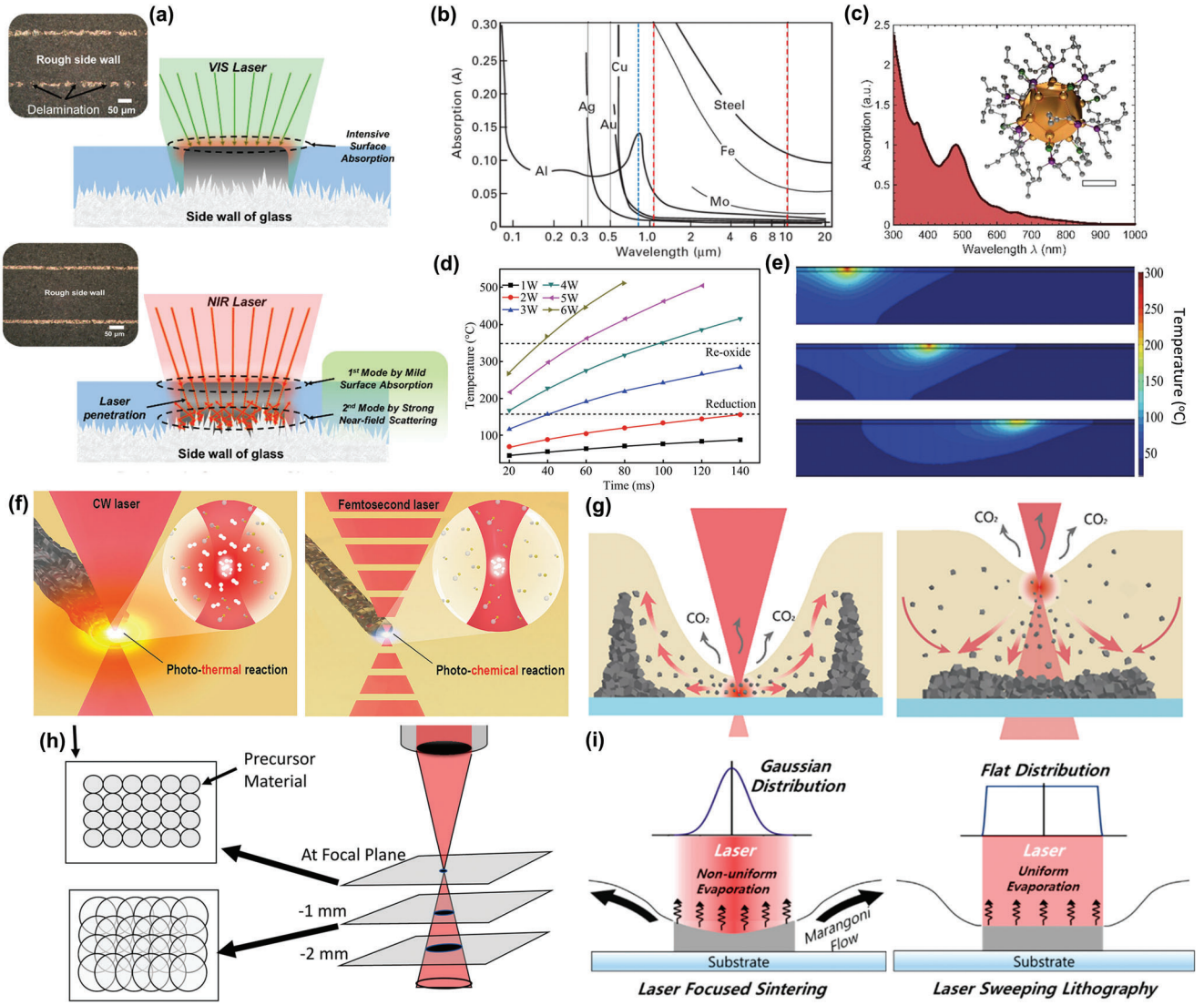


**Figure 6.** Influence of fabrication parameters on DLW laser-material interactions. a) Comparison of visible and NIR laser on their penetration depth, absorption, and scattering on a silver NP sintering model over a glass. Reproduced with permission.[101] Copyright 2020, American Chemical Society. b) Absorption spectrum of several bulk metals at specific laser wavelengths. Reproduced with permission.[97] Copyright 2021, MDPI. c) Representative absorption spectrum of a plasmonic gold nanocluster. Reproduced with permission.[102] Copyright 2023, Wiley-VCH. d) Influence of laser power and irradiation duration on reduction and oxidation outcomes of a copper metal ion precursor. e) Heatmap of temperature distribution for different writing speeds. Reproduced with permission.[103] Copyright 2017, Springer Nature. f) Schematic comparison of photothermal vs photochemical material processing depending on CW or femtosecond pulsed laser. g) Deposition profile of a transition metal dichalcogenide processed by DLW, depending on laser beam focus. Reproduced with permission.[18] Copyright 2022, American Chemical Society. h) Pulse spot overlapping profile of a $CO_2$ laser, depending on laser defocus degree. Reproduced with permission.[104] Copyright 2018, American Chemical Society. i) Comparison of Gaussian and flat top beam energy distributions and effects over silver NP sintering by DLW. Reproduced with permission.[105] Copyright 2018, American Chemical Society.

structural effects.[94] For higher wavelengths, lattice vibrations dominate the effects caused by photon energy absorption, leading to a preponderance of photothermal effects resulting in high energy accumulation and temperature increase. The promotion of phonons with high vibrational energies leads to the decomposition of several lower energy bonds while allowing for fast reorganization and structural transitions of irradiated chemical structures during thermal accumulation and after thermal relaxation.[95,96] Wavelength selection is also important to control beam penetration depth, influencing the thickness of processable materials and desired outcomes. This penetration depth ($\delta$) is expressed by: $\delta = \frac{\lambda}{4\,\pi\,k_e}$, where $k_e$ is the extinction coefficient of the material at a specific wavelength.[94] Generally, lower laser wavelengths lead to less penetration, increasing for higher wavelengths, although the absorptivity of materials at specific wavelengths influences these outcomes. This creates the need to optimize photon absorption by the irradiated material at distinct depths, either at the surface of the support substrate or at the surface of active irradiation layers (**Figure 6a**). This in turn impacts material deposition and pattern resolution. Thus,

studies on the transmission or absorption of irradiated materials are usually performed, to determine the suitability of specific laser wavelengths with the different target mechanisms for DLW, discussed in subsequent sections. While most bulk materials, such as metals, present low absorbances at most wavelengths above the UV (Figure 6b),[97] other metal micro and nanostructures or metal salt precursors present characteristic absorption profiles due to their chemical structure or plasmonic behavior (Figure 6c). Therefore, several processes based on multiphoton absorption (MPA) benefit from a considerate wavelength selection for optimal reactions and patterning outcomes.[42,98] Within these absorption processes, TPA is a powerful tool within laser-based material processing and microfabrication, used for 3D photolithography and photopolymerization, using photoresists and light-sensitive monomers, for high-resolution laser writing.[99] Because two photons are needed to induce efficient electron excitation of a target photosensitive material, their absorption is proportional to the square of light intensity ($I^2$), resulting in nonlinear processes, where photons must coincide in time and space. Thus, the sum of absorbed photon energies must be sufficient to cause excitation from a ground state to an excited state. Because of this, laser wavelength and associated photon energy for two-photon DLW (TP-DLW) must be lower than the energy difference (ΔE) between the electronic states, to avoid the occurrence of single-photon absorption (SPA) processes, that are linear and diminish high-resolution capabilities of the DLW process. Furthermore, laser wavelength also influences the spatial profile of focal units, usually called voxels, manipulated to achieve submicrometer resolutions.[100]

*Laser Energy and Power*: Laser power (Watts, J $s^{-1}$) is usually the most used metric in the energy domain, being given by differentiating the energy (Joules, J) of the laser beam concerning time. While in many cases the laser beam power is analogically controlled in the laser system, by modulating the gain medium pumping and output beam, some laser systems control the output power by pulse width modulation (PWM).[106] In these cases, the laser output energy is constant, and the resulting power is given by percentages of maximum power under continuous mode operation, depending on the pulse duration.[106] Thus, different energy profiles can be reached for the same absolute power output, depending on the employed laser system, and its power control mechanism. Regarding laser-material interactions, laser power is crucial to establish the threshold at which photochemical or photothermal effects are dominant.[107] Especially for low-wavelength lasers, lower power regimens lead to a preponderance of photochemical phenomena, due to the higher photon energy. With the increase of power, higher temperatures are promoted and can lead to desirable microstructural transitions and phase changes that can be temperature dependent. Depending on the laser power and time evolution of the irradiation process, different temperature-dependent mechanisms can occur, including reduction of the precursor, or re-oxidation of synthesized metallic structures, in case excessive energy is employed. (Figure 6d).[103,108,109] When surpassing the melting point, adequate power can lead to sintering and annealing processes for some metallic and metal oxide materials,[110] while allowing for photothermal-induced bond breaking and rearrangement in other processes, such as carbonization and graphitization.[92] If not properly controlled, high laser power can also lead to evaporation, sublimation, and ablation of irradiated materials, which in some cases is the desirable outcome for patterning.[33,111] In other cases, it can be an undesirable outcome, that indicates that excessive laser energy degraded the chemical or physical process being targeted. Hence, most process-property optimization methods report the outcomes or irradiation within power intervals against another variable of interest (e.g., writing speed, repetition frequency) to determine processing windows. Thus, laser power is not an independent variable and must be considered together with the time and spatially dependent variables that govern patterning tasks.

*Laser Writing Speed*: Laser writing speed (m $s^{-1}$) is highly dependent on the laser beam directing control systems described before, and greatly influences the accumulation of thermal effects promoted by laser irradiation. For CW lasers, writing speed dictates the fluence (J $cm^{-2}$) or irradiance (W $cm^{-2}$), since it directly establishes the dwell time of the beam over a unit of area.[112] For pulsed lasers, writing speed is also crucial to determine the overlapping rate of subsequent pulses, playing a critical role in many synthesis and conversion processes, as well as in patterning resolution.[113] As such, writing speed is usually used in conjunction with laser power, to control the energy dose subjected to the irradiated material and its areal distribution, as well as the resulting heat accumulation and dissipation effects. Usually, lower speeds lead to increased temperatures at the irradiation spot and higher heat accumulation at adjacent areas and in depth, while higher speed leads to less thermal accumulation, due to energy dissipation caused by the movement of the laser spot (Figure 6e).[103] Thus, many reports of process-property optimizations use power and speed pairs to determine useful processing windows, in opposition to undesirable outcomes such as ablation or incomplete reactions.[106,114–117] A final aspect regarding writing speed is the fabrication and production time. While writing speed has a relevant impact on photon and thermal-induced conversion and synthesis processes, it is relevant to optimize DLW processes for maximum speed, allowing for higher fabrication throughput, contingent that material performance is not compromised.[118–120]

*Pulse Width and Pulse Repetition Frequency*: PW (s) and pulse repetition frequency (PRF, Hz) are the two main variables in the time and frequency domains of pulsed laser irradiation and writing processes. Like writing speed, both have a great influence on photon flux and resulting energy and heat accumulation of individual pulses or subsequent pulse trains. PW can vary greatly, depending on the assembled laser system, going from milliseconds ($10^{-3}$ s) to femtoseconds ($10^{-15}$ s). Generally, PW dictates the time a pulse interacts with the material, and depending on this duration, the radial heat dispersion profile and penetration depth can be manipulated. This has implications not only on patterning resolution but also, in the photochemical or photothermal reactions that can occur during irradiation and their extent over the irradiated area. For CW lasers and short-pulsed lasers, energy accumulation is increased, and higher writing speeds are needed to ensure appropriate reaction conditions and microscale patterning. Ultrashort pulsed lasers allow for a more contained reaction environment, through the creation of reaction voxels[18] that promote photochemical reactions instead of thermal-induced processes (Figure 6f). More specifically, femtosecond lasers have gained great preponderance in TP-DLW micro and

nanomanufacturing paradigms based on photochemical reaction mechanisms, due to the non-linear and nonequilibrium phenomenon that can occur.[121] These processes rely on spatial and temporal photon overlap, showing the non-linear, quadratic dependence of electron excitation. These are greatly promoted using ultra-short pulsed lasers, mostly femtosecond lasers, that provide high photon flux and high peak power at low average power,[100] which increase the occurrence of TPA, diminish the occurrence of photothermal effects, and provide higher spatial resolution over the writing process.

Usually, ultrashort laser pulses are also coupled with the capability for high PRFs, in the MHz and GHz ($10^6$–$10^9$ Hz), to allow for material patterning in different settings.[122] In this regard, the duty cycle is an important metric since it establishes the relation between PW and PRF in terms of relative activation time over a pulsing period, and can be used as an optimization metric.[123] This duty cycle can be expressed as a fraction or percentage and is given by the expression: Duty cycle = $PW \times 1/PRF$. Knowing the PRF and energy of the laser beam, average laser power can be derived, by the expression: $P_{ave} = E_P$ x PRF, where $E_p$ is pulse energy. Inversely, pulse power is computed using pulse duration, employing the inverse relation: $P = E_P$ / PW. For some laser systems, PW and PRF may be manipulated directly in the control software. For some commonly used laser engraving systems, especially with PWM, they are expressed by pulse per distance metrics, such as pulses per inch (PPI).[77–81] In these cases, conversions are necessary, considering writing speed. For different writing speeds, PRF must vary, to ensure the same number of pulses occur in a set writing distance. In cases where PW and PRF are similar (duty cycle approximating 100%), there may be overlaps between subsequent pulse activations, giving rise to much higher thermal accumulation and an operation approximating a CW laser.[106]

*Laser Beam Focus and Spot Size*: Spot size and laser beam focusing are crucial variables in the spatial domain of laser writing processes. Laser spot size depends on two main components, namely the wavelength of laser photons and the optics system employed for beam shaping. For a Gaussian beam, laser spot size radius ($\omega$) can be calculated by the following expression: $\omega(z) = w_0\sqrt{1+\left(\frac{\lambda.z}{\pi\omega_0^2}\right)^2}$, where $\omega_0$ is the spot radius at focus and z is the relative distance to the focal point. It is noteworthy that spot radius at focus depends on the focal length, characteristic of the specific lens employed for beam shaping. Thus, irradiation spot size is directly controlled by the relative position of the optic lens system and the substrate surface. In a focused position, spot size is minimal, and the beam interacts with materials in its most condensed form. By varying this positioning, irradiation spot size can be manipulated and the laser beam can be focused on various positions relative to the processed material's surface or interface with a support substrate.[18,124] This, in turn, can have various effects on laser-material interactions. For example, when employing solution processing for materials synthesis from a thin precursor film, laser writing at different focal points can determine the architecture and shape of deposited materials (Figure 6g).[18] In turn, defocusing beam incidence also results in increases of beam spot radius. This directly dictates the energy density of a laser pulse, expressed by: Laser Fluence $= E_p/(\pi * \omega_z^2)$ (J cm$^{-2}$), where $E_p$ is pulse energy and $\omega_z$ is the spot radius. An increase in spot size also promotes the increase in subsequent laser pulse overlapping, alongside other variables previously discussed. For some writing and conversion processes, overlapping can be a determining variable in the quality of converted materials, as is the case of laser-induced graphene (LIG) synthesis (Figure 6h).[104] Defocus of the laser beam can also lead to either a convergent or divergent nature of laser photon paths, which can also influence laser-material interaction outcomes, even in cases of equal spot size.[106] It is also important to make some exceptions regarding alternative optic systems and their focusing capabilities. For galvanometer-based systems, the deflection of the laser beam requires lenses capable of focusing beams with different entry angles over a flat working surface. This is usually achieved using f-theta lenses,[86,87] which have distinct aspects when considering spot size calculations and fluence. Another factor is the energy distribution of laser beams. While most commonly, laser beams employed in DLW present a Gaussian distribution (TEM00), specific optical hardware can be implemented to achieve alternative beam energy profiles, such as a flat top energy distribution (Figure 6i).[105] In such cases, the beam energy is distributed differently over the laser spot area and can lead to different geometrical profiles of written patterns.

*Irradiation Atmosphere*: Although not directly related to laser operation, irradiation atmosphere is an important variable when performing DLW synthesis and conversion tasks. Usually, a choice must be made between performing DLW under inert conditions or an ambient atmosphere. Under inert atmospheres, film and substrate contamination can be avoided, while the absence of reactive volatiles suppresses the occurrence of possible oxidation or combustion promoted by the presence of oxygen.[125,126] These inert atmospheres are usually developed by permeating the working chamber with inert gases[125] or injecting these gases through a nozzle directed at the irradiated area,[127] being argon[29,126,128–130] or argon/$H_2$ mixture (95:5)[125,127] the most common choices. Other gases have been employed for atmosphere control in irradiation procedures, to accelerate certain reactions, for example, reduction, or to suppress plasma and exacerbated heat accumulation,[94] where nitrogen flow stands out.[77,80,116,131] However, the need for gas injection systems decreases the cost-effectiveness of the laser writing microfabrication procedures. Thus, ambient atmosphere irradiation schemes have been preferred, in cases where this is not detrimental to the synthesis and conversion outcomes.[37,41,69,70,132,133]

## 3. Mechanisms for Material Synthesis and Conversion Through DLW

Depending on the irradiated material and the laser characteristics, several interaction routes can be taken for laser synthesis and conversion processes using ADLW and TDLW. This section is dedicated to key synthesis and conversion mechanisms, that have been used individually or in combination, to produce conductive and semiconductor patterns from several inorganic and organic precursors and substrates, suitable for integration into electronics and bioelectronic systems and devices.

### 3.1. Laser Sintering

Selective laser sintering has been a common mechanism used in AM, targeting several material sources, from metals, ceramics, and polymers in powder forms, within 3D printing frameworks.[134] For microfabrication purposes, laser sintering has mainly been employed with micro or nanostructured material sources, ideal for higher resolution patterning of conductors and semiconductor formulations. Typically, solution-processed films consist of metal or metal oxide NPs, additives, and surfactants mixed in a solvent, whose presence tends to increase resistivity values.[135,136] Sintering is a commonly used approach to degrade unwanted organic phases, as well as increase particle percolation, leading to continuous films or geometries with more efficient electron flow capabilities and reduced resistivity.[135,136] Several alternatives have been explored for thermal sintering, including plasma, electric current, photonic, and flash techniques.[135] However, most of these require higher temperatures to achieve efficient film percolation and widespread sintering, while also not supporting simultaneous patterning, which must be done beforehand. Laser sintering within DLW frameworks is an ideal approach since the delivered heat can be confined to the specific beam area,[135] enabling the composition and property control of sintered films, according to specific requirements and regions.[17] Laser sintering for metal processing has become a straightforward alternative to access high-resolution writing of conductive lines and other geometries, not only improving film conductivity but also adhesion to support substrates. Besides glass,[101,102,105,137] other compatible substrates have been used, including semiconductor wafers ($Si/SiO_x$,[102] ITO,[137] and GaAs),[138] ceramic surfaces,[139] and several flexible substrates (PI,[102,137,140–142] PET,[143] PEN,[144] TPU,[145] and paper).[141,146] Different noble metal NP sources and other particle morphologies have been targeted, including gold,[21,102,147] silver,[101,147,148] and platinum.[139,147] Other transition metals have also been explored for laser sintering approaches including nickel,[149] copper,[87] and some of their oxide forms,[136] although not limited to these metal classes. Zinc macro and microparticles are also promising for laser sintering processing,[69,150,151] as well as other metals, such as aluminum.[152]

Laser sintering is dependent on the optical properties of the precursor film and its composition, specifically its absorption of laser radiation.[136] Specifically, the plasmonic behavior of nanostructures promotes the use of resonant laser wavelengths for maximum energy absorption, in the visible to near IR range,[102,136] while minimizing substrate radiation absorption. During this process, a neck between adjacent particles is formed, followed by surface-to-volume reduction due to particle aggregation, with the extension of this process over the DLW treated area, as represented in a gold patterning DLW method in the schematic of **Figure 7a**. In the first stage, focused laser beams lead to a decrease of interfacial energy between NPs due to photothermal effects, promoting rapid neck formation between adjacent particles.[153] Depending on the laser energy dose, irradiation time, and most importantly, the resulting temperature, neck growth occurs (Figure 7b). This neck growth process can be promoted by several material transport processes, including Ostwald ripening, and surface and grain boundary diffusions. These processes have been extensively studied using molecular dynamics simulations,[140,154] aiding empirical experiments. Generally, these simulations show the very rapid neck formation in several metal NP systems, in the picosecond time range (Figure 7c). If temperature is kept constant, equilibriums are reached regarding neck size. However, an increase in laser energy dose and temperature promotes neck growth, until limits delineated by the size of the particles in a pair system (Figure 7d).[154] Associated with this interparticle neck growth, there is a direct influence on the degree of resistivity decrease (Figure 7e), common for several target metal nanostructures.[140,155] Continued neck growth leads to densification of the material and closing of pores between adjacent particles, as shown in Figure 7f for a sintered track of AgNPs employing a femtosecond laser.

Notably, in this work by Noh et al.,[148] femtosecond laser sintering occurs without melting, with sintered structures retaining the original crystallinity of AgNPs. For higher power regimens and increased pulse width, melting can lead to recrystallization after thermal relaxation, inducing polycrystallinity in the sintered structure.[135,148] Thus, ultrashort pulsed lasers have been preferred over longer PW lasers and CW lasers, allowing for higher control of neck growth, melting, and recrystallization processes.[153] Additionally, the temperature increase in the laser-irradiated area must be enough to efficiently promote the degradation of organic species and solvent evaporation. Laser-sintered films can commonly present swelling effects, due to entrapped volatiles. This is common in sintering processes with thicker precursor films, that require repeated irradiation for sintering within film depth. Usually, initial laser pulses cause the formation of superficial sintering, while subsequent pulses promote the same phenomenon at increasing depths. The repetition of this process leads to the degradation of organic compounds and solvent evaporation, which ultimately form vapors entrapped within the film and ununiform patterns (Figure 7g).[135] To circumvent some of these effects, a synergistic control of precursor film deposition conditions and irradiation scheme is needed for improved outcomes. An example is presented in Figure 7h, where the control of the deposition rate of a polyurethane/silver ink using a syringe printing process leads to lower thickness in the deposited precursor film, which in turn leads to more uniform laser sintered films. Besides precursor preparation, process-property optimization of power, writing speed, and other fabrication parameters are subsequently needed, to achieve improvements in film conductivity as shown in the graph of Figure 7i, where lower temperature accumulation associated with increasing writing speeds leads to less efficient sintering and the resulting increase in resistivity.

### 3.2. Laser-Induced Reduction

Laser-induced reduction is a commonly used technique to pattern conductive layers in flexible substrates through photon-induced chemical reactions. Within this DLW modality, several principles have been proposed for the capability to reduce metal ion species into metallic NPs, followed by continued deposition, growth, and structure writing. The first possibility is the occurrence of MBA and TPA principles, that allow for electron excitation in precursor solutions and films, leading to NP nucleation (**Figure 8a**).[124,156] For this to happen, high photon flux

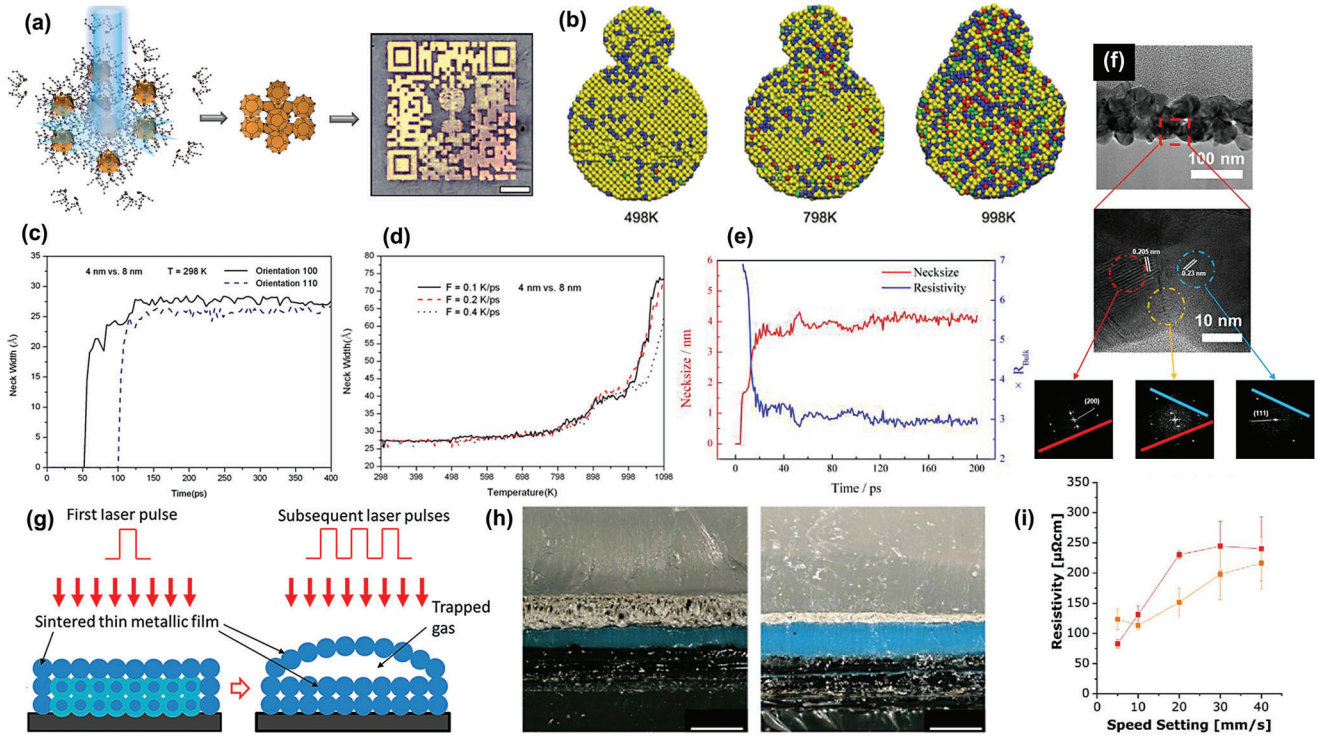


**Figure 7.** DLW sintering mechanisms for nanostructure precursors. a) Schematic of gold NP DLW sintering mechanism. Reproduced with permission.[102] Copyright 2023, Wiley-VCH. b) Snapshot of molecular dynamics simulation of neck formation and growth at different temperatures for a 4 and 8 nm gold NP pair system, corresponding neck width evolution over time (c) and for increased temperatures (d). Reproduced with permission.[154] Copyright 2011, Springer Nature. e) Relationship between neck width and resistivity. Reproduced with permission.[140] Copyright 2020, Elsevier B.V. f) Transmission electron microscope images and selective area electron diffraction patterns of femtosecond laser sintered silver NPs. Reproduced with permission.[148] Copyright 2020, Elsevier B.V. g) Schematic of vapor entrapment in laser sintering processes. Reproduced with permission.[135] Copyright 2019, American Chemical Society. Cross-section of sintered film with different thickness, resulting in different sintering uniformity (h) and effect of laser writing speed on resistivity values of sintered silver films (i). Reproduced with permission.[145] Copyright 2021, IOP Publishing.

lasers are needed, and absorbed photon energy must be enough to excite electrons from the ground to an excited state and promote reduction. In these cases, TPA phenomenon translates to two-photon reduction (TPR) mechanisms,[118,156] in opposition to other mechanisms outside the scope of this review, such as two-photon polymerization. This process can either directly affect the precursor metal ions,[98,157] or occur through a photoinitiator or other excitable component within a precursor formulation, that transfers electrons following photon-induced excitation, acting as photoreducing agents (e.g., photoresists,[158] sodium citrate,[159] semiconducting structure).[160] Commonly, TPR also requires ultrashort pulse laser systems, most commonly femtosecond lasers, capable of providing the high photon flux stimulus needed to initiate photoreduction.[121,156,159] Also depending on the photosensitizer, SPA can be responsible for laser-induced reduction.[161] Alternatively, the use of laser systems with lower photon flux (e.g., laser with higher PW and CW laser) for reduction relies on photothermal activation of formulations made from the metal ion and reducing agents. The thermal stimulus and decomposition of reducing agents or solvents promote the necessary electron transfer and subsequent reduction of the metal ions, leading to the nucleation of nanostructures at the irradiated surface.[124] Following nucleation, both continued photon absorption or photothermal mechanisms, such as Joule and plasmonic heating, lead to the growth of nucleated nanostructures and their aggregation at the laser focal point, by local depletion of metal ions, to form continuous films and patterns throughout the irradiation path. For efficient DLW processes, the focal point must be focused on the surface of the deposition substrate, to allow for the patterning of adhered microstructures, in opposition to irradiation product deposition or NP formation throughout the aqueous precursor solution (Figure 8b,c).

Furthermore, in cases where irradiation is performed in metal ion-rich liquid phases, microbubble formation occurs and heat-induced flows, such as Marangoni convection, further promote the accumulation of metal ions in the irradiated area, allowing for continual writing (Figure 8c).[124] However, other formulations using gelatine matrices have also been employed.[162,163] Several metallic salts have been used for this purpose, including metal nitrates, chlorides and acetates, such as $AgNO_3$,[42,147,163–167] $AgClO_4$,[158,162] $Cu(NO_3)_2$,[82,103,115,160,164,168–171] $Cu(CH_3COO)_2$,[172] $HAuCl_4$,[40,147,173,174] $PtCl_4$,[42] and $NiCl_2$.[147] Regarding reducing agents, polyvinylpyrrolidone (PVP) is a common choice, whose decomposition produces formic acid, able to reduce metal ion species.[87,115,164] Sodium citrate has been the main resource used in laser photon or thermal-induced reduction of silver

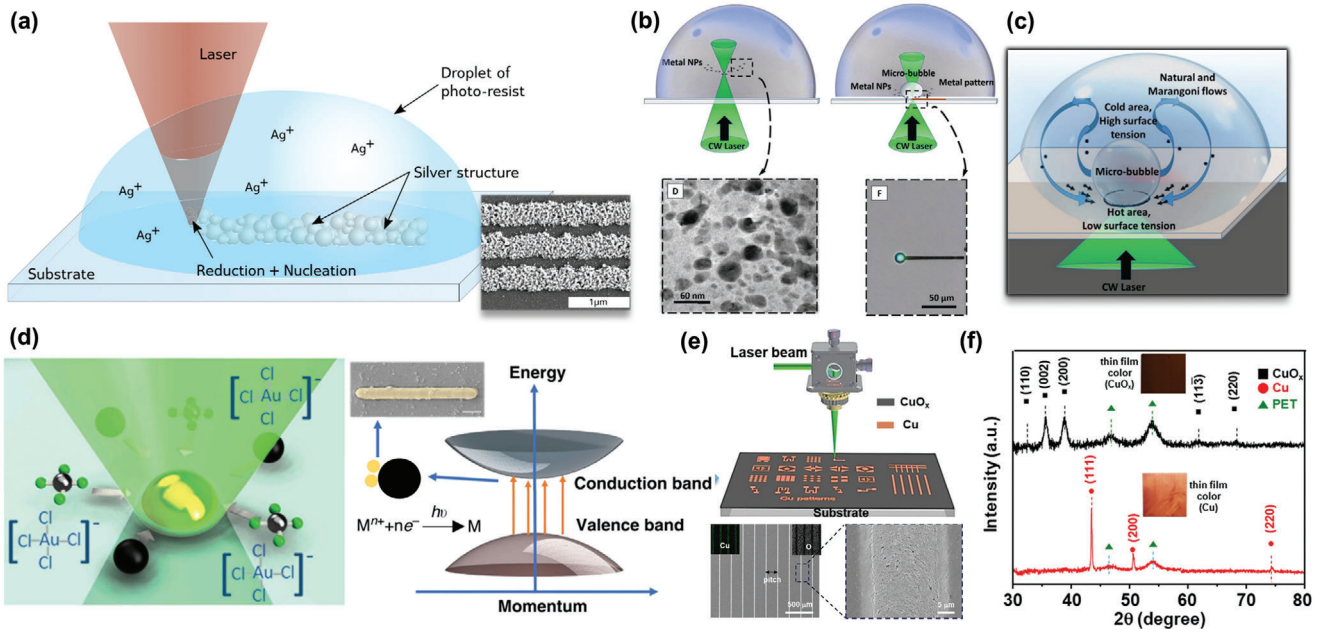


**Figure 8.** Laser-induced reduction mechanisms employed in DLW microfabrication. a) Laser-induced reduction of silver promoted by a photo-resist initiator and resulting conductive tracks. Reproduced with permission.[158] Copyright 2021, American Chemical Society. b) Effect of focal point positioning on the nature of laser-synthesized structures and c) representation of Marangoni flow and renovation of precursors over the irradiation path. Reproduced with permission.[124] Copyright 2019, Wiley-VCH. d) Laser-induced reduction of metal ions over semiconductor NP photoinitiators. Reproduced with permission.[147] Copyright 2020, Springer Nature. e) Laser-induced reductive sintering of copper oxide NPs to form metallic copper patterns and XRD spectra of copper oxide precursor and resulting laser-reduced copper. Reproduced with permission.[87] Copyright 2021, Elsevier B.V.

ions.[158,166] Another reported mechanism for the formation of metallic films involves the use of semiconductor NPs as reducing agents.[147,173,174] Upon laser exposure, the electrons in the valence band are promoted to the semiconductor's conduction band, promoting the reduction of metal ions at their surface. Simultaneously, the laser beam is also proposed as an optical trap, that drives the semiconductor NPs toward the irradiation path, leading to robust writing of metal/semiconductor composite patterns (Figure 8d).

Another common mechanism based on reduction principles is the use of metal oxide NPs as metallic precursors. This method has been adopted for several transition metals, using $CuO_x$,[36,38,87,175–178] $NiO_x$,[86,149,179] $CoO_x$,[180] as well as NP mixtures.[181,182] This mechanism is based on mixing oxide NP precursors with similar reducing agents (e.g., PVP,[38,87] ethylene glycol),[36,182] while laser irradiation and resulting photothermal processes promote the removal of oxygen over the metal oxide NP structure. Alongside reduction agents, photothermal excitation of these semiconductor structures can excite electrons into the conduction band, aiding in reduction initiation.[179] Since the precursor is also in a nanostructure form, most of these writing processes are also associated with sintering, leading to a process named reductive sintering of NPs,[36,87,181] that allows for an efficient percolation and continuous conductive film (Figure 8e). In addition, control of the irradiation process is key to achieving efficient oxygen removal and synthesis of metallic patterns, in opposition to metal/metal oxide mixtures, due to incomplete reduction, usually tracked by X-ray diffraction (XRD) (Figure 8f). Similar laser-induced reductive processes were also developed for removing oxygen functional groups from GO. These processes have been extensively reviewed in the literature[183] and are not explored in this review.

### 3.3. Laser-Induced Oxidation

Laser-induced oxidation was performed for the first time in thin chromium films to produce chromium oxide. The films were exposed to radiation with a fluence lower than the evaporation thresholds, leading to laser-induced chemical reactions and resulting patterns that remained visible over time, depending on humidity. It took 6 months to attribute the patterns to laser irradiation, and the laser-induced oxidation process was only understood in the following 6 months.[184] Laser oxidation can be applied for selective oxide fabrication.[185] The fundamental processes of this phenomenon are chemical reactions and oxygen diffusion (**Figure 9a**).[133] Laser irradiation occurs in an oxygen-rich environment, so chemical reactions between the metallic film and oxygen are promoted, leading to its oxidation. Then, a metal oxide layer with the desired pattern is formed.[37,185–187] In sum, laser-induced oxidation comprises five main steps: i) absorption of energy at the film surface causing a temperature rise, ii) adhesion and dissociation of oxide molecules to the substrate's surface, iii) nucleation of subatomic layers, iv) transportation of particles (both metal and oxide) within the oxide layer and growth of the newly formed layer.[188] The energy absorbed by the films directly affects their temperature and, consequently, their degree of oxidation.[189] Particularly, through the variation of parameters such as laser wavelength, power, exposure time, irradiation atmosphere, and focusing details, it is possible to tailor the

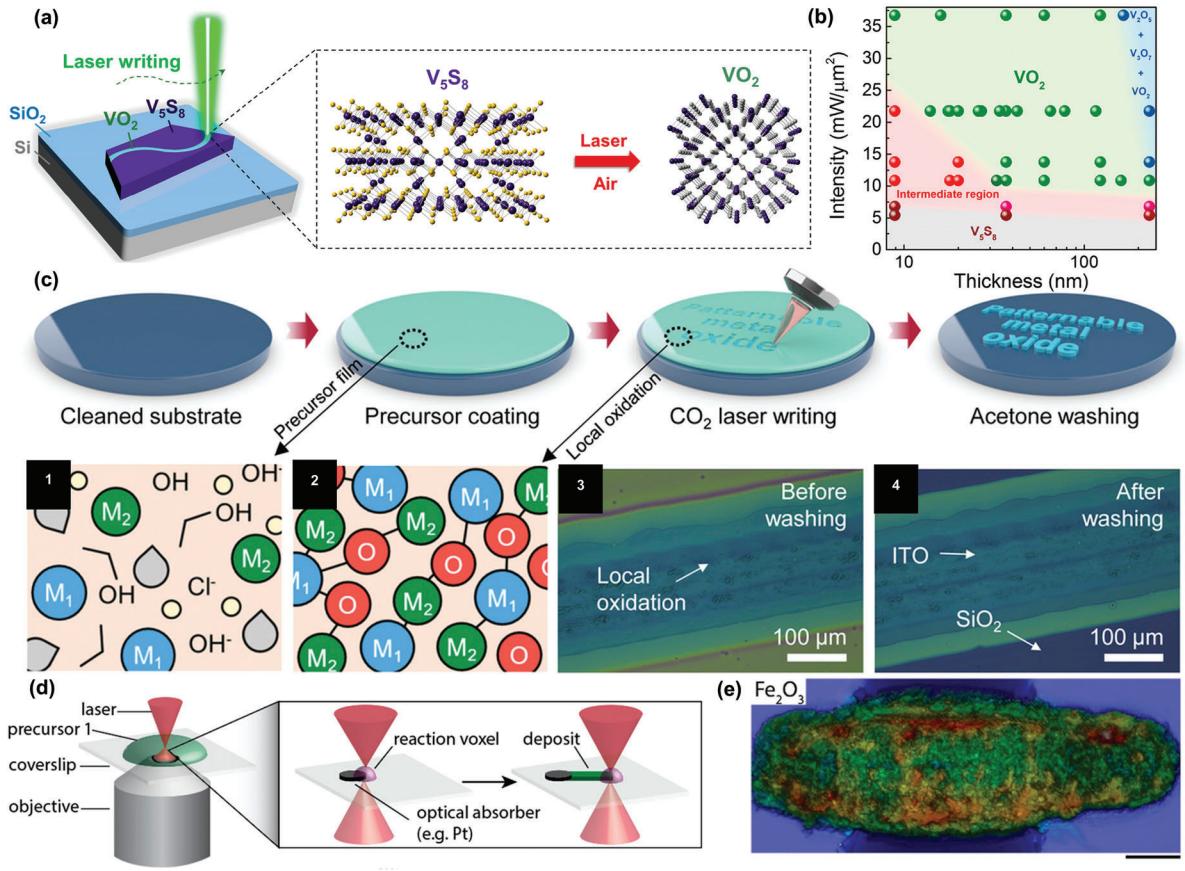


**Figure 9.** DLW mechanisms for selective laser-induced oxidation. a) Laser-induced oxidation of vanadium sulfide films in ambient atmosphere to synthesize vanadium oxide patterns. b) Regions of oxidation into different vanadium oxide species depending on precursor film thickness and laser intensity. Reproduced with permission.[133] Copyright 2021, American Chemical Society. c) DLW oxidation of solution-processed precursor. 1) Precursor film made of metal ions precursor and solvent. 2) Permeation of oxygen and metal oxide synthesis promoted by laser irradiation. 3) Metal oxide patterning prior to precursor washing. 4) Metal oxide (ITO) pattern after washing of precursor phase. Reproduced with permission.[37] Copyright 2022, Wiley-VCH. d) DLW metal oxide synthesis from solution precursor by solvothermal decomposition. Reproduced with permission.[191] Copyright 2019, American Chemical Society. Resulting $Fe_2O_3$ line written by laser-induced solvothermal decomposition. Reproduced with permission.[186] Copyright 2022, American Chemical Society.

properties of the oxide layer, namely, roughness, geometrical form, adhesion properties, thickness, and crystallinity. The spots where crystallization starts depend on the energetic distribution of the laser beam.[187] It is worth noting that laser-induced oxidation is a non-linear process and occurs in nonequilibrium circumstances, as there is a temperature gradient within the oxide film resulting from variability in the coupling processes between the laser beam and substrate. The chemical reaction rates depend not only on the film temperature but also on other laser parameters.[188] Also, as the oxidation film's thickness increases, the oxidation reaction kinetics start being diffusion-limited and not reaction rate-limited.[133] Laser-induced oxidation can be applied to oxidize films to different oxides of the same metal, where one oxide can be preferred over another, depending on the laser input power (Figure 9b).[133,187]

Besides DLW for laser-induced oxidation of deposited metal films, solution processing of precursors has also been recently explored as a more accessible route for oxide synthesis and writing (Figure 9c). Similarly to the laser-induced reduction of metal salt precursors, metal ions (e.g., $MoCl_5$,[70] $Cu(NO_3)_2$,[115,186] $Zn(NO_3)_2$,[42,186] $ZnCl_2$,[37] $FeCl_3$,[190] and $SnCl_4$,[186] amongst others) can be used in formulations without reduction agents. Under ambient, oxidative atmospheres, laser-induced growth, oxidation, and writing of metal oxide patterns are achieved. In these cases, denitrogenation and dichlorination occur by laser-induced thermal decomposition (Figure 9c(1)) before oxygen diffusion throughout the metal oxide chemical structure (Figure 9c(2)).[37] After laser-induced oxide synthesis and writing, the removal of unreacted precursor films is needed to reveal the DLW-produced geometries (Figure 9c(3,4)). These precursor formulations can also be used in the aqueous phase, where the creation of laser-induced thermal voxels (LITV) promotes the oxidation of several metal oxide species for microscale patterning directly using the precursor solution, by solvothermal decomposition processes that generate oxide NPs, followed by their growth and sintering (Figure 9d).[186,191] This allows for faster metal oxide patterning, when compared to other techniques, such as laser-induced hydrothermal growth (LIHG), another mechanism used for oxide nanostructure synthesis and writing.[192,193]

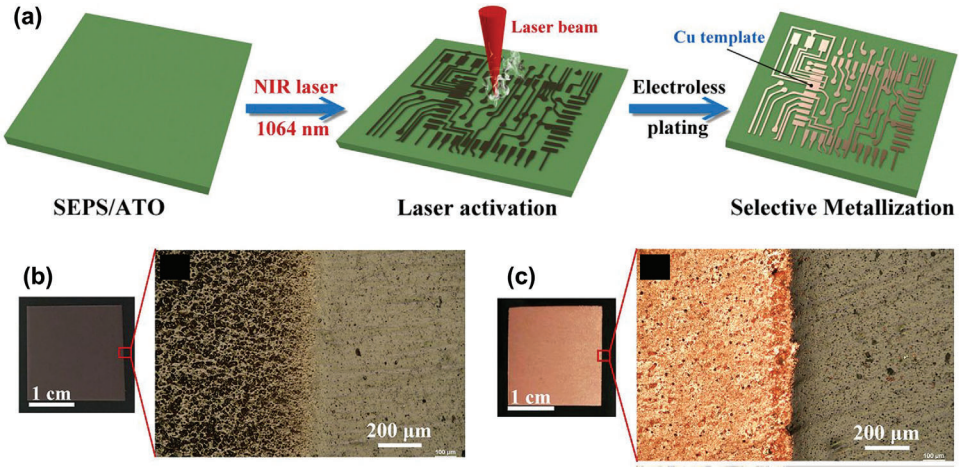


**Figure 10.** DLW activation of substrate for LISM processes. a) Steps in LISM process of an activated SEPS/ATO substrate using a NIR laser (SEPS as substrate material and STO as activator). b) resulting activated pattern and its microtopography. c) Resulting copper film after copper electroless plating. Reproduced with permission.[194] Copyright 2022, American Chemical Society.

### 3.4. Laser-Induced Selective Metallization

Although not a DLW technique for direct material synthesis and patterning, laser-induced selective metallization (LISM) has been a widespread resource for writing activated patterns over substrates of interest. LISM encompasses three main steps: substrate material preparation, laser activation, and electroless plating (**Figure 10**a). Substrates are usually composites, made of a polymer matrix and a laser sensitizer.[194] For activation, laser sensitizers absorb energy, decomposing into species that activate certain substrate areas for electroless plating reactions.[195] There are two types of laser sensitizers, depending on the mechanism leading the metal production. The first mechanism is based on the reduction of a metal precursor. The activated patterns usually present rough micro-topographies and disperse metal particle seeds, which become active centers for electroless plating (Figure 10b). The second mechanism is based on the catalytic activity of the sensitizer towards the electroless plating process.[196] According to the literature, copper aluminum oxide,[197] ethylenediaminetetraacetate,[198] copper hydroxyl phosphate,[199] multiwalled CNTs,[200] copper oxalate,[89] copper–chromium oxide,[201] molybdenum trioxide,[196] and antimony-doped tin oxide (ATO)[202] can be used as sensitizers. In alternative to the incorporation of sensitizers within the substrate matrix, laser activation can also be performed with the substrate immersed in a sensitizer solution. Particularly, Ren et al. performed LISM of silver NPs on a PI substrate, where the catalytic layer presents a porous structure enhancing the stability of the electroless plating.[75] The advantage LISM is the straightforward capability to write activated patterns in a myriad of substrates, including glass,[203] PI,[75,204] polyurethane (PU),[198] polyamide (PA),[205] polypropylene (PP),[200] polybutylene terephthalate (PBT),[206] polyvinyl butyral (PVB),[207] polystyrenes,[89,194,196,208,209] polydimethyl siloxane (PDMS),[83,195,196,210] Ecoflex,[201] cement,[211] ceramics,[212,213] and 3D printed resins.[214] It is worth mentioning that although most works report the use of 1064 nm wavelength lasers, other laser systems are also compatible with the LISM process, including $CO_2$,[207] UV,[208] and femtosecond lasers.[83] This process has been most notably employed to produce copper functional patterns, after copper sulfate electroless plating (Figure 10c), although other approaches have been reported for the electroless plating of other metals, such as nickel[204] or layered metal structures.[196]

### 3.5. Laser Carbonization and Graphitization

Laser carbonization and graphitization are similar mechanisms, related to the irradiation of carbon-based precursors, resulting in photothermal effects caused by lattice vibrations and heat accumulation. High temperatures promote the cleavage of bonds, with the release of oxygen-rich volatiles, while most of the carbon fraction of the material reorganizes, also due to photothermal effects. This reorganization is both dependent on the imposed temperatures of the laser irradiation scheme and its time evolution, where different irradiation schemes, resulting temperatures, irradiation atmosphere, and other factors influence the extent of reorganization of native chemical bonds onto pristine, crystalline hexagonal lattices, with minimized atomic defects (**Figure 11**a).[215] This distinguishes processes that lead to carbonization and graphitization, where, more amorphous, less crystalline carbon forms are synthesized for carbonization, while the evolution of this process over time leads to structures with a higher degree of graphitic stacking. Synthesis principles are similar for both mechanisms, in which carbon bonds are converted from their original hybridization to $sp^2$-rich chemical structures, through aromatization and condensation processes. Ultimately, this leads to the build-up of graphene lattices in organizations analogous to graphite, with similar interlayer distances (3.37 Å) (Figure 11b), but more defective atomic carbon-bond organization at the lattice level. (Figure 11c).[95] Regarding the microstructure of carbonized and graphitized materials of different origins, the release of volatiles leads to the formation of porous 3D structures, where cross-section analysis is usually employed to determine the effect of the irradiation toward the thickness and

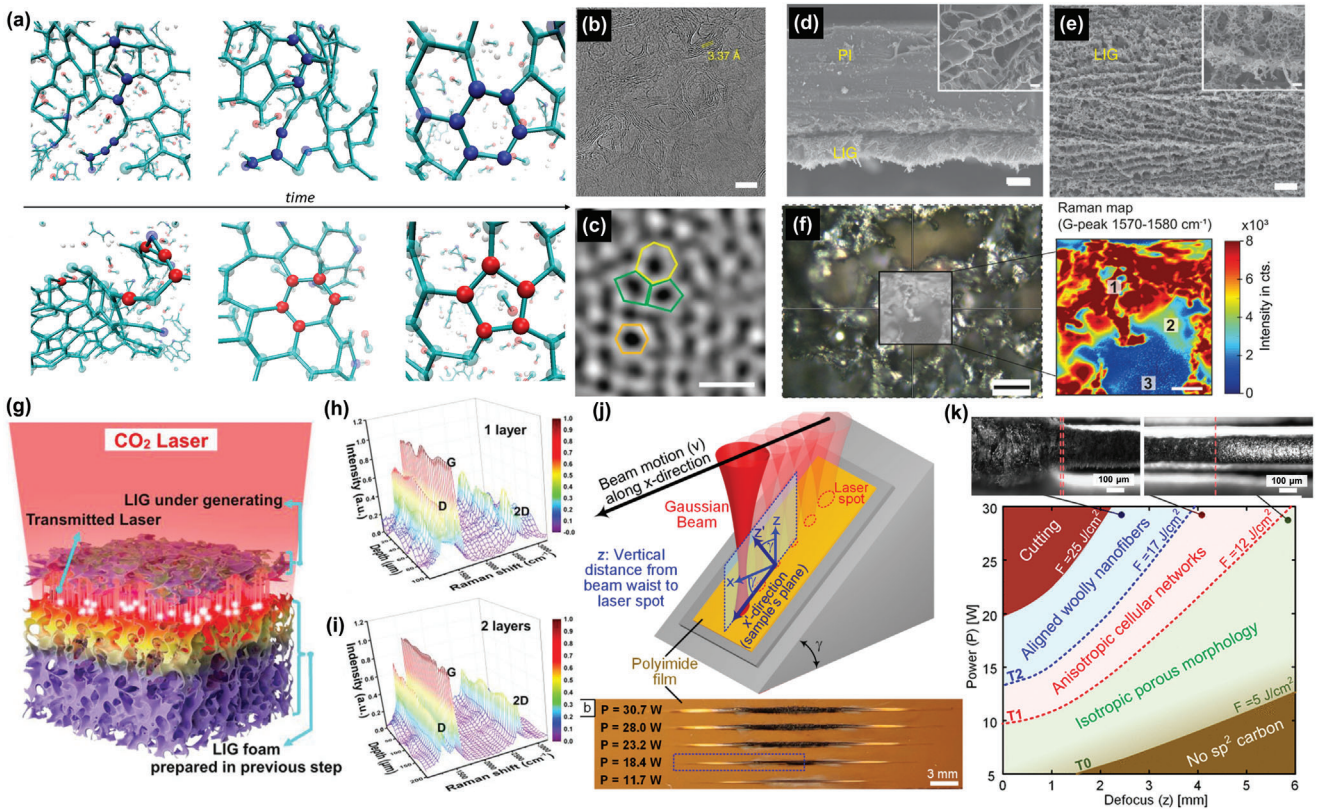


**Figure 11.** DLW for laser-induced carbonization and graphitization. a) ReaxFF molecular dynamics simulations of PI carbonization/graphitization over time and the distribution of pentagonal and hexagonal carbon arrangements. Reproduced with permission.[215] Copyright 2020, American Chemical Society. Transmission electron microscope images of LIG for b) interlayer distance and c) carbon atom lattice distribution analysis. Scanning electron microscope images of LIG d) cross-section and e) distribution of porous material over the laser beam irradiation path. Reproduced with permission.[72] Copyright 2014, Springer Nature. f) Raman spectroscopy mapping of a wood-derived LIG surface and the distribution of G peak intensities. Reproduced with permission.[217] Copyright 2022, Springer Nature. g) Layered synthesis of LIG from a polyether sulfone precursor and the distribution of chemical properties in depth, surveyed by Raman spectroscopy for h) 1 precursor layer and i) 2 precursor layers. Reproduced with permission.[218] Copyright 2023, Wiley-VCH. j) Laser beam defocus method for spot size and laser fluence selection. k) Dependency on laser power and defocus distance toward morphological transition levels. Reproduced with permission.[108] Copyright 2021, American Chemical Society.

architecture of formed graphitic layers (Figure 11d). In the perpendicular axis, there is usually a distribution of the material accompanying the laser beam path (Figure 11e). In cases where there is the presence of other inorganic phases, carbonization processes can also promote the synthesis of metal carbide materials, with the carbon fraction participating in carbothermal reduction mechanisms.[216,217]

Laser carbonization of PI has been observed as far back as the 1980s,[219] using argon-ion lasers. However, these techniques took traction when James Tour's research group reported, in 2014, an alternative for the synthesis of 3D porous graphene resulting from the conversion of PI when exposed to far-IR $CO_2$ laser irradiation.[72] Although $CO_2$ lasers are the tool of choice for carbonization and graphitization,[72,79,217,220,221] other laser sources have shown compatibility, including UV[222–225] and visible lasers.[226,227] For these lower wavelength sources, authors report the concurrent occurrence of photochemical processes,[228] although they are not sufficient to cause efficient carbonization and graphitization, which is mainly promoted by temperature-induced effects.[229,230] The resulting material was labeled LIG, although other names have been used in the literature, including laser-engraved graphene (LEG)[231] or laser-scribed graphene (LSG).[232] Since then, tremendous progress on conversion and patterning mechanisms of PI and other precursors has occurred, regarding conversion mechanisms, material property optimization, and the multiple fields of application.[233–236] Depending on the chemical structure of precursors, different graphitization potentials result from the abundance of aromatic chemical structures within a precursor, while for substrates without aromatic chemical moieties, different modification strategies are needed to ensure efficient carbonization and graphitization strategies. For synthetic aromatic polymers, such as PI and polyetherimide (PEI), DLW leads to direct graphitization, contingent that laser irradiation schemes provide sufficient temperature stimuli.[72,215] For aliphatic materials, such as several abundant biopolymers, substrate modification strategies that improve thermal resistance are needed. Appropriate laser systems that present higher control of temperature accumulation profiles can also be used.[95] Contingent on the chemical formulation of precursors and laser irradiation schemes, tailored properties of resulting graphitized materials are possible, aiming at improved defect densities, crystalline size, electrical conductivity, and overall morphology.

Being a 3D graphitic material with significant porosity, control of the overall chemical properties of LIG throughout the irradiated area and film depth is also important, usually being surveyed in many process-property experiments. This optimization has been mainly performed using Raman spectroscopy, to determine chemical characteristics of LIG over material topography. In the work by Dreimol et al., mapping of Raman peak distribution over wood-derived LIG showed improved graphitization in more superficial areas, exposed to higher temperatures (Figure 11f). Because of these differences in depth, novel strategies have appeared in the DLW graphitization paradigm, designed to synthesize more uniform LIG in all directions. An example is the work by Song et al.,[218] where the synthesis is performed in multiple steps, each focusing on a single layer of precursor (Figure 11g). A controlled thickness of precursor can be used, guaranteeing a uniform graphitization at depth for subsequent layers, surveyed by Raman spectroscopy (Figure 11h,i). Along with these outcomes, the control of the electrical conductivity of carbonized and graphitized materials has been essential in developing this field. Although LIG is categorized as semiconducting ($\sigma < 10^3$ S cm$^{-1}$), it has mostly been used due to its conductive characteristics. Contrarily to laser synthesized and patterned metal oxides and other semiconductor materials, where standardization of properties highly depends on the metal type and other variables such as oxygen content, LIG has been mainly compared by its sheet resistance. Another important consideration is the morphology of the resulting LIG, highly dependent on the coefficient of thermal expansion and melting mechanisms of the precursor and irradiation parameters. For PI, the specific manipulation of several parameters, not only related to power but also associated with spot size, beam defocus, and resulting areal energy density, allows for control of shape and topological distribution of LIG networks. More specifically, in the work by Abdulhafez et al.,[108] a control of laser defocus and resulting fluence allows for the formation of distinct 3D arrangements, depending on the distance of the substrate to the beam-shaping lens (Figure 11j). The formation of isotropic pores, cellular networks, and nanofibers can be selected, at transition levels depending on the applied laser fluence regimen (Figure 11k). In addition, synergistic effects of chemical and morphological properties of LIG also influence the interaction of these graphitic materials with aqueous and liquid phases, with the possibility of controlling hydrophobicity, an important factor in several applications requiring electrolyte/electrode interactions.[237,238] For other emerging precursor materials, such process-properties studies have been explored in more specific cases and in less detail but are fundamental in the future development of DLW fabrication paradigms in several applications.

## 4. Materials for Next-Generation Laser-Processed Electronics

ADLW and TDLW mechanisms have shown great versatility and capability to engineer different material sources into conductor and semiconductor products that can participate in the assembly of varied electronic applications. This section is devoted to systematizing several resulting material properties, including conductivity, semiconductor characteristics, and writing resolution of several processing strategies through DLW. Metallic conductors, metal oxides, carbides, and chalcogenides are discussed. Laser synthesis of LIG from several precursor groups is also overviewed, as well as other emerging laser-material engineering approaches, including conductive polymer engineering or composite material synthesis.

### 4.1. DLW Synthesized Metallic Conductors

The role of metallic conductors in electronic systems is vast, encompassing passive and functional roles, such as circuit interconnects,[75,101] microelectrodes for transistor fabrication,[88,102,239] or within information transmission elements.[69,146] DLW techniques have shown to be valid alternatives to this fabrication, where the use of alternative precursor sources and more versatile strategies are capable of changing the conventional paradigm of deposition techniques, that rely on the use of bulk metals for evaporation at back-end-of-line (BEOL) processes.[138] Several mechanisms previously addressed have been used for this purpose, including the sintering of metallic nanostructures, laser-induced reduction of aqueous metal salt precursors, and selective metallization of laser-activated surfaces. Using these techniques, patterning of highly conductive metal structures composed of several metals of interest is possible, where the aim is to increase the efficiency and precision of patterning, while achieving conductivities comparable to the respective bulk metal. An overview of several synthesis and patterning strategies and resulting material properties is presented in **Table 1**, divided by the type of target metal, mechanism, and detailing the precursor formulation used for the DLW process.

#### *4.1.1. Noble Metal DLW*

Metallic silver patterns have been prolifically fabricated using sintering approaches as well as the reduction of silver metal ion precursors, mostly silver nitrate.[159,166,167] These methods promote a good adhesion to the several types of support substrates, since the laser beam is focused on the substrate/precursor interface, leading to interactions between the formed metallic structures and substrate surfaces, including the embedding of NPs.[167,240] For silver, sintering mechanisms appear more efficient in producing highly conductive structures, probably due to the higher weight composition of silver NP precursors when compared to metal ion precursor formulations, which also need additional steps of nucleation and growth to reach fully continuous written geometries. Reported conductivity values by Noh et al.[148] show behaviors close to bulk silver, at $1.4 \times 10^5$ S cm$^{-1}$ (4.5 times lower than bulk silver) for femtosecond laser sintered AgNPs over polyethylene terephthalate (PET) substrates. Laser sintering of silver within DLW has been developed using several different laser systems, but femtosecond lasers have stood out, regarding their capability to efficiently percolate AgNP precursors, while allowing for high-resolution patterning. For higher PW lasers, larger heat transfer profiles are generated, ultimately leading to less capability for sub-micron patterning. To highlight the work by Son et al.,[240] where fine silver patterns can be developed using DLW laser sintering, down to 380 nm in width. For reduction mechanisms,

**Table 1.** DLW approaches targeting metallic conductor patterning.

| Material | Mechanism | Precursor | Substrate | Laser | Conductivity [S cm$^{-1}$] | Width [µm] | Thickness [µm] | Refs. |
|---|---|---|---|---|---|---|---|---|
| Silver | Sintering | 40 nm AgNP suspension | PET | Ti: sapphire femtosecond laser (800 nm) KrF excimer laser (248 nm) | $1.4 \times 10^5$<br>$9.6 \times 10^4$ | – | – | [148] |
| | | 3-6 nm AgNP | Glass and silicon wafer | Ti: sapphire femtosecond laser (780 nm) | $5.5 \times 10^4$ | 0.38 | 0.05 | [240] |
| | | Commercial AgNP ink (36%wt) | Photo paper, PI, and clear PI | Femtosecond laser (515 nm) | $9.6 \times 10^4$<br>$2.1 \times 10^4$<br>$1.9 \times 10^4$ | – | 1 | [141] |
| | | Ag flakes/PDMS ink | PDMS | Nanosecond Yt fiber laser (1064 nm) | $5.9 \times 10^3$ | 250 | 10 | [35] |
| | | Commercial AgNP inks | Printing papers | CW fiber laser (1064 nm) | $1.6 \times 10^5$ | – | 0.85 | [146] |
| | | PU-based Ag ink | TPU | Diode laser (445 nm) | $1.7 \times 10^4$ | 715 | 35.7 | [145] |
| | | PVP coated AgNP | Glass boundary edge | CW fiber laser (1070 nm) | $3.5 \times 10^5$ | 10 | 1 | [101] |
| | Seed growth and sintering | Organometallic silver seed solution | Soda-lime glass and PI | CW diode laser (930 nm) | $6.6 \times 10^4$ | 5 | 0.1 | [105] |
| | Reduction | Silver nitrate + sodium citrate | Glass microchannel | Femtosecond laser (790 nm) | $5.9 \times 10^4$ | 0.125 | 0.008 | [159] |
| | | Silver nitrate + sodium citrate + PVP | PC | CW laser (450 nm) | $2.4 \times 10^3$ | 404 | 23.2 | [167] |
| | | Silver nitrate + sodium citrate + NLSS | Glass | Femtosecond laser (800 nm) | $4.2 \times 10^3$ | 0.18 | – | [166] |
| | | Silver nitrate @ gelatin matrix | Glass | CW laser (405 nm) | 92.6 | 0.9 | – | [163] |
| | | Silver perchlorate @ gelatin | Glass | Ti: sapphire femtosecond laser (780 nm) | 303 | – | – | [162] |
| | | Silver nitrate + trisodium citrate | Silanized cover glass | Ti:Sa femtosecond laser (780 nm) | $5.9 \times 10^4$ | 0.8 | – | [42] |
| | | Silver nitrate + carbon/GO ink | Glass | CW laser (532 nm) | – | – | – | [147] |
| Gold | Sintering | Au nanocluster ink | Glass, Si/SiOx wafer, ITO, PI | CW diode laser (488 nm) | $1.0 \times 10^4$ | 0.25 | 0.02 | [102] |
| | | 1-3 nm diameter SAM capped AuNPs | PI | Argon ion laser (514.5 nm) | $1.8 \times 10^5$ | 10 | – | [239] |
| | Reduction | Tetrachloroauric acid solution | Soda-lime glass | Femtosecond fiber laser | $2.5 \times 10^4$ | 5 | – | [157] |
| | | Tetrachloroauric acid + carbon/GO ink | Glass | CW laser (532 nm) | – | – | – | [147] |
| | | Tetrachloroauric acid @ collagen hydrogel matrix | Silicon | Femtosecond NIR Ti-Sapphire laser (780 nm) | – | 1.2 | – | [241] |
| | | Gold cyanide solution | Glass | CW diode-pumped laser (532 nm) | $6.4 \times 10^4$ | – | – | [242] |

(*Continued*)

**Table 1.** (Continued)

| Material | Mechanism | Precursor | Substrate | Laser | Conductivity [S $cm^{-1}$] | Width [μm] | Thickness [μm] | Refs. |
|---|---|---|---|---|---|---|---|---|
| Platinum | Sintering | Pt particle paste | $Al_2O_3$ substrate | CW fiber laser (1064 nm) | $2.2 \times 10^4$ | 183.5 | <13 | [139] |
| | Reduction | Chloroplatinic acid + carbon/GO ink | Glass | CW laser (532 nm) | $1.7 \times 10^4$ | – | – | [147] |
| | | Ammonium tetrachloroplatinate + iron oxalate | Silanized cover glass | Ti:Sa femtosecond laser (780 nm) | $2.4 \times 10^3$ | 0.8 | – | [42] |
| | | Platinum chloride + NMP | Glass | CW laser (532 nm) | $3.1 \times 10^3$ | 4 | 0.08 | [243] |
| | Selective metalization | Silicon rubber + PMMA and chloroplatinic acid activation for potassium tetranitroplatinate electroless plating | Silicon rubber | Kr-F excimer laser (248 nm) | (0.2 Ω $sq^{-1}$) | 200 | 10 | [210] |
| Copper | Sintering | Inkjet-printed, organic coated 50 nm copper NP ink | Silicon substrate | CW semiconductor laser (808 nm) | (1.3 Ω $sq^{-1}$) | – | – | [244] |
| | | Sub 50 nm CuNPs + diethylene glycol paste | Glass and PEN | CW diode-pumped ND:YAG laser (532 nm) | (<1 Ω $sq^{-1}$) | 20 | 3.2 | [144] |
| | | Sub 50 nm CuNPs + diethylene glycol paste | Epoxy/PET | CW diode-pumped ND:YAG laser (532 nm) | (<1 Ω $sq^{-1}$) | 20 | – | [143] |
| | | Copper formate ink | Glass, ITO-coated glass, and PI | Nanosecond-pulsed UV laser (355 nm) | $1.2 \times 10^4$ | 12 | – | [137] |
| | | Commercial copper ink | Doped GaAs wafer | Diode-pumped picosecond laser (1064 nm) | $9.1 \times 10^4$ | – | 0.4 | [138] |
| | | CuNPs + EG ink | | Nanosecond-pulsed UV laser (355 nm) | $6.5 \times 10^4$ | 5 | 8 | [245] |
| | Reduction | Copper acetate @ deep eutectic solvent | Sodium silicate glass | Picosecond laser (1064 nm) | $5.5 \times 10^4$ | 90 | 4 | [246] |
| | | Copper nitrate @PEG + PVP ink | Polycarbonate (PC) | CW diode laser (808nm) | (1.2 Ω $sq^{-1}$) | 760 | – | [171] |
| | | Copper nitrate @NMP + EG liquid precursor | PI | CW diode laser (808 nm) | $1.0 \times 10^5$ | 300 | – | [82] |
| | | Copper nitrate @NMP + EG liquid precursor | Glass and PI | CW diode laser (808 nm) | $2.7 \times 10^5$ | – | – | [169] |
| | | Copper nitrate + PVP + PMMA | Glass and PC | CW diode laser (808 nm) | (0.57 Ω $sq^{-1}$) | – | – | [170] |
| | | Copper nitrate + EG solution + SiNP | Glass | Femtosecond visible laser (515 nm) | 833.3 | 45 | 10 | [160] |
| | | Copper nitrate + PVP + PEG ink | PC | CW Yb laser (1064 nm) | (0.25 Ω $sq^{-1}$) | – | – | [115] |
| | | Copper nitrate + EG | PDMS and PET | sCW diode laser | $1 \times 10^4$ | 250 | 24 | [103] |

(*Continued*)

**Table 1.** (Continued)

| Material | Mechanism | Precursor | Substrate | Laser | Conductivity [S $cm^{-1}$] | Width [µm] | Thickness [µm] | Refs. |
|---|---|---|---|---|---|---|---|---|
| | Reductive sintering | Cu2O nanowires + EG | Glass and PDMS | CW visible laser | – | <10 | – | [36] |
| | | CuOx NPs + PVP ink | Glass | Pulsed laser beam (1070 nm) | $7.7 \times 10^4$ | – | – | [247] |
| | | CuOx NP + PVP + CTAB ink | PET, PI, and glass | CW Nd: YVO4 laser (532 nm) | $9.5 \times 10^4$ | 6.5 | 0.6 | [87] |
| | | CuOx NP + PVP + CTAB ink | PET | $CO_2$ laser (10.6 µm) | (0.4 Ω $sq^{-1}$) | 120 | 18 | [38] |
| | | CuO NPs + PVP + EG ink | PI | CW diode laser (650 nm) | – | 120 | – | [175] |
| | LISM | PI + silver nitrate catalyst for copper sulfate electroless plating | PI | NIR pulsed fiber laser (1040 nm) | $4.4 \times 10^5$ | 50 | 0.5 | [75] |
| | | Laser-induced backside dry etching activation | Quartz glass + Zr alloy catalyst layer | Femtosecond laser (530 nm) | $5.1 \times 10^5$ | 18 | 2 | [203] |
| Nickel | Reductive sintering | NiOx NP + PVP + CTAB ink | Glass, PET and PI | CW laser (532 nm) | $1.0 \times 10^4$ | 35 | 1.2 | [86] |
| | | NiOx NP + PVP + CTAB ink | Colorless PI | CW laser (532 nm) | $1.0 \times 10^4$ | 22 | 1.6 | [149] |
| | Reduction | Nickel chloride + carbon/GO ink | Glass | CW laser (532 nm) | – | – | – | [147] |
| | LISM | PVD + palladium chloride catalyst for nickel chloride electroless plating | PI | CW semiconductor laser (405 nm) | 0.08 Ω $sq^{-1}$ | 27 | 65 | [204] |
| Copper/silver alloy | Sintering | Cu@Ag core-shell NP ink | PI | Fiber laser (1064 nm) | $3.5 \times 10^4$ | – | – | [142] |
| | Reduction | Copper nitrate + silver nitrate + NMP ink | CW diode laser | CW diode laser (808 nm) | $1.3 \times 10^5$ | 300 | 0.7 | [164] |
| Zinc | Sintering | Zinc microparticles + PVA + ethyl acetate ink | PVA, PlgA, PVP, CA, and Na-CMC | UV laser (355 nm) | $2.0 \times 10^4$ | 125 | 20 | [69] |
| | Reduction | Zinc chloride + carbon/GO ink | Glass | CW laser (532 nm) | – | – | – | [147] |
| Iron | Reduction | Iron chloride + carbon/GO ink | Glass | CW laser (532 nm) | – | – | – | [147] |
| Aluminum | Sintering | 3D printed sub 200 nm AlNPs paste | Al film | Q-switched fiber laser (1064 nm) | 1953.1 | – | – | [152] |

most achieved conductivity values are situated at one order of magnitude lower. Reported conductivity by Xu et al.[159] reached values around $5.9 \times 10^4$ S cm$^{-1}$, employing a 790 nm wavelength femtosecond laser for multiphoton reduction of a silver nitrate precursor and sodium citrate reducing agent, while using a 780 nm Ti:Sa femtosecond laser. Yang et al.[42] reported similar values of conductivity using a similar precursor formulation. In both these works, the writing resolution is to note, showing the capability of femtosecond laser-induced reduction to produce Ag lines with sub-micron width. Depending on the laser power, Xu et al. report line widths as low as 125 nm and a height of 80 nm.[159] For other noble metals, such as gold or platinum, similar strategies have been employed. Laser sintering of gold nanostructures has been an explored technique for gold microstructure writing, due to the lower thermal budgets needed for particle necking and melting, compatible with multiple polymeric substrates.[21,239] Conductivities close to bulk gold have been reported by Seung et al.,[239] at ≈$1.8 \times 10^5$ S cm$^{-1}$ (2.3 times lower than bulk gold). Besides NPs, other reports using alternative gold nanostructures have been presented. These include metalloid gold nanoclusters, although conductivity values reported by Geladari et al. reached one order of magnitude lower ($1.4 \times 10^4$ S cm$^{-1}$).[102] To note the sub-micron resolution of this sintering approach, with minimum linewidth and height of 250 and 20 nm, respectively, without requiring a femtosecond laser system. Sintering of platinum NPs using DLW has been an under-reported approach for the engineering of platinum conductive microstructures, probably due to its higher melting point. However, the use of platinum microparticles has been reported by Wang et al.,[139] for laser sintering/micro-cladding, resulting in thick films with conductivities of $1.7 \times 10^4$ S cm$^{-1}$ (5.5 times lower than bulk platinum). Besides sintering, reduction mechanisms have also been successfully employed for the laser writing of structures comprising these noble metals. For gold, tetracholoauric acid has mostly been used as the gold ion source,[147,157,241] although other precursors, including gold cyanide also being employed, with high conductivity reported by Lim et al.,[242] at $6.4 \times 10^4$ S cm$^{-1}$. For platinum, several metal ion sources have been employed, including chloroplatinic acid,[147] ammonium tetrachloroplatinate,[42] and platinum chloride,[243] with the highest conductivity being for the thermal reduction of platinum chloride and n-methyl-2-pyrrolidone (NMP) aqueous formulation, at $1.7 \times 10^4$ S cm$^{-1}$.[147]

#### 4.1.2. Transition Metal DLW

DLW approaches have also been copiously employed for copper structure writing. Copper precursors, either NPs for sintering or reductive sintering, copper ions, or electroless plating in LISM approaches have been successfully implemented for copper microstructure engineering, taking advantage of the high processability of these copper sources and resulting conductivity. In this regard, the sintering of several copper nanostructure precursors has shown great versatility for conductive track writing, using different size NP and ink formulations, coated in distinct substrates. Good conductivities have been achieved by this method while allowing for good spatial resolution in the hundreds of nanometers range. In the work by Hayati-Roodbari et al.,[138] control on the thickness of sintered copper layers, from 250 to 400 nm, allows for the establishment of both Schottky and ohmic contact behaviors, respectively, over a GaAs semiconductor substrate, while presenting a maximum conductivity of $9.1 \times 10^4$ S cm$^{-1}$. Laser-induced reduction for copper patterning has equally been employed for efficient copper microstructure engineering. Copper nitrate has been the metal salt of choice, and a myriad of formulations using this metal ion source with different reducing agents (e.g. PVP,[168,171] NMP,[82,169] ethylene glycol,[36] and SiNPs)[160] have been employed. Notably, higher conductivities have been achieved by the reduction-based approaches, with the reported conductivity values by Zhou et al. situated at $2.7 \times 10^5$ S cm$^{-1}$.[169] This work showed the significance of controlling experimental parameters to achieve metallic copper phases and the capability of erasing and rewriting copper patterns. This reversible nature of laser engineering of copper precursors is relevant, since by changing laser writing parameters or irradiation atmosphere and resulting reductive or oxidative characteristics, concurrent and reversible synthesis and selective writing of metallic copper and semiconductor copper oxide patterns can occur, for the fabrication of different junction types.[36,115,171] This also shows how copper oxide NP inks are an efficient source material for metallic copper micropatterning. Using a reductive sintering approach, writing of copper with conductivities as high as $9.5 \times 10^4$ S cm$^{-1}$ can be achieved, as reported by Nam et al.,[87] presenting fine features conducive for transparent electronics, with a minimum resolution of 6.5 µm linewidth and 600 nm in height. Copper patterning using LISM approaches has also been a valuable resource, opening new routes for metallic circuit element fabrication. Although in these processes, the laser beam is not responsible for material synthesis or deposition, effective substrate surface activation, and micro structuring allow for an efficient metallization of copper sulfate, notably able to reach conductivity values very similar to that of bulk copper ($5.1 \times 10^5$ S cm$^{-1}$ for femtosecond laser activation of Zr alloy substrate),[203] although lower values are reached depending on the substrate material, sensitizer and laser system. However, relevant features are brought up by LISM approaches, namely the high bonding strength of developed micropatterns due to anchor effects[203] and the capability to develop layered metal structures comprising not only copper but other metals such as silver,[75,196] gold and nickel,[196] through successive electroless plating steps.

Nickel writing has been achieved successfully through reductive sintering approaches, where $NiO_x$ NP inks have been the main precursor source. Using such approaches, the printing of nickel has been performed in a myriad of substrates, including glass, PET, and PI,[44,86,149] with good conductivities around $1.4 \times 10^4$ S cm$^{-1}$ (10 times lower than bulk nickel). Another aspect of using these oxide NP reduction methods is the capability to control the degree of reduction and oxygen content in the resulting written patterns, to also synthesize different bandgap semiconductors, analogous to copper oxide NP precursors.[181,182] Besides transition metals, other target metals have been subjected to DLW fabrication strategies. The patterning of zinc functional structures has been achieved by sintering of zinc microparticles over several substrates, including biodegradable sodium carboxymethyl cellulose (Na-CMC) with good conductivity of $2.0 \times 10^4$ S cm$^{-1}$ (8.45 times lower than bulk zinc).[69]

**Table 2.** DLW approaches targeting metal oxide patterning.

| Material | Method | Precursor | Substrate | Laser | Features | Refs. |
|---|---|---|---|---|---|---|
| $TiO_2$ | LITV | $TiOSO_4{\cdot}xH_2SO_4{\cdot}yH_2O$ (1 M)<br>Solvent: water | Coverslip to hold the aqueous solutions | CW Ti:sapphire laser ($\lambda$ = 760 nm) | Minimum line width ranges from 2.5 to 14.5 µm | [191] |
| $VO_2$ (M) | Laser oxidation | Monoclinic $V_5S_8$ flakes (grown by CVD using $VCl_3$ and sulfur) | $SiO_2$/Si substrate | Confocal Raman microscope ($\lambda$ = 532 nm) | Minimum line width of ~1 µm<br>The maximum thickness of precursor film that can fully convert into $VO_2$ is about 230 nm | [133] |
| $VO_2$<br>$V_2O_5$ | Laser oxidation | Vanadium film (200 nm) | Quartz substrate | CW solid state ($\lambda$ = 410 nm) | – | [185] |
| $VO_2$ | LITV | Vanadyl sulfate (1 M)<br>Solvent: water | Coverslip to contain the aqueous solutions | CW Ti:sapphire laser ($\lambda$ = 760 nm) | Minimum line width ranges from 2.5 to 14.5 µm | [191] |
| $Cr_2O_3$ | | Chromic nitrate (1 M)<br>Solvent: water | | | | |
| $Mn_2O_3$ | | Manganese(II) nitrate (1 M)<br>Solvent: water | | | | |
| $Fe_2O_3$<br>$Fe_3O_4$ | | Iron(III) nitrate (1 M)<br>Iron (II) chloride (1 M)<br>Solvent: water | | | | |
| Pt-doped $Fe_2O_3$ | Laser conversion/oxidation<br>LITV | 28.7 wt % Iron(III) nitrate in 1 g solvent<br>15.7 wt % Ammonium tetrachloroplatinate (II) in 1 g solvent<br>Solvent: deionized water | Glass substrate | CW laser ($\lambda$ = 780 nm) | Thicknesses ranging from 8 to12 µm<br>Line widths between 30 and 40 µm | [186] |
| CoO | Laser oxidation | Cobalt(II) nitrate hexahydrate (40 mg $mL^{-1}$)<br>Copolymer (S-LEC PLT 7552) (60 mg $mL^{-1}$)<br>Solvent: N, N-dimethylformamide, acetonitrile and dichloromethane | Glass slide with PI film<br>Carbon nitride/FTO slides | Laser ($\lambda$ = 405 and 488 nm) | Rod-like, star-like, and rhombic structures were obtained with sizes ranging from 200 nm to 5 µm | [249] |
| $Co_3O_4$ | LITV | Cobalt(II) nitrate (1 M)<br>Solvent: water | Coverslip to contain the precursor solutions | CW Ti:sapphire laser ($\lambda$ = 760 nm) | Minimum line width ranges from 2.5 to 14.5 µm | [191] |
| NiO | | Nickel(II) nitrate (1 M)<br>Solvent: water | | | | |
| NiO | Laser conversion/oxidation<br>Laser-induced thermal voxel | 22.5 wt % Nickel(II) nitrate in 1 g solvent<br>Solvent: deionized water | Glass substrate | CW laser ($\lambda$ = 780 nm) | Thicknesses ranging from 8 to12 µm<br>Line widths between 30 and 40 µm | [186] |
| NiO | Laser oxidation | Nickel(II) nitrate hexahydrate (20 mg $mL^{-1}$)<br>Copolymer (S-LEC PLT 7552) (60 mg $mL^{-1}$)<br>Solvent: N, N-dimethylformamide, acetonitrile and dichloromethane | Glass slide with PI film<br>Carbon nitride/FTO slides | Laser ($\lambda$ = 405 and 488 nm) | Rod-like, star-like, and rhombic structures were obtained with sizes ranging from 200 nm to 5 µm | [249] |
| CuO | LITV | Copper(II) nitrate (1 M)<br>Solvent: water | Coverslip to contain the precursor solutions | CW Ti:sapphire laser ($\lambda$ = 760 nm) | Minimum line width ranges from 2.5 to 14.5 µm | [191] |

(*Continued*)

**Table 2.** (Continued)

| Material | Method | Precursor | Substrate | Laser | Features | Refs. |
|---|---|---|---|---|---|---|
| Cu<br>$Cu_2O$ | Laser reduction | Copper(II) nitrate (2 M)<br>Polyethylene glycol (0.2 g $mL^{-1}$)<br>Polyvinylpyrrolidone (0.1 g $mL^{-1}$)<br>Solvent: deionized water | Polycarbonate sheets | Yttrium fiber laser ($\lambda$ = 1064 nm) | – | [115] |
| CuO | Laser conversion/oxidation | 19.4 wt % Copper(II) nitrate in 1 g solvent<br>Solvent: deionized water | Glass substrate | CW laser ($\lambda$ = 780 nm) | Thicknesses ranging from 8 to12 µm<br>Line widths between 30 and 40 µm | [186] |
| $Cu_2O$<br>CuO | Laser oxidation | Copper layer (15 to 36 nm) | PI substrate | CW laser ($\lambda$ = 514.5 nm) | – | [187] |
| CuO | Laser oxidation | Copper(II) nitrate hydrate (20–60 mg $mL^{-1}$)<br>Copolymer (S-LEC PLT 7552) (60 mg $mL^{-1}$)<br>Solvent: N, N-dimethylformamide, acetonitrile and dichloromethane | Glass slide with PI film<br>Carbon nitride/FTO slides | Laser ($\lambda$ = 405 and 488 nm) | Rod-like, star-like, and rhombic structures were obtained with sizes ranging from 200 nm to 5 µm | [249] |
| ZnO | Photothermal synthesis | Zinc nitrate hexahydrate (0.4 M)<br>Ammonia (14 M)<br>Solvent: water | Glass (ZnO forms on top of the platinum wire) | CW laser ($\lambda$ = 532 nm) | Minimum feature sizes below 1 µm | [42] |
| ZnO | Laser conversion/oxidation | Zinc (II) chloride (0.25 M)<br>Solvent: Ethanol | $SiO_2$/Si substrate | $CO_2$ laser ($\lambda$ = 10.6 µm) | Line width of ~140 µm was obtained | [37] |
| ZnO | LITV | Zinc nitrate (1 M)<br>Solvent: water | Coverslip to contain the precursor solutions | CW Ti:sapphire laser ($\lambda$ = 760 nm) | Minimum line width ranges from 2.5 to 14.5 µm | [191] |
| $ZrO_2$ | | Zirconium(IV) oxynitrate (1 M)<br>Solvent: water | | | | |
| T-$Nb_2O_5$ | Laser sintering | T-$Nb_2O_5$ (15 mg) and tetrachloroauric acid (60 mg)<br>Cellulose acetate (25 mg $mL^{-1}$)<br>Solvent: tetrahydrofurane | PI substrate | UV laser ($\lambda$ = 405 nm) | – | [250] |
| $MoO_2$ (monoclinic phase) | Laser oxidation | Molybdenum chloride (1 M)<br>Solvent: deionized water and ethanol | Poly(styrene-ethylene-butadiene-styrene)<br>PI<br>Glass<br>PDMS<br>Human hair | $CO_2$ laser ($\lambda$ = 10.6 µm) | $MoO_2$ thickness of ~50 µm | [70] |
| $MoO_2$<br>$Mo_4O_{11}$ | LITV | Ammonium molybdate (0.25 M)<br>Solvent: water | Coverslip to contain the precursor solutions | CW Ti:sapphire laser ($\lambda$ = 760 nm) | Minimum line width ranges from 2.5 to 14.5 µm | [191] |
| $RuO_2$ | Laser oxidation/patterning | Cellulose acetate (22.47 mg $mL^{-1}$)<br>Ru(COD)(COT) (125 mg $mL^{-1}$)<br>Solvent: tetrahydrofuran | Ti/Au thin layer covered Kapton foil<br>Silicon substrate | UV laser ($\lambda$ = 405 nm) | The thickness of the laser-assisted synthesized layer was 210 ± 50 nm<br>Distance between adjacent lines of 1 mm | [248] |

(*Continued*)

**Table 2.** (Continued)

| Material | Method | Precursor | Substrate | Laser | Features | Refs. |
|---|---|---|---|---|---|---|
| $RuO_2$ | Laser conversion | $RuO_2 \cdot 1.8H_2O$ powder containing ink (30 mg $mL^{-1}$) Solvent: tetrahydrofuran | PI film | UV laser ($\lambda$ = 405 nm) | Distance between adjacent lines equal to 5 µm | [40] |
| $WO_3$ | LITV | Ammonium tungsten oxide (0.5 M) Solvent: water | Coverslip to contain the precursor solutions | CW Ti:sapphire laser ($\lambda$ = 760 nm) | Minimum line width ranges from 2.5 to 14.5 µm | [191] |
| ITO | Laser conversion/oxidation | Indium (III) chloride hydrate (0.25 M) Tin (IV) chloride pentahydrate (0.25 M) Solvent: Ethanol | $SiO_2$/Si substrate | $CO_2$ laser ($\lambda$ = 10.6 µm) | Line width of ~140 µm was obtained | [37] |

### 4.2. DLW of Metal Oxides

Fabricating flexible electronics requires semiconductor fabrication methods that should differ from commonly used approaches, that rely primarily on multi-step processes that use expensive raw materials.[115] Conversely, most solution approaches used to fabricate metal oxides require a high-temperature sintering step to obtain residue-free materials.[37] The need for an annealing or sintering step limits the material's usability in electronics microfabrication, since processing temperatures for each material should not deteriorate the remaining.[42] DLW appears as an alternative to these limitations since it can be used to produce multiple semiconductors in a scalable, one-step, cost and time-effective process.[115,248] This technique has been used for decomposing metal precursors and their subsequent oxidation,[37] producing semiconductor patterns with high design freedom.[40] The use of DLW for the synthesis of multiple materials opens the door for lithography-free fabrication of oxide electronics.[185] Laser approaches can thus be used as large-scale, time-effective alternatives for synthesizing and patterning metal oxides with good resolution (≈1 µm minimum feature sizes)[42] without needing post-annealing processes.[37] Several metal oxide layers have been synthesized through laser oxidation, reduction, or sintering. Some examples are presented in **Table 2**, jointly with relevant processing parameters, precursor formulations, and relevant DLW outcomes.

It is worth noting the approach developed by Zhao et al.,[70] a method for converting molybdenum chloride precursors to molybdenum dioxide ($MoO_2$) using a $CO_2$ laser (**Figure 12a**). This was performed over several substrates, but porous poly(styrene-ethylene-butadiene-styrene) (SEBS) was selected for the development of bioelectronic components, due to its high breathability (Figure 12b), while serving as a platform for the fabrication of low-thickness patterns of 50 µm (Figure 12c). Due to the intrinsic high conductivity of $MoO_2$, the obtained patterns presented a low sheet resistance of approximately 4.6 Ω $sq^{-1}$.

Another interesting approach is to use the optical properties of an underlying layer to synthesize the intended semiconductor. Particularly, the synthesis of ZnO on top of platinum wires can be achieved due to the local heating caused by the absorption of laser radiation by a platinum layer (Figure 12d), as reported by Yang et al.[42] Upon laser-induced heating, zinc(II) ammine complexes dissociate, causing the precipitation of zinc hydroxide and its subsequent conversion to polycrystalline ZnO, which has direct contact with the platinum layer. By varying the exposure of the liquid zinc precursor to the laser beam energy, controlled deposition and patterning of ZnO microstructures can be performed, both radially and in height (Figure 12e). More specifically, by varying the laser power and exposure time of the employed CW 532 nm wavelength laser, the pattern radius can be varied between 130 nm to 5.2 µm (Figure 12f). Moreover, DLW offers the possibility of tuning the metal oxide structural, chemical (and electrical)[115] properties through the variation of laser parameters such as power and speed,[37,115,185] and it also allows the production of multiple interconnected materials and devices.[37,191] In this scope, Bae et al.[37] produced 5 × 5 two-terminal devices (Figure 12g) consisting of indium tin oxide (ITO) electrodes over ZnO lines acting as channels (Figure 12h) showing great optical transmittance (90.4%). These devices were

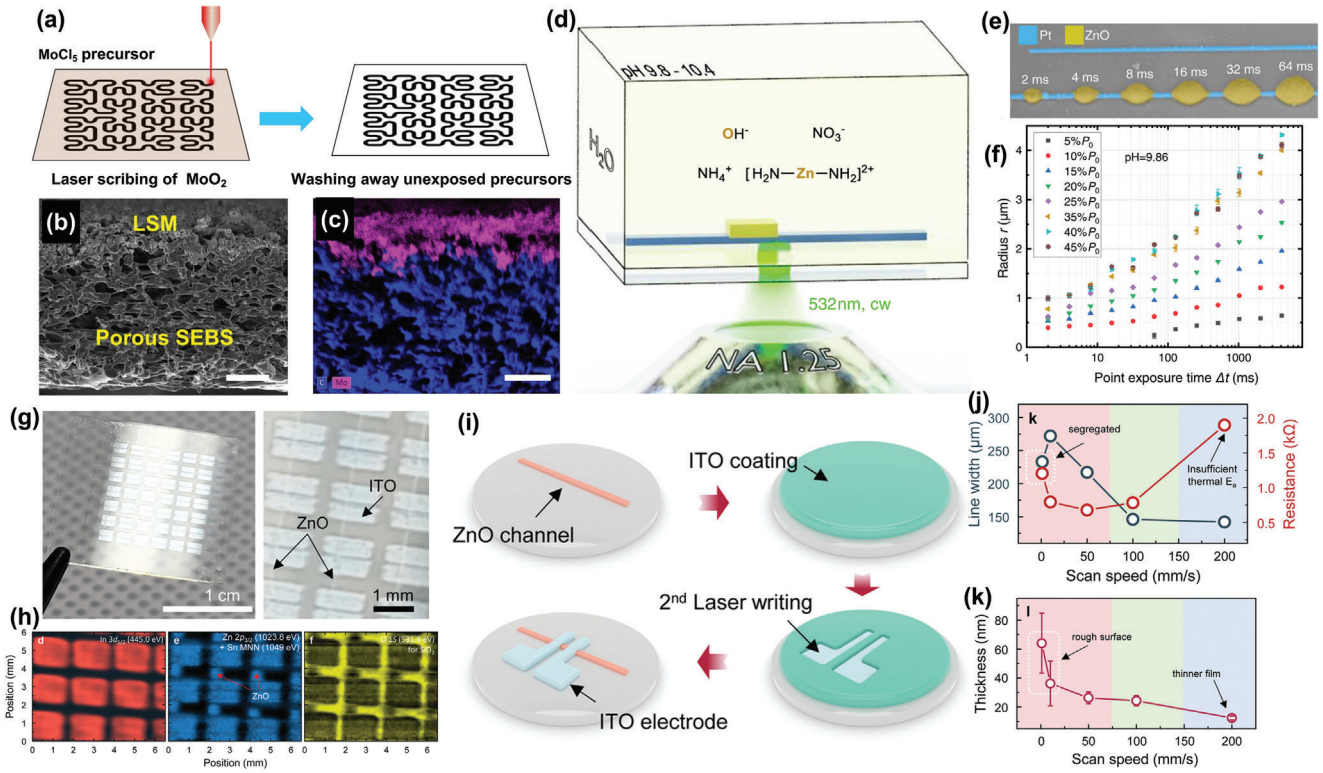


**Figure 12.** DLW metal oxide pattern design strategies. a) Writing of $MoO_2$ patterns using $CO_2$ laser irradiation. Scanning electron microscope (b) and energy dispersive x-ray spectroscopy elemental mapping (c) images of the porous SEBS/$MoO_2$ cross-section. Scale bars, 20 μm (b), 50 μm (c). Reproduced with permission.[70] Copyright 2022, American Association for the Advancement of Science. d) DLW of ZnO patterns promoted by laser absorption of subjacent platinum lines. e) Scanning electron microscope images of ZnO profiles synthesized for different irradiation times and f) evolution of ZnO pattern radius for different laser power levels. Reproduced with permission.[42] Copyright 2023, Springer Nature. g) ZnO/ITO two terminal devices pattern by DLW of solution-processed precursor and h) elemental mapping. i) Schematic of solution processing and DLW steps for ZnO/ITO two-terminal device fabrication. Influence of writing speed on ITO linewidth, resistivity (j), and thickness (k). Reproduced with permission.[37] Copyright 2022, Wiley-VCH.

produced based on laser exposure of zinc chloride precursors, resulting in the formation of the semiconducting channel, then overlapping deposition and writing of conducting ITO electrodes (Figure 12i). In this case, variation of writing speed dictated the control over pattern resolution for ITO, achieving minimum functional linewidth of approximately 140 μm, obtained using a laser power of 6 W and 150 mm $s^{-1}$ scan speed (Figure 12j). For pattern thickness, control of scan speed ensured uniform distribution of written ITO, at around 20 nm (Figure 12k). Besides processing the materials in film form, DLW has been used to alter aqueous solutions, leading to the formation of the intended metal oxide semiconductor.[186,191] The attractiveness of DLW also relies on the possibility of producing heterostructures, binary compounds, and doped materials.[185] In this scope, Jones et al.[115] reported the production of a flexible electronic platform based on copper electrodes interconnected by $Cu_2O$. Tuning the writing parameters of a 1064 nm yttrium fiber laser allowed the production of each material in a single writing step. Sheet resistance values of ≈10 Ω $sq^{-1}$ were obtained. In conclusion, DLW is a largely unexplored area that can convey significant advances in integrated device design.[186] This emerging production approach in the field of flexible electronics does not require high vacuum conditions or standard photolithography processes[42,187] to synthesize multiple conducting and semiconducting materials in the same platform with the desired pattern in a single scanning step without needing mask design and alignment.[40,186,187]

### 4.3. DLW of Transition Metal Chalcogenides

2D transition metal dichalcogenides (TMDCs) have recently become a very popular class of low-dimension materials, due to several advantageous properties, including atomic-scale thickness, direct bandgaps, and interesting electrical conductivity and mechanical properties.[251] Amongst several synthesis techniques, laser-induced thermolysis of TMDCs has been recently explored within DLW paradigms for flexible electronics fabrication using this special class of materials.[18,41,252,253] Such approaches have mainly been employed to synthesize $MoS_2$, employing chemical precursors such as ammonium tetrathiomolybdate[41,252–254] and molybdenum acetylacetonate.[18] Other TMDCs, such as $WS_2$ have also been successfully synthesized,[41,254] as well as alloyed TMDCs for tailored optoelectronic properties.[255] Generally, the processes are mostly based on the thermal decomposition of precursors and resulting chemical reactions, leading to the deposition and writing of the TMDCs. For example, the mechanism for

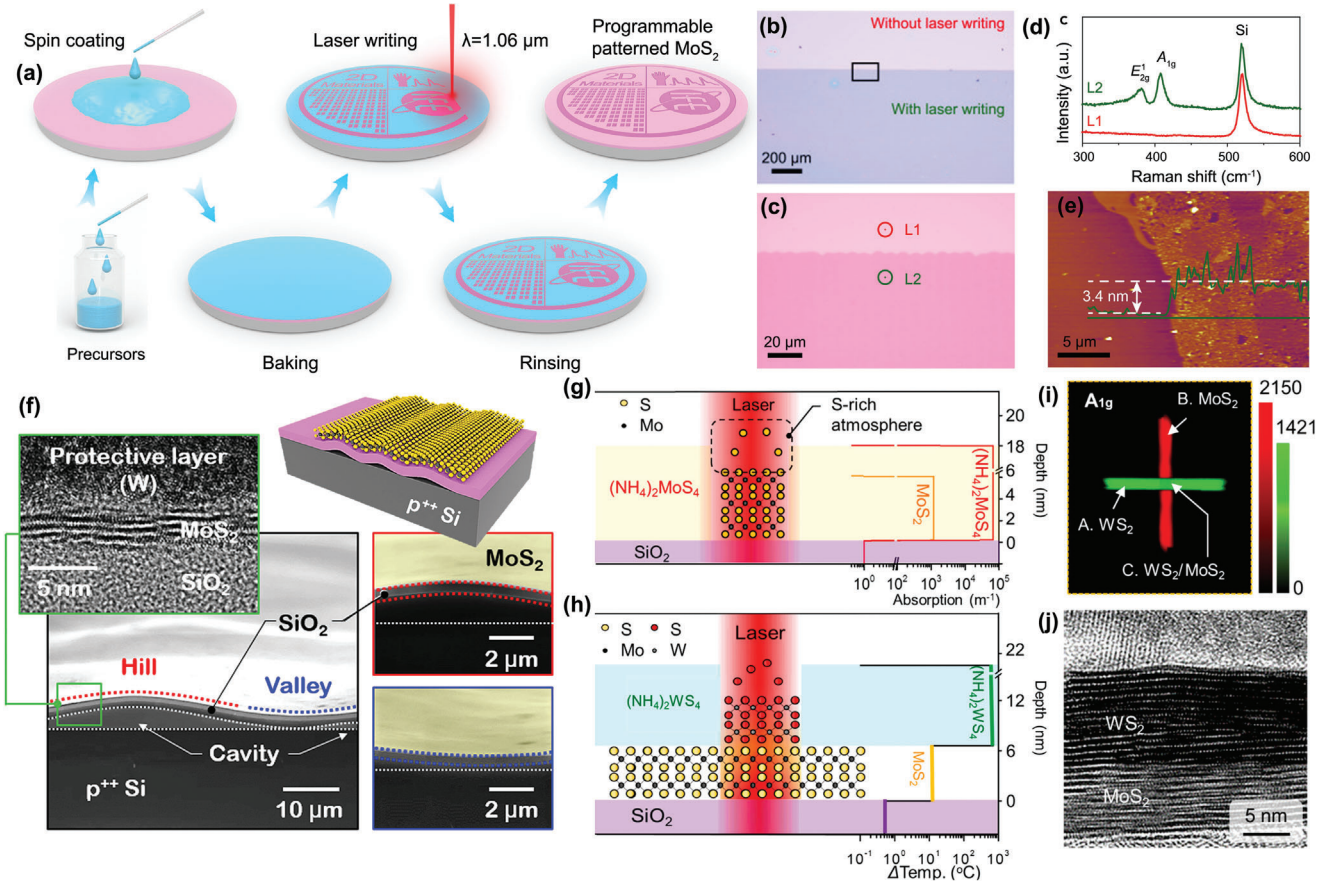


**Figure 13.** DLW for TMDC synthesis and patterning. a) Preparation of ammonium tetrathiomolybdate precursor film for $CO_2$ laser irradiation and $MoS_2$ writing. b,c) Optical image of processing areas before and after irradiation. d) Raman spectra of molybdenum precursor and laser-synthesized $MoS_2$. e) Atomic force microscopy image of laser written $MoS_2$. Reproduced with permission.[252] Copyright 2021, Elsevier B.V. f) Laser-induced, crumpled $MoS_2$ films derived from formation of interfacial cavities. Reproduced with permission.[253] Copyright 2020, Elsevier B.V. g) Laser-induced $MoS_2$ synthesis mechanisms over $SiO_2$. h) Laser-induced $WS_2$ synthesis mechanisms over presynthesized $MoS_2$. i) Imaging of $MoS_2/WS_2$ heterostructure. j) Transmission electron microscopy cross-section of $MoS_2/WS_2$ heterostructure. Reproduced with permission.[41] Copyright 2020, American Chemical Society.

ammonium tetrathiomolybdate conversion into $MoS_2$ has been generally given by the following chemical reactions:[252,253]

$$(NH_4)_2MoS_4 \xrightarrow{T\ laser} 2NH_3 + H_2S + MoS_3 \quad (1)$$

$$MoS_3 \xrightarrow{T\ laser} S + MoS_2 \quad (2)$$

Several reports have resorted to this approach for the patterning of $MoS_2$. One such method was proposed by Xu et al., for the patterning of this TMDC over $Si/SiO_2$ substrates using a fiber laser ($\lambda = 1.06$ μm).[252] The precursor films are spin-coated onto the plasma-cleaned rigid support wafer, followed by precursor baking, DLW process, and rinsing of unconverted precursor (**Figure 13a**), with the authors also describing the capability of transferring the written material onto flexible substrates. A clear distinction is visible between processed and unprocessed precursor areas (Figure 13b,c), as well as in their chemical characteristics, with Raman spectra confirming the successful synthesis of the 2D 2H crystal phase of the MoS2 film (Figure 13d). A very thin pattern of $MoS_2$ could be designed with this approach, down to 3.4 nm in thickness and an average roughness of 0.78 nm (Figure 13e). A similar method proposed by Park et al.[253] shows the capability to control the surface morphology of the TMDC layer, using internal stresses and the formation of a crumpled layer, ascribed to the separation of $SiO_2$ thin film over the Si wafer caused by laser irradiation (Figure 13f). This in turn causes the formation of interfacial cavities in the TMDC layer, resulting in crumpled $MoS_2$ structures exhibiting improved performance when included in TENGs, compared with devices containing a flat $MoS_2$ layer. The enhanced performance was attributed to increased surface roughness and changes in the work function of the TMDC. The electrical conductance of flat and wrinkled $MoS_2$ surfaces was evaluated to be $6.27 \times 10^{-3}$ S·cm$^{-1}$ and $2.07 \times 10^{-2}$ S·cm$^{-1}$, respectively. The work functions were also studied, and values of 4.32 eV and 4.54 eV were computed for flat and highly wrinkled surfaces. In another work by the same group, the laser thermal energy was also used to produce $WS_2$, to create $WS_2/MoS_2$ heterostructures.[41] During laser thermolysis, the authors describe the chemical processes leading to

synthesis, where oxygen is pushed out of the reaction area, creating a sulfur-enriched atmosphere that promotes the formation of $MoS_2$ (Figure 13g). $WS_2$ structures, and consequently $WS_2/MoS_2$ heterostructures, were produced similarly to $MoS_2$, but the precursor was ammonium tetrathiotungstate, which was deposited on top of the pre-synthesized $MoS_2$ (Figure 13h). Due to its low absorption coefficient, $MoS_2$ films present high resistance to harsh laser-based thermal annealing. Thus, executing laser-induced thermolysis to produce $WS_2$ on top of $MoS_2$ does not damage the TMDC layer. The presented method allows for the selection of the processing layer, taking advantage of the absorption coefficient of each material, demonstrating the development of multilayer devices based on TMDCs,[41] with linewidths as low as 24.5 µm and very low thicknesses, characteristic of the 2D arrangement of these TMDCs (Figure 13i,j).

Femtosecond laser synthesis of $MoS_2$ was also reported by Xu et al., ($\lambda = 780$ nm).[18] According to the authors, the use of this high photon flux laser allows for the creation of controlled photochemical microreaction zones at the focal point, in opposition to the conventional approaches based on thermolysis mechanisms. This, in turn, leads to the photochemical decomposition of precursor and subsequent synthesis reactions triggered by TPA processes. To achieve this, a careful precursor formulation was designed by the authors. Briefly, carbon sulfide was chosen due to its ability to improve the crystallinity of the synthesized materials, whereas propanol was used as a solvent to prevent the oxidation of newly formed products. Oleylamine was mixed with this organic solvent, to enhance film formation and increase the precursor's stability, since it can tune its melting point. The synthesis of $MoS_2$ occurs in three steps. Briefly, the complex resulting from a prior reaction between oleylamine and carbon disulfide reacts with the molybdenum precursor, forming a metal complex. Laser exposure, in turn, converts this molybdenum metal complex into a $MoS_2$ pattern that can present a width of approximately 3.8 µm and a thickness of 40 nm. A lower line width can be reached if the proportion of oleylamine is reduced. Besides the high resolution, reasonable electrical properties can be reached as the produced $MoS_2$ layers presented a conductivity of 3.17 S $cm^{-1}$.

Laser exposure has also been used for the simultaneous crystallization and patterning of $MoS_2$ and $WSe_2$ on PDMS substrates. The crystallization of these 2D materials was achieved through the irradiation of thin stoichiometric amorphous films deposited on the flexible substrate (via PLD) with a nanosecond laser ($\lambda = 1064$ nm). The laser wavelength was chosen due to the low optical absorption of PDMS. Thus, by controlling the pulse duration and the number of laser pulses, the energy delivered to the sample was controlled to stimulate the crystallization of the amorphous film without substrate damage. Phase transition was stimulated by localized photothermal heating resulting from laser exposure under an argon flow, which was used to avoid surface oxidation.[29] Additionally, laser-induced crystallization and oxidation of a monolithic amorphous $MoS_2$ film have been proven to produce different molybdenum-containing materials, including conductors ($MoO_2$), semiconductors (2H-$MoS_2$), insulators ($MoO_3$), and $Mo_4O_{11}$ depending on the laser intensity and exposure time. The irradiation at ambient pressure of amorphous $MoS_2$ films, deposited on glass substrates via magnetron sputtering, was performed using a continuous-wave laser ($\lambda =$ 514 nm). This approach can be used to create several electronic circuits since different laser parameters can produce different materials from the same TMDC precursor film with good resolution (on the order of 50 µm).[256]

### 4.4. DLW of Carbide Materials

Transition metal carbides have attracted much attention since they present high electrochemical activity, low resistivity, thermal stability, and corrosion resistance.[81,216] However, the production of ultrathin transition metal carbides requires high temperatures to generate the MAX phase and hazardous chemicals to perform the etching step. Among the alternatives considered to produce these materials is laser-assisted synthesis.[81] A method for the laser-induced synthesis of molybdenum carbide on a paper substrate has been thoroughly described. The metal carbide is produced during laser scanning of a paper substrate previously sprayed with $Mo^{5+}(MoCl_5)$/gelatin ink, resorting to a $CO_2$ laser (**Figure 14a**).[257] The irradiation of the soaked substrate leads to the formation of graphene with embedded $Mo_3C_2$ structures, confirmed by X-ray diffraction analysis (Figure 14b). The carbide formation process was suggested to be directly related to the Mo/gelatin matrix's ability to absorb laser energy then used to form molybdenum carbide. Gelatin is a fundamental agent since it can form a triple helix structure resulting in a lamellar morphology with embedded molybdenum cations which stimulates bond formation among carbide and carbon, leading to improved conductivity. Moreover, gelatin has functional groups that can bind with $Mo^{5+}$, increasing the absorption of laser energy and, consequently, local temperature.[257,258] The same group further developed this method to produce other transition metal carbides in the form of ultrathin flakes. Hydrogels with embedded transition metal ions ($Mo^{5+}$, $W^{6+}$, and $Co^{2+}$) deposited onto glass substrates are irradiated with a $CO_2$ laser (Figure 14c), absorbing energy and leading to the synthesis of porous metal carbide species (Figure 14d). The species present in the precursor hydrogel formulation (ions, polymer, and metal-ligand) define the obtained material since they determine the efficiency of energy absorption, which, jointly with the activation energy of carbonization, determine the formation of metal carbides or oxides.[81]

In a related approach, laser techniques were used for synthesizing nitrogen-doped carbon networks with embedded $MoC_{1-x}$ NPs. These NPs are formed during laser-induced carbonization through a carbothermal reduction reaction where the transient molybdenum clusters are reduced to molybdenum carbides. Films containing ammonium heptamolybdate were deposited on silicon wafers and then scanned with a $CO_2$ laser ($\lambda = 10.6$ µm) to produce the $MoC_{1-x}$ NPs embedded in the carbon matrixes. Interestingly, sodium iodide acted as an effective porogen agent leading to networks with increased specific surface area after laser exposure, which contributed to the higher sensing response of the sensors developed using these materials to detect volatile organic compounds.[216] Using these approaches, several reports take advantage of these carbothermal synthesis processes to integrate polymer materials of interest with laser-synthesized carbide materials.[130] One example is the use of aluminum NPs over PET substrates, which can be transformed into aluminum carbide integrated into laser-written patterns (Figure 14e).[259] Using a 450 nm diode laser, laser-induced polymer melting around deposited

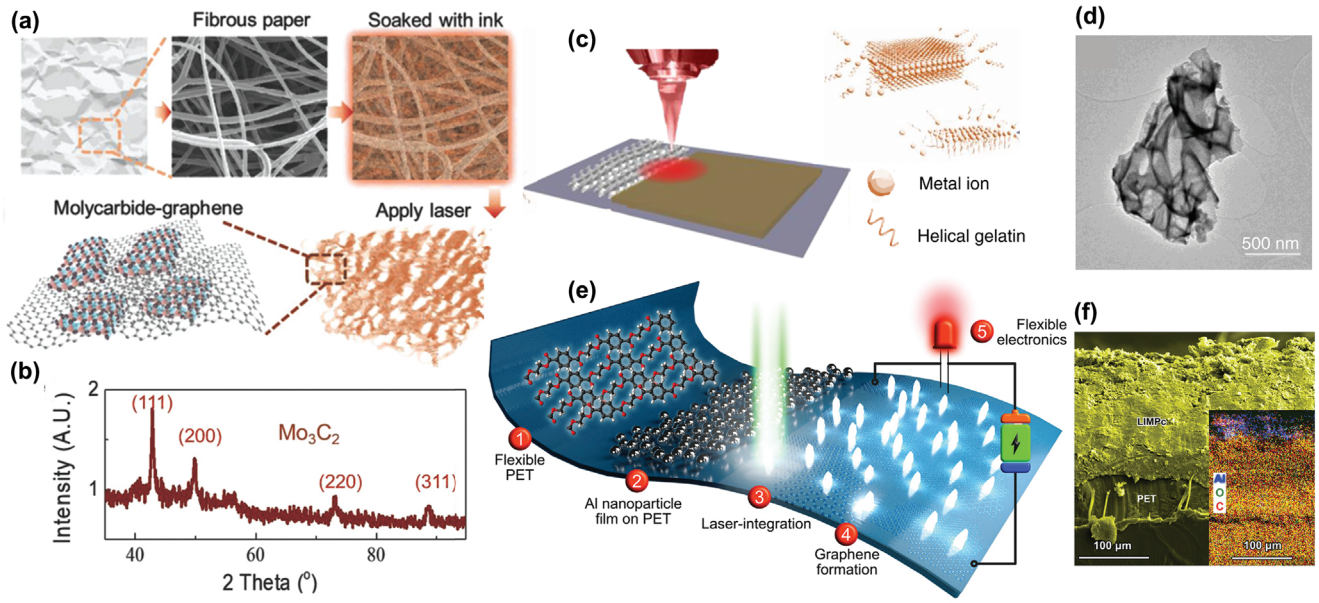


**Figure 14.** DLW synthesis and patterning of carbide materials. a) $Mo_3C_2$ synthesis over paper substrates, using a gelatin-mediated ink containing $Mo^{5+}$ ions, resulting in molycarbide-graphene composites. b) XRD spectrum of $Mo_3C_2$. Reproduced with permission[257] Copyright 2018, Wiley-VCH. c) Synthesis of ultrathin transition metal carbides from metallo-hydrogel precursor. d) TEM image of laser synthesized $MoC_x$, composed of randomly oriented carbide crystals. Reproduced with permission.[81] Copyright 2019, Springer Nature. e) DLW synthesis and incorporation of $Al_4C_3$ over PET substrates for flexible electronics. f) Cross-section SEM image (inset EDX elemental mapping) of written patterns with incorporated aluminum carbide particles. Reproduced with permission.[259] Copyright 2021, Wiley-VCH.

Al NPs leads both to the formation of $Al_4C_3$ carbide structures and graphene structures, resulting in a composite material where there is a superficial abundance of $Al_4C_3$ (Figure 14f), that provides very good mechanical resilience to the written conductive patterns and resulting applications. Similar approaches take advantage of the composition of certain polymeric materials, that have the presence of metals of interest. This is the case in the abundant presence of silicon in several elastomeric substrates, such as PDMS or Ecoflex, that have been directly irradiated for the patterning of SiC structures.[227,260,261]

### 4.5. DLW of Carbon-Based Materials

The manipulation of carbon-based precursors and surfaces using DLW has been explored over the years, to achieve the synthesis of varied materials or improve their functionality in different contexts. Processes that include annealing of amorphous carbon films,[262] synthesis of CNTs from carbon black,[66] carbon-rich SiC structures over 4H-SiC wafer,[263] and writing of diamond-like carbon materials[264] are some of the relevant examples. However, their expression and adoption in electronics microfabrication was not widespread, since either the materials did not provide attractive properties or because they were meant to substitute established techniques and did not provide sufficient flexibility and throughput. Recently, other relevant approaches with much higher adoption have appeared, where laser synthesis and patterning of reduced graphene oxide (rGO) stand out.[183] Even though the popularity and prolific applicability of laser-based rGO synthesis, this method suffers from a key disadvantage, since there is the need for multiple preparation steps, starting with the cumbersome synthesis of GO from graphite, GO dispersion, and ink preparation, followed by the modification of the substrate material or surface with GO. However, this technique propelled the interest in laser fabrication and engineering of graphene-based electronics.[265]

Contrarily, DLW applied for direct carbonization and graphitization of substrates has gained great traction, since it has shown to be compatible with a large pool of substrate sources, from synthetic to naturally sourced. Simultaneously, it allows for one-step, selective synthesis, and patterning of tailored graphene-based structures and seamless assembly of graphene architectures. To draw comparisons between several precursor substrates and resulting irradiation outcomes, an overview of LIG synthesis and properties using several emerging precursor substrates is presented in **Table 3**, including aromatic polymers, naturally derived precursors, and custom-made precursor formulations.

#### *4.5.1. Aromatic Polymers*

Since the initial report by Jian Lin et al.,[72] several advancements have been made in the preparation of LIG from different aromatic polymer sources. For PI and similar polymers containing aromatic and imide repeating units, efficient graphitization is straightforward, where fine control of irradiation parameters leads to sheet resistances of ≈15 Ω $sq^{-1}$ ($\sigma$ of 25 S $cm^{-1}$) or lower. Other aspects besides conductivity have also been manipulated with great efficiency, including morphological characteristics,[108] surface hydrophobicity,[238] and doping of graphene crystalline structures.[297] Many process-property optimization studies

**Table 3.** Overview of LIG synthesis from carbon-based precursors and resulting properties.

| Precursor | Substrate formulation/ treatment | Atmosphere | Laser source | ID/IG | Conductivity | Refs. |
|---|---|---|---|---|---|---|
| PI | – | Ambient | $CO_2$ laser (10.6 µm) | 0.4 | 15 Ω $sq^{-1}$ / 25 S $cm^{-1}$ | [72] |
| Polyetherimide | 3D printed PEI | Ambient | $CO_2$ laser (10.6 µm) | – | 0.3 Ω $sq^{-1}$ | [266] |
| | – | Ambient | $CO_2$ laser (10.6 µm) | 0.2 | 15 Ω $sq^{-1}$ | [104] |
| Polycarbonate/PEI blends | Different blend percentages | Ambient | $CO_2$ laser (10.6 µm) | – | 4 S $cm^{-1}$ | [267] |
| Polyethersulfone | Microporous PES | Ambient | $CO_2$ laser (10.6 µm) | 0.7 – 0.3 | 4.1 Ω $sq^{-1}$ / 9.24 S $cm^{-1}$ | [218] |
| Parylene-c | – | Ambient<br>Nitrogen flow | $CO_2$ laser (10.6 µm) | 0.42 | 9.2 Ω $sq^{-1}$<br>178.5 Ω $sq^{-1}$ | [268] |
| Polybenzimidazole ink | PBI @ DMSO coated on PET and glass | Ambient | Picosecond UV laser (355 nm) | – | 8 Ω $sq^{-1}$ / 50 S $cm^{-1}$ | [222] |
| Liquid crystal polymer | Aromatic block copolymer | Ambient | 450 nm laser | 0.58 | <20 Ω $sq^{-1}$ | [71] |
| Para-aramid textile (Kevlar) | Woven, non-woven and knitted textiles | Ambient | Yb-doped femtosecond fiber laser (1035 and 347.8 nm) | 0.265 | 2.86 Ω $sq^{-1}$<br>5.02 Ω $sq^{-1}$ | [269] |
| Meta-aramid (Nomex paper) | – | Ambient | $CO_2$ laser (10.6 µm) | – | ~20 Ω $sq^{-1}$ | [270] |
| Carbon fibers | Mesophase pitch carbon fibers (pre-carbonized) | – | CW semiconductor laser (915 nm) | | 7.04 × $10^3$ S $cm^{-1}$ | [126] |
| | Lignin-impregnated carbon cloth | Ambient | $CO_2$ laser (10.6 µm) | 0.85 | – | [271] |
| Liquid precursor | Synthetic aromatic-rich polymeric viscous precursor using benzoxazine chemistry | Ambient | $CO_2$ laser (10.6 µm) | 0.4 | 50 S $cm^{-1}$ | [79] |
| | Furfuryl alcohol | Ambient | $CO_2$ laser (10.6 µm) | 0.7 | – | [129] |
| Wood | – | Ar/H2 | $CO_2$ laser (10.6 µm) | 0.48 | 10 Ω $sq^{-1}$ | [125] |
| | – | Ambient | UV femtosecond laser (343 nm) | 0.63 | 10 Ω $sq^{-1}$ | [223] |
| | Iron-tannic acid ink treatment | Ambient | $CO_2$ laser (10.6 µm) | – | 30 Ω $sq^{-1}$ /25 S $cm^{-1}$ | [217] |
| Cork | – | Ambient | $CO_2$ laser (10.6 µm) | <1 | 115 Ω $sq^{-1}$ | [272] |
| | Agglomerated and natural cork | – | Diode-pumped Nd:YVO4 pulsed laser (355 nm) | <1 | 75 Ω $sq^{-1}$ | [224] |
| | Commercial cork + FR (boric acid) | Ambient | 450 nm laser | 1 | 46 Ω $sq^{-1}$ | [226] |
| | Agglomerated cork + wax treatment | Nitrogen flow | Nd:YAG fiber laser (1.06 µm) | 0.2 | 7.5 Ω $sq^{-1}$ | [273] |
| | Natural cork | Ambient | 450 nm laser | 0.8 | 10.8 Ω $sq^{-1}$ | [274] |
| Lignin / Lignocellulose | Lignin/PVA film | Ambient | $CO_2$ laser (10.6 µm) | 0.39 | 3.8 Ω $sq^{-1}$ /66.2 S $cm^{-1}$ | [275] |
| | Lignin/PVA/urea film | Ambient | $CO_2$ laser (10.6 µm) | 0.33 | 2.8 Ω $sq^{-1}$ | [276] |
| | Lignin/PEO film | Ambient | $CO_2$ laser (10.6 µm) | 1.1 | 363.1 Ω $sq^{-1}$ | [277] |
| | Kraft lignin/PVA | Ambient | $CO_2$ laser (10.6 µm) | 0.37 | 4.5 Ω $sq^{-1}$ | [278] |
| | DES pretreatment for lignocellulose film production | Ambient | $CO_2$ laser (10.6 µm) | 0.61 | 24 Ω $sq^{-1}$ | [78] |
| | 2-hydroxyethyl cellulose + lignosulfonate ink + FR (boric acid) | Ambient | $CO_2$ laser (10.6 µm) | – | 3.8 Ω $sq^{-1}$ / 28 S $cm^{-1}$ | [279] |

(*Continued*)

**Table 3.** (Continued)

| Precursor | Substrate formulation/ treatment | Atmosphere | Laser source | ID/IG | Conductivity | Refs. |
|---|---|---|---|---|---|---|
| Paper | Whatman filter paper + commercial FR (ammonium sulfamate) | Ambient | $CO_2$ laser (10.6 µm) | 0.86 | 61.5 Ω $sq^{-1}$ | [280] |
| | Filter paper + commercial FR (ammonium phosphate) | Ambient | CW $CO_2$ laser (10.6 µm) | 0.5 | 32 Ω $sq^{-1}$ | [281] |
| | Filter paper + commercial FR (ammonium phosphate) | Ambient | Diode-pumped Nd:YVO4 UV laser (355 nm) | – | 132 Ω $sq^{-1}$ | [225] |
| | Cotton cellulose paper + FR (ammonium sulfamate) | Ambient | $CO_2$ laser (10.6 µm) | 1 | 23 Ω $sq^{-1}$ | [43] |
| | Colored paper, paper cup & milk carton | – | Nd:YAG CW laser (532 nm) | 0.9 | 105 Ω $sq^{-1}$ | [282] |
| | Whatman filter paper + FR (sodium tetraborate) + coloured wax loading | Ambient with nitrogen flow | $CO_2$ laser (10.6 µm) | 0.28 | 5 Ω $sq^{-1}$ / 24.3 S $cm^{-1}$ | [220] |
| | Hemp fiber paper + lignin-based epoxy acrilates + FR (ammonium phosphate) | Ambient | $CO_2$ laser (10.6 µm) | 0.77 | 3 Ω $sq^{-1}$ | [283] |
| | Filter paper + lignin solution + FR | – | 460 nm laser | – | 52 Ω $sq^{-1}$ | [284] |
| Nanocellulose | TEMPO-oxidized cellulose nanofibers | Ambient | $CO_2$ laser (10.6 µm) | >1 | 60 mS $cm^{-1}$ | [132] |
| | Cellulose nanofiber film | Ambient | Femtosecond laser (522 nm) | 0.2 | 6.9 S $cm^{-1}$ | [84] |
| | Cellulose nanocrystals film | Nitrogen flow | $CO_2$ laser (10.6 µm) | >1 | 600 Ω $sq^{-1}$ | [285] |
| Hemicellulose | Carboxymethyl Xylan + FR (ammonium phosphate) | Ambient | CW $CO_2$ laser (10.6 µm) | – | 186 Ω $sq^{-1}$ | [286] |
| Chitosan | Chitosan/HCl solution | Ambient | $CO_2$ laser (10.6 µm) | – | 5.5 kΩ $sq^{-1}$ | [287] |
| | Chitosan/acetic acid/glycerol solution | Ambient | 3-step laser synthesis: $CO_2$ laser (10.6 µm) and UV laser (405 nm) | 1 | 40 Ω $sq^{-1}$ / 2.5 S $cm^{-1}$ | [288] |
| | Carboxymethyl chitosan aqueous solution | Ambient | CW $CO_2$ laser (10.6 µm) | – | 2.2 kΩ $sq^{-1}$ | [221] |
| | Chitosan oligosaccharide aqueous solution | Ambient | CW $CO_2$ laser (10.6 µm) | – | 33.9 Ω $sq^{-1}$ | [221] |
| | Chitosan hydrochloride aqueous solution | Ambient | CW $CO_2$ laser (10.6 µm) | – | 12.7 Ω $sq^{-1}$ | [221] |
| | Chitosan-borax composite film | Ambient | $CO_2$ laser (10.6 µm) | | 110 Ω $sq^{-1}$ | [289] |
| Chitin | Chitin nanopaper + FR ($CaCl_2$) | – | $CO_2$ laser (10.6 µm) | – | – | [80] |
| Alginate | Cross-linked sodium alginate ($CaCl_2$ cross-linking agent) | – | $CO_2$ laser (10.6 µm) | 2.2 | 15 kΩ $sq^{-1}$ | [290] |
| Agarose | Agarose + lignin hydrogel | Ambient | Femtosecond laser (522 nm) | – | 150 µS | [291] |
| Elastomers | Ecoflex | Ambient | CW Verdi laser (532 nm) | – | – | [227] |
| | PDMS | Ambient | CW diode laser (405 nm) | 0.8 | 5.0 kΩ $sq^{-1}$ | [292] |
| | PDMS | Ambient | Femtosecond laser (522 nm) | 0.4 | 0.5 S $cm^{-1}$ | [293] |
| | PDMS + triethylene glycol | Ambient | $CO_2$ laser (10.6 µm) | 1.64 | 130 Ω $sq^{-1}$ | [294] |
| Natural fabrics | Commercial woven silk fabric precarbonized before irradiation | Ambient | Fiber laser (1064 nm) | – | 40 Ω $sq^{-1}$ | [295] |
| Metal-organic frameworks | NiCo-MOFs/PAA films | – | Femtosecond laser (1035 nm) | 0.98 | 45 Ω $sq^{-1}$ | [296] |

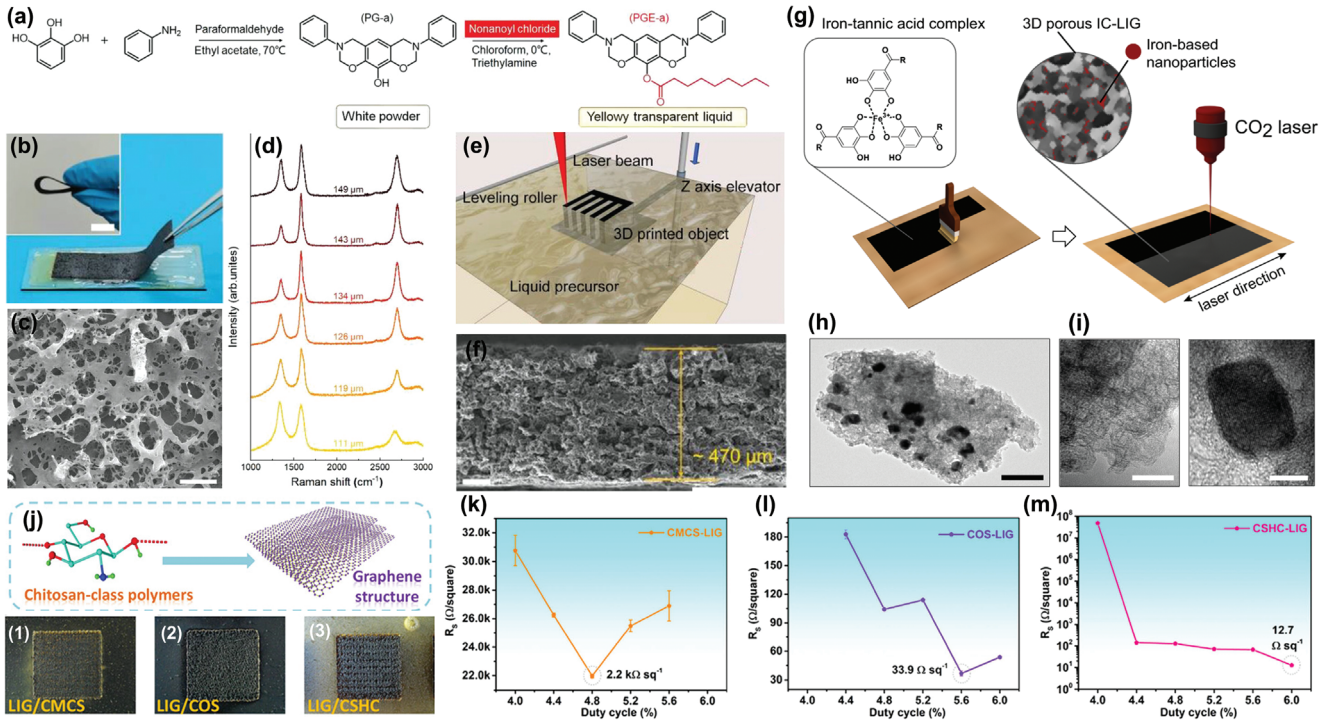


**Figure 15.** DLW processing of aromatic, lignocellulosic, and polysaccharide-based substrates for LIG synthesis and patterning. a) Chemical structure of aromatic liquid precursor made from aromatic monomers and long alkyl chains (PGE-a). b) Images of converted liquid precursor, showing mechanical stability and flexibility. c) SEM image of porous LIG structure arising from graphitization of liquid precursor. d) Raman spectroscopy process-property optimization of chemical properties of LIG, depending on laser spot size. e) Printing of 3D LIG microstructures from aromatic liquid precursor and f) resulting thickness of the LIG macrostructure. Reproduced with permission.[79] Copyright 2022, Wiley-VCH. g) Modification of wood with iron-tannic acid ink for improved DLW processability and LIG conversion. h,i) TEM image of LIG and iron carbide NPs, responsible for improving graphitization potential. Reproduced with permission.[217] Copyright 2022, Springer Nature. j) DLW conversion of chitosan-class polymers: i) carboxymethyl chitosan (CMCS), ii) chitosan oligosaccharide, and iii) chitosan hydrochloride. k–m) Process-property optimization of sheet resistance employing duty cycle has the fabrication parameter of study. Reproduced with permission.[221] Copyright 2023, American Chemical Society.

targeting different characteristics of LIG materials have shown to be crucial to understanding irradiation outcomes in PI and establishing protocols for the transfer of writing principles for the graphitization of alternative polymer substrates. Several aromatic polymers have been targeted, including PEI,[104,266] polyethersulfone (PES),[218] parylene-C,[268] polybenzimidazole (PBI),[222] and aromatic polyamides.[269,270] In terms of the conductive characteristics of resulting LIG, similar sheet resistances are achieved to standard PI-derived LIG. Notably, PEI has shown to be a high-efficiency precursor, with sheet resistances below that of PI, with values as low as 0.3 Ω $sq^{-1}$ for LIG derived from 3D printed PEI surfaces.[104] This work by Gilavan et al.[104] shows the capability of integrating conductive LIG patterns on surfaces with 3D conformations besides commercial polymer surfaces. Thus, one of the main trends in aromatic polymer-based LIG has been the use of custom-made polymer formulations, in opposition to commercial forms of these materials. One example is the work by Correia et al.,[268] where LIG patterning is performed on parylene-C, a biocompatible, flexible, highly inert substrate, deposited over a glass carrier through CVD. By employing ambient and nitrogen-rich irradiation atmospheres, the authors showed the relevant influence of ambient atmospheres to achieve an efficiency graphitization of this aromatic polymer precursor, reaching sheet resistances values as low as 9.2 Ω $sq^{-1}$ for ambient atmosphere, in opposition to 178.5 Ω $sq^{-1}$ when employing a nitrogen-rich atmosphere.

Because of the efficient nature of this DLW method, novel fabrication paradigms have appeared for these high-efficiency aromatic precursors. One such breakthrough is the development of LIG from aromatic liquid precursors. In the work by Huang et al.,[222] organic PBI inks were used as a graphene-forming phase and can be printed onto different substrates, including glass and PET. Attractive conductivities can be achieved using this process, employing a picosecond UV laser, with a sheet resistance of 8 Ω $sq^{-1}$ translating to conductivities of ≈50 S $cm^{-1}$. In the work by Yu et al.,[79] the authors developed a custom-made formulation of a liquid, viscous aromatic polymer precursor, made from two monomer units, that endow the precursor with its graphitizable characteristics, arising from the aromatic structure, as well as molecular flexibility, through the introduction of a long alkyl chain (**Figure 15a**). No detriment to the structural integrity of the graphitized patterns was caused by the liquid nature of the precursor (Figure 15b), retaining the characteristic porous nature of LIG (Figure 15c). The authors performed process-property optimization studies focusing on the three fabrication variables, namely the spot diameter, laser power, and thickness of the precursor film. Spot size was an important variable determining the efficiency of graphitization, surveyed by Raman spectroscopy

(Figure 15d), and in conjunction with the remaining two variables, tunable conductivity and thickness of graphitization layers were achieved, showing a maximum conductivity of ≈50 S $cm^{-1}$. Most importantly, this liquid characteristic of the precursor allows for the printing of 3D LIG structures, by employing successive irradiation cycles and manipulating beam focus, by moving the precursor in the *z*-axis (Figure 15e). This is performed by moving the substrate platform at a length equal to the thickness of individual LIG layers, leading to the integration of porous, vertical layers within 3D geometries with controlled height (Figure 15f). This turns spot size into a key fabrication parameter since different positionings of the laser beam lead to varied spot sizes and possible inconsistencies of the synthesis in the vertical direction. Additive laser printing of 3D LIG structures has thus been sought after to improve the applicability of laser graphitization processes. Another proposed approach was reported by Song et al.,[218] using successive porous PES layer deposition and laser graphitization. This layer-by-layer covalent growth approach allows for an efficient interconnection between subsequent LIG layers, showing not only an efficient conductivity in each layer, but also an improved cross-layer conductivity for the all-graphene macrostructures. In-plane conductivity of 9.2 S $cm^{-1}$ was achieved, while comparable cross-layer conductivity of 8.2 S $cm^{-1}$ was reported. This good isotropic conductivity was attributed to the capacity to achieve efficient covalent interconnection between LIG layers, also improving crystallinity over the macrostructure thickness. Other aromatic polymer forms were shown to be attractive LIG precursors. Notably, aramid materials have been used, either in the form of Kevlar fabrics[39,269,298] or Nomex paper.[270] In the work by Yang et al.[269] the use of a femtosecond fiber laser for the graphitization of non-woven, knit, and woven Kevlar textiles allows for the efficient synthesis of LIG with low sheet resistances of 2.86 Ω $sq^{-1}$, endowing several functionalities onto these textiles for multimodal applications in smart clothing. Nomex paper sheets have also resulted in LIG with attractive sheet resistances of ≈20 Ω $sq^{-1}$, enabling the production of double-sided surfaces employed for human-machine interfacing.[270]

#### 4.5.2. Lignocellulosic Materials

Several sources of vegetable biomass have been used as efficient LIG precursors, due to the presence of aromatic components that endow them with graphitization potential.[95] For wood, there is a significant presence of aromatic lignin, in addition to polysaccharides such as cellulose and hemicellulose, with relative amounts dependent on the type of wood and tree species, leading to distinct graphitization potentials. This was first reported in the pioneering work by Ye et al.,[125] where pine, birch, and oak wood sources were used for LIG synthesis. Because of the higher relative concentration of lignin in pine, a lower degree of defects in LIG structures is achieved, as well as attractive sheet resistance around 10 Ω $sq^{-1}$. However, as denoted in this work, the significant fraction of aliphatic carbon, arising from polysaccharides, diminishes the stability of the material for graphene induction. Polysaccharides tend to completely decompose upon irradiation, instead of participating in the carbonization and graphitization process. To avoid this, the authors employed an inert $Ar/H_2$ atmosphere, to decrease the oxidative and combustive behavior of the photothermal effects promoted by the laser irradiation. Since then, several strategies have been put forward to avoid the use of a less accessible inert atmosphere. These include the use of femtosecond lasers, that allow for an increased control of temperature and resulting photothermal processes leading to graphitization, decreasing the decomposition of aliphatic phases in wood and other materials, such as leaves.[223,299] Another approach is to perform chemical treatments of lignocellulosic precursors, including fire-retardants[104] and catalyzing inks.[217] In the work by Dreimol et al.,[217] an iron-tannic acid ink, made with gum arabic and glycerol, is used to enable conversion into high-quality, conductive graphitic materials, promoted by the aromatic tannic acid and the presence of iron (Figure 15g). Iron appears as a crucial component, due to the formation of iron carbide NPs, as surveyed by TEM imaging (Figure 15h,i) The authors propose that these carbide NPs promote graphitization in opposition to the formation of amorphous carbon. This way, $CO_2$ lasers can be readily employed for the graphitization of wood materials, making this process much more accessible. Besides wood, other vegetable biomass sources have appeared as highly efficient precursors. One of the most prolific has been cork, due to the abundant presence of not only lignin but also suberin, an aromatic–aliphatic cross-linked polymer, that improves the relative aromatic content in this material. Several approaches have been used for cork graphitization and pattern by DLW, using $CO_2$,[272] UV, and[274] IR-fiber lasers.[273] The use of fire-retardant chemicals has also been attempted.[226] Sheet resistances comparable to wood have been achieved using cork substrates, with the lowest value reported in the literature of 7.5 Ω $sq^{-1}$[273] using waxed cork substrates and a 1064 nm fiber laser.

Inspired by the graphitization potential of lignin, isolated forms of this component have also been employed for LIG production. In most cases, lignin has been used within polymeric composite sheets, where the concentration of lignin can be studied for optimized irradiation outcomes. Such polymers include PVA,[276,278,300] PES,[301] poly-L-lactic acid (PLLA),[302] and polyethylene oxide (PEO).[277,303] Several lignin sources have also been targeted, including kraft lignin,[277,278] alkali lignin,[302,303] and lignosulfonate.[276,279,304] Very attractive properties of resulting LIG can be achieved using such formulations, such as sheet resistances as low as 2.8 Ω $sq^{-1}$[276] and conductivities as high as 66.2 S $cm^{-1}$.[275] Besides these polymers, other materials have been used to disperse lignin, where cellulose-based materials stand out. This way, lignocellulosic matrices can be mimicked, with the benefit of controlling the relative concentration between aromatic and aliphatic components. One example is the work by Yuan et al.,[304] where lignin is dispersed in a hydroxyethyl cellulose slurry. Another similar approach was presented by Edberg et al.,[279] where a similar lignin/hydroxyethyl cellulose formulation also including boric acid fire retardant is employed as a high-efficiency LIG precursor, used in conjunction with screen-printing for patterning. Low sheet resistances of 3.8 Ω $sq^{-1}$ are reported, translating to a conductivity of 28 S $cm^{-1}$. Thus, lignin has turned into a valuable resource in several DLW graphitization routes, used either as the sole graphitizable element or to improve the graphitization potential and add functionality to graphitizable substrates.[305]

#### 4.5.3. Polysaccharide-Based Materials

Arising from different biomass processing chains, polysaccharides have appeared as interesting LIG precursors, due to intrinsic properties that make them attractive for degradable and biocompatible electronics. The first major polysaccharide used for this purpose was cellulose, within paper substrates. However, as previously stated, laser irradiation of cellulose in wood using $CO_2$ lasers results in complete degradation and combustion, showing that on its own, cellulose does not present apparent graphitization potential. To circumvent this, the use of several fire retardants has been the main strategy of choice, allowing for an increase in the thermal resistance of cellulose substrates and the formation of chars and graphitized products, depending on the treatment and irradiation scheme. Fire-retardant chemicals have been employed, either commercial or custom-made formulations. These include ammonium sulfamate,[43,280] ammonium phosphates,[104,225,281,306] boric acid,[307] and sodium tetraborate.[116,117,220,308] Depending on the fire retardant, different mechanisms may occur upon their decomposition under laser irradiation, but they commonly promote the transformation of cellulose chemical structures into chars, instead of their complete degradation. As such, initial reports stated that to achieve graphitization of paper, the application of more than one laser irradiation cycle was needed, to promote an initial char formation, while subsequent laser scanning promoted the build-up of graphene lattices, characteristic of graphitization.[95,280,307] As such, even with the use of fire-retardant treatments, the graphitization potential of this polysaccharide is much lower, when compared to aromatic precursors. Different works report higher sheet resistances of resulting LIG, such as the work by Park et al.,[280] where the authors reached a minimum value of 61.5 $\Omega\ sq^{-1}$, or the work by Kulyk et al.,[281] where a minimum value of 32 $\Omega\ sq^{-1}$ was reached. Similarly, other forms of cellulose have been employed, resulting in more resistive LIG, including cellulose nanofibers films[84,132] and cellulose nanocrystals.[285] Recently, novel approaches have been employed to improve conductive properties and boost the graphitization potential of cellulose-based precursors, resorting to modification with not only fire-retardants but also aromatic-rich components. One straightforward solution is the reintegration of lignin within paper, to reach compositions close to lignocellulosic materials.[283,284] Besides lignin, alternative sources can be employed for a similar effect. Dreimol et al.[217] employed the same iron-tannic acid ink used to improve wood processability to modify paper substrates, with good prospects in improving the properties of paper-derived LIG. Another proposed solution has been wax printing, a technique that introduces colored wax loaded with aromatic pigments within the porosity of paper substrates.[116,220] With a complete wax loading of paper porosity, boosted graphitization potential is demonstrated, due to the increased aromatic content and overall carbonizable material in this composite precursor. LIG properties in the same order of magnitude as high-efficiency aromatic precursors were reached, with minimum sheet resistance around 5 $\Omega\ sq^{-1}$ translating to conductivities of 24.3 $S\ cm^{-1}$. In addition, modification methods allow for the use of other functionalities of paper substrates simultaneously with LIG functional patterns. Taking advantage of the capillary properties of paper, Bezinge et al.[43] constructed paper-based electrofluidics, designed for bio-electrochemical analysis. Resorting to the biodegradable properties of cellulose, Jung et al.[282] focused on developing LIG sensing elements within smart-packaging systems, designed to be easily disposable without a significant environmental footprint, while providing the capability to monitor food spoilage.

Other novel polysaccharide sources have steadily been rising as compatible materials for DLW processing. The first example is hemicellulose, the remaining by-product of wood processing. In the work by Kulyk et al.,[286] xylan, a common form of hemicellulose, was successfully graphitized for the formation of conductive LIG. However, like cellulose, the resulting properties show a lower potential for graphitization, with more resistive LIG films with sheet resistances of 182 $\Omega\ sq^{-1}$. Maintaining the same principles of polysaccharide chemical treatments for DLW processability, chitosan has also recently appeared as a precursor of interest. Analogous to cellulose, most reports of chitosan-derived LIG show the need for an efficient control of laser irradiation schemes and resulting temperatures, to initiate char formation and subsequent graphitization.[221] As such, initial proposed experimental procedures employ multiple irradiation cycles until the chitosan precursor is efficiently graphitized.[288] Other reports show the capability for one-step induction, where the chemical structure of the chitosan precursor is a key variable to achieve maximized properties of resulting LIG. Huang et al.[221] used three chitosan derivatives, namely carboxymethyl chitosan, a chitosan oligosaccharide, and chitosan hydrochloride, successfully implemented in DLW processing schemes (Figure 15j). However, the resulting outcomes of each derivative are different, both in terms of the chemical characteristics and resulting conductive capabilities. The authors used the duty cycle as the main process-property optimization metric to assess the effect of laser irradiation over the resistivity of the chitosan-derived LIG films (Figure 15k–m). While for carboxymethyl chitosan a highly resistive film with a minimum sheet resistance of 2.2 $k\Omega\ sq^{-1}$ was reached (Figure 15k), for the chitosan oligosaccharide film and chitosan hydrochloride, the sheet resistance dropped to 33.9 (Figure 15l) and 12.7 $\Omega\ sq^{-1}$ (Figure 15m), respectively. This shows the great potential for this polysaccharide for biodegradable and biocompatible electronics, opening routes to explore different formulations and chemical compositions of distinct polysaccharide sources for DLW.

### 4.6. DLW Processing of Conductive Polymers

Conductive polymers have been considered as promising candidates for flexible device development,[309] due to their low toxicity, mechanical flexibility, low cost, and easy solution processability.[310] Because of this, processing of conductive polymers using DLW paradigms has been attempted with different purposes, from direct laser polymerization[311,312] to tuning of polymer conductivity and selective phase changes for improved functionality.[309,310,313,314] In this regard, poly[3,4-(ethylenedioxy)thiophene] (PEDOT) and its mixture with polystyrene sulfonate (PEDOT:PSS) have been the main target of laser processing studies, while other conductive polymers remaining less explored. Regarding direct polymerization and synthesis of conductive polymers, two studies can be highlighted. In the work by Luo et al., the polymerization of PEDOT from its

EDOT monomer is reported, resorting to a 532 nm femtosecond laser.[311] Using this ultra-short laser system, nanopatterning of PEDOT wires can be performed, down to 140 nm in width, also with a conductivity of $1.28 \times 10^3$ S cm$^{-1}$. Among the several interesting properties of PEDOT:PSS, the ability to tune its conductivity or transmittance by DLW has been explored.[309] PEDOT is a positively charged chain, whereas PSS is negatively charged. The latter is a surfactant with a dual role, acting as a charge balancing counterion and PEDOT dispersant in aqueous media. However, the presence of PSS decreases PEDOT's conductivity.[310] In its more frequent configuration, PEDOT:PSS presents a structure with an island-like distribution, where the conductive PEDOT domains are surrounded by insulative PSS shells, blocking charge flow.[309,313] Several works have reported different approaches to improve the electrical conductivity of PEDOT:PSS films through laser exposure. Although the proposed mechanisms differ among them, some points are similar. Briefly, laser exposure disrupts the stability of the PEDOT:PSS system causing changes in PEDOT configuration from a benzoid to quinoid structure, i.e., the transition from a coiled to an extended coil or linear structure. Moreover, the PSS shells are fragmented and migrate from the PEDOT surroundings, allowing these units to merge, stimulating charge transportation, and enhancing conductivity.[309,310,313,315] Among the mentioned approaches, one presented by Kalachyova et al.[309] includes chemical modification of PEDOT:PSS films with 4-nitrobenzenediazonium tosylate, causing the creation of bonds between arenediazonium cations and the $SO_3^-$ present in the PSS chains. The ability to create and erase conductive patterns is based on the reversible light-triggered E/Z isomerization of the trans-isomer of 4-(nitrophenyl) azo groups. This isomerization process is accompanied by spatial redistribution within the PEDOT:PSS film since PSS also contains diazo-containing moieties and will be affected by laser exposure. Scanning chemically modified films with a 430 nm laser removes the PSS chains from PEDOT surroundings and the subsequent merge of the PEDOT domains creating a conductive pattern. This pattern can then be removed by exposure to a 490 nm laser, which returns the azo bond to E-configuration and the PSS chains to wrap the PEDOT domains. The possible mechanisms behind reversible PSS movement were suggested to be gradients in temperature, electric force or permittivity, isomerization pressure, asymmetric diffusion-related forces, or mean-field chromophore–light interaction. In another approach proposed by Wang et al.,[310] the conductivity of PEDOT:PSS films drop-casted on PET substrates was tailored using a femtosecond laser ($\lambda$ = 1030 nm). The underlying phenomena behind improved conductivity were pointed out to be changes in PEDOT conformation, reduction of interplanar stacking distance, and PSS removal (**Figure 16a**). The described mechanism stated that electron-photon interactions were accompanied by carrier excitation and delocalization of the conjugate backbone in PEDOT, leading to changes in its conformation. Electron-phonon scattering process also occurred, generating localized shock pressure, which caused the reduction of PEDOT $\pi$- $\pi$ stack spacing, stimulating carrier hopping between PEDOT chains and enhanced electrical conductivity. When the accumulated localized heat, resulting from photon-electron and electron-phonon interactions, surpasses the Coulombic interaction between PEDOT and PSS, the partial removal of the surfactant takes place, promoting the separation of the positively and negatively charged domains. This process was proposed to expedite charge transfer between and within PEDOT chains, improving the films' conductivity, dependent on laser fluence (Figure 16b), but independent of the resulting processing temperature (Figure 16c), confirming the photochemical nature of the process. An improvement in conductivity up to 803 S cm$^{-1}$ was achieved, allowing for the patterning of conductive lines with 10 µm spacing on PET substrates. In another work by the same group, similar processing using ultrashort pulse lasers further improves the conductivity of PEDOT:PSS up to 1024 S cm$^{-1}$, while showing tunable transmittance when compared to the pristine PEDOT:PSS film (Figure 16d).[316] Depending on the laser power, both the conductivity and transmittance of the laser-treated area can be tailored (Figure 16e), up to 98% transmittance paired with a conductivity of 191 S cm$^{-1}$.

Improvements in conductivity and water stability of PEDOT:PSS hydrogels through laser-assisted phase separation using a 532 nm continuous-wave laser have also been reported by Won et al. (Figure 16f–i).[315] Here, the laser was presented as a simultaneous source of electric field and photothermal energy. While the latter disrupts the stability of the PEDOT:PSS system, the electric field promotes the separation of the two domains, followed by the interconnection between PEDOT domains leading to improved conductivity (Figure 16g) and water stability (Figure 16h,i). Through AFM analysis, the authors showed the difference between the initial PEDOT:PSS organization and the one resulting after laser irradiation. Initially, the film is composed of small and isolated PEDOT domains, surrounded by PSS-rich domains (Figure 16j(1)). After laser processing, PEDOT domains expand and there is less presence of PSS (Figure 16j(2)). Depending on laser power, the relative concentration of PEDOT/PSS domains is tunable up to 1.2 times more PEDOT than PSS (Figure 16k). Change of PEDOT from a benzoid to a quinoid conformation is also reported. It is worth mentioning that AuNP ink was blended in the hydrogels to intensify the interaction with laser radiation. However, the hydrogels' conductivity decreased above a particular AuNPs concentration, since PVP is present in the ink composition, and this chemical species is an electrical insulator. As so, the final properties of the hydrogels can be tuned by determining AuNP concentration and laser processing parameters, reaching a conductivity of 670 S cm$^{-1}$ at a 6 µm pattern resolution in a swollen hydrogel operation (Figure 16l). It is worth noting the compatibility of this technique with multiple flexible substrates such as soft styrene-butadiene-styrene, polyurethane, and PDMS. Improvements in spin-coated PEDOT:PSS films' conductivity using a 1.07 µm wavelength CW ytterbium fiber laser have also been demonstrated by Yun et al.[313] The differential absorption of laser energy by PEDOT and PSS domains was presented as the central phenomenon behind the improved carrier transport properties. Briefly, when exposed to laser radiation, the PEDOT domains heat due to absorption. Then, these domains transfer energy to PSS shells causing their fragmentation and subsequent reorganization. Then, the PEDOT domains merge, reducing the carriers' hopping distance and thus enhancing the films' electrical properties. Films with different thicknesses were produced, and the thicker ones required lower laser powers to undergo conductivity changes. Optimal laser power was found for each film

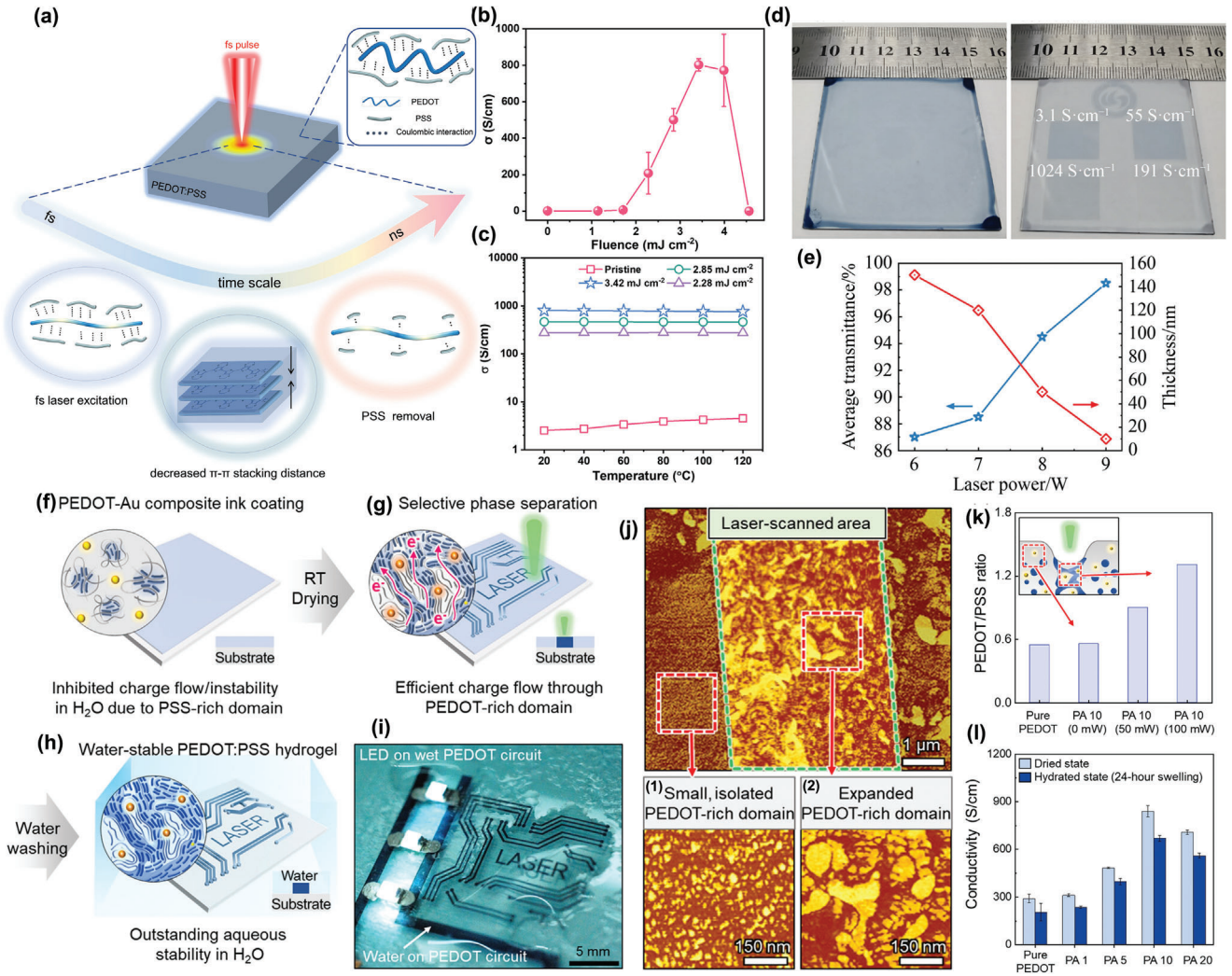


**Figure 16.** DLW processing of conductive polymers. a) Mechanisms of PEDOT:PSS conductivity improvement using a femtosecond laser. b) Laser fluence dependency on conductivity improvements. c) Conductivity of laser-modified PEDOT:PSS depending on temperature and laser fluence. Reproduced with permission.[310] Copyright 2023, Wiley-VCH. d) Images of pristine and laser-modified PEDOT:PSS films with varying laser power and resulting conductivity. e) Variation of film transmittance and thickness for different laser powers. Reproduced with permission.[316] Copyright 2023, Springer Nature. f–i) Laser-induced phase separation process of PEDOT:PSS/gold NP films. j) AFM images of PEDOT:PSS before and after laser writing. k) Influence of laser power on the PEDOT/PSS ratio. l) Influence of gold NP concentration of conductivity of laser written PEDOT. Reproduced with permission.[315] Copyright 2022, American Association for the Advancement of Science.

thickness, above which the film's integrity was compromised. Areas with different patterns and predetermined conductivity could be produced in the same flexible substrate with this method by controlling the laser parameters, up to 931.9 S $cm^{-1}$. Moreover, the sheet resistance of pristine PEDOT:PSS films (62–113 kΩ-$sq^{-1}$), deposited on glass, PET, and PDMS substrates, was improved after laser exposure. A minimum sheet resistance of 96.1 Ω.$sq^{-1}$ was achieved for a laser power equal to 1.6 W.$cm^{-2}$.[313] Another study also reported the influence of laser processing parameters on the conductivity processed using a 1064 nm CW Nd:YAG laser. The laser was scanned along the samples at different line gaps, resulting in different overlaps between lines. The results of the performed study revealed that above a specific laser power, the sheet resistance decreased from multiple kiloohms to a few hundred ohms, and an average conductivity of ≈900 S $cm^{-1}$ for the irradiated area was estimated. The results were used to design a model to predict the spatial distribution of the films' conductivity after laser exposure, important for future use of such DLW techniques for functional electronic element fabrication.[314]

### 4.7. DLW Synthesis of Hybrid and Composite Materials

Another attractive feature of DLW processing frameworks is the capability to synthesize multifunctional hybrid and composite materials composed of different conductive or semiconductive phases. By combining different inorganic precursors or mixing them with organic materials, photothermal and photochemical stimuli can promote the simultaneous occurrence of different

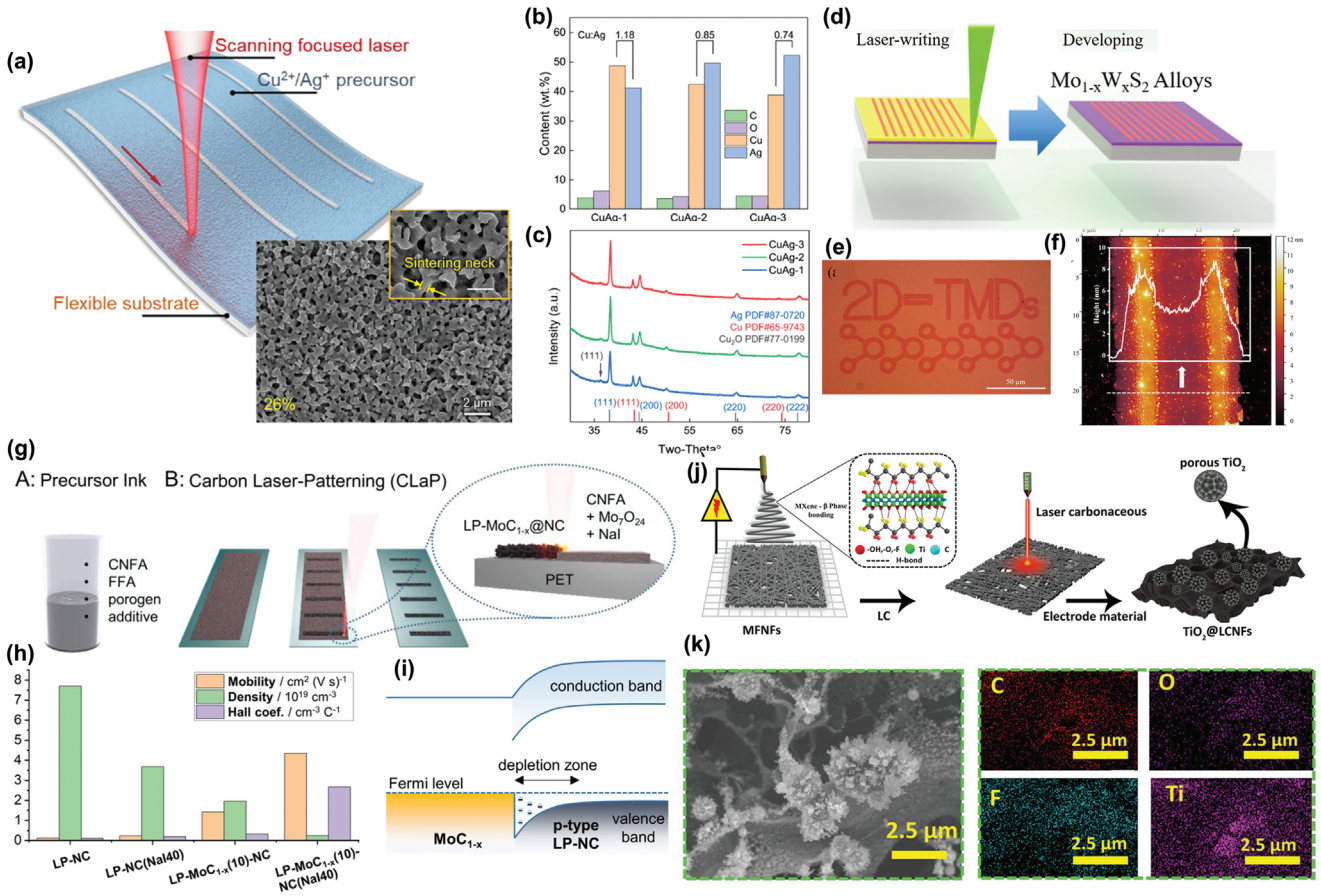


**Figure 17.** DLW synthesis of alloys, hybrid and composite materials. a) Writing conductive silver/copper metal alloys by laser-induced reduction of metal ion precursor mixture. b) Relative silver and copper content and c) XRD spectra of written films depending on initial precursor formulation. Reproduced with permission.[164] Copyright 2023, American Chemical Association. d) Laser writing of TMDC alloys. e) Image of TMDC alloy pattern and f) AFM analysis of a written line. Reproduced with permission.[255] Copyright 2023, Elsevier B. V. g) DLW carbonization for $MoC_{1-x}$/nitrogen-doped carbon synthesis and patterning. h) Varying semiconducting properties of components within the laser synthesized composite material and i) band diagram for the junction between carbonized and $MoC_{1-x}$ phase. Reproduced with permission.[216] Copyright 2021, Wiley-VCH. j) Electrospinning of a fluoropolymer/Mxene precursor for the synthesis of conductive carbon/Mxene/$TiO_2$ composite material. k) SEM imaging and EDS elemental mapping of the composite. Reproduced with permission.[317] Copyright 2023, Wiley-VHC.

synthesis mechanisms. Several works report the synthesis of alloyed materials using one-step synthesis approaches. In the work by Zhou et al.,[164] ionic precursor mixtures with different volume ratios of copper and silver nitrate were used to produce highly conductive copper/silver alloy electrodes on a flexible substrate (**Figure 17a**). Control of each precursor phase leads to alloys with tailored weight content percentages for each metallic component (Figure 17b), as well as polycrystalline features arising from each metal phase in the resulting alloys (Figure 17c).

Similarly, laser irradiation procedures can be used to produce metal/metal oxide composite material, either by control of laser parameters[168,171] or the precursor mixture.[181,182] One example is the work by Mizoshiri et al.,[181] where a mixture of CuO and NiO NPs can be used to fabricate hybrid metal oxide films with defined semiconductive behaviors, through reductive sintering mechanisms. Depending on the employed laser fluence of a 780 nm femtosecond laser, either n-type or p-type semiconductor oxide composites can be produced, used in this case for thermoelectric sensor fabrication. Multi-metal oxide alloys synthesized by laser oxidation of solution-processed metal ions precursor by femtosecond laser irradiation have also been reported by Hegde et al.[318] For TMDCs, laser-induced synthesis of $Mo_{1-x}W_xS_2$ alloys with adjustable composition has been reported by Averchenko et al. (Figure 17d).[255] The laser-induced photothermal dissociation precursor films lead to the formation of these alloys, whose composition is tuned by varying the precursors' volume ratio. The mixed precursor solution composed of ammonium tetrathiomolybdate and ammonium tetrathiotungstate was scanned with a CW laser ($\lambda$ = 532 nm), resulting in homogeneous TMDC alloy patterns (Figure 17e). As expected, the thickness and dimensions of the alloys' features are dependent on the laser processing parameters. Different conditions were tested and the maximum width of $Mo_{0.5}W_{0.5}S_2$ samples was 18.2 μm when a laser power of 950 mW and a scan speed of 2 mm $s^{-1}$ were employed. The narrowest width (3.73 μm) was achieved in the sample produced using the lowest power and fastest speed (450 mW and 20 mm $s^{-1}$). However, ununiform thickness characterized these lines, with

a central height of 4 nm and an edge height of ≈7–8 nm (Figure 17f).

Another possibility for one-step laser-induced hybrid material synthesis has been the combination of organic and inorganic materials. This allows for the combination of different laser-material processing mechanisms, within simple synthesis frameworks. The main example has been the doping of LIG with different metallic and metal oxide nanostructures, leading to composites with unique catalytic properties, appropriate for different applications, from energy storage to sensing.[319] The first approach to synthesizing such composite materials is the deposition of a metal precursor phase over the graphitizable substrate, using solution processing approaches.[170,320–324] A second approach is the formulation of liquid composite precursors, that present both the organic, LIG precursor phase and the metal precursor simultaneously.[325–327] Using both strategies, LIG-based composites with metallic elements have been produced, using the thermal laser stimulus to simultaneously graphitize the carbon organic precursor and reduce or oxidize the metallic precursor. Doped structures with metal NPs such as silver,[328] platinum,[327] and copper[170] have been synthesized. For metal oxide elements, zinc oxide,[325] cobalt oxide,[321] manganese oxide,[329] and vanadium oxide/LIG[326] composites have been produced. To note the work by Yang et al., in which the authors developed a versatile precursor formulation employing block copolymer-phenolic resin custom-made films as LIG synthesis phase, doped with vanadium sulfide ($V_5S_8$). Upon laser irradiation, concurrent graphitization of the organic phase occurs while vanadium precursor suffers oxidation and leads to the formation of embedded $VO_X$ NPs, with interesting semiconducting and bandgap properties for gas sensing applications. Besides metal and metal oxide embedded phases for LIG-based composite synthesis, concurrent synthesis of other semiconductor materials has been explored, including chalcogenides such as hafnium diselenide[323] and molybdenum disulfide.[324] Based solely on carbonization mechanisms, the writing of LIG doped with several carbides has also been explored. Molybdenum carbide nanostructures embedded in conductive carbon have been reported using paper substrates[257,258] by soaking the cellulose matrix with molybdenum metal ions. Another work by Wang et al.[216] resorted to a custom-made formulation using a carbon-network forming agent (derived from citric acid and urea) and the molybdenum ion precursor (Figure 17g). The different phases of the resulting composite present different semiconducting characteristics, regarding their charge mobility density and hall coefficient (Figure 17h), resulting in the presence of spread heterojunctions between the carbonized and the metal carbide phases. Ultimately, this creates depletion zones around MoC NPs within the composite, characteristic of Schottky-junctions (Figure 17i), that increase the sensitivity in gas sensing applications. Another interesting approach is based on the modification of PET substrates with aluminum NPs, to produce patterns made of conductive carbon and aluminum carbide,[259] endowing the resulting composite with great mechanical resilience, as well as good electrical conductivity.

Besides these approaches, different material classes with more complex chemical compositions and arrangements have been proposed for DLW synthesis of composite structures. Metal–organic frameworks (MOFs) are an example and have been used to write conductive metal alloy NP patterns.[330,331] Another possibility is using these crystalline, high-porosity materials to produce conductive carbon/metal nanocomposites, where the organic components of MOFs are subjected to photothermal conversion, turning into laser-induced MOF-derived carbon.[332] The embedding of MOF over a LIG precursor is also a possible fabrication strategy[296] for similar conductive carbon/metal composites. Besides MOFs, MXenes have also appeared as an interesting class of materials for DLW composite processing frameworks. MXenes can be employed using solution processing over polymeric LIG precursors, to synthesize LIG/MXene hybrids.[333,334] Embedding of MXenes within the carbonizable phase has also been attempted with success,[317] where the authors mixed a fluoropolymer that interacts with —OH, —O, and —F functional sites of the MXene phase, for subsequent use in electrospinning (Figure 17j). The electrospun film is then subjected to laser irradiation, to form $TiO_2$-rich laser-carbonized fiber membranes, with sheet resistances of 15.6 Ω $sq^{-1}$. The resulting composite is composed of porous, graphitized carbon fibers and unreacted $Ti_3C_2$ MXene surrounded by $TiO_2$, arising from the oxidation of the Ti phase of the Mxene (Figure 17k). Thus, direct irradiation of MXene films can also lead to the synthesis of Mxene/metal oxide materials, by laser oxidation of certain metal components of the Mxene phase.[335]

### 4.8. Implementation of ADLW and TDLW Mechanisms for Electronics Microfabrication

Based on the physical and chemical principles underlying the most common mechanisms used within DLW synthesis addressed before, several considerations are needed for efficient implementation of laser-induced material synthesis and conversion mechanisms within electronic devices. These pertain to preprocessing requirements, compatible laser systems, throughput capabilities, and morphological outcomes, beyond specific conductive or semiconductive properties. A statistical analysis of the employed laser system over the literature reviewed in Sections 3 and 4 is presented in **Figure 18**a, specific for the pulsing capabilities and laser wavelength selection. A preponderant use of pulsed lasers over CW lasers is visible. Within pulsed lasers, femtosecond lasers have also been progressively selected, since they offer additional capabilities that other ultra-short pulsed lasers, such as picosecond laser, do not possess, related to efficient TPA processing.[118] For laser wavelength selection, IR lasers have been preferred for multiple tasks, followed by visible lasers. UV lasers have been less explored, being mostly employed in experimental studies of irradiation processes and resulting material interactions and properties, and less in larger scale application.

In Figure 18b, a comparative analysis of processing windows for dominant irradiation parameters (laser power and scan speed) and resolution outcomes of these different laser categories is performed (average values reported in the reviewed literature for the analyzed parameters). In terms of processing windows related to laser power, authors have greatly resorted to IR and pulsed lasers in DLW processes, where photothermal mechanisms are dominant, showing higher power levels used in their works. However, IR lasers have also been used at low power regimens (0.5 mW[118] to 350 mW)[42] when paired

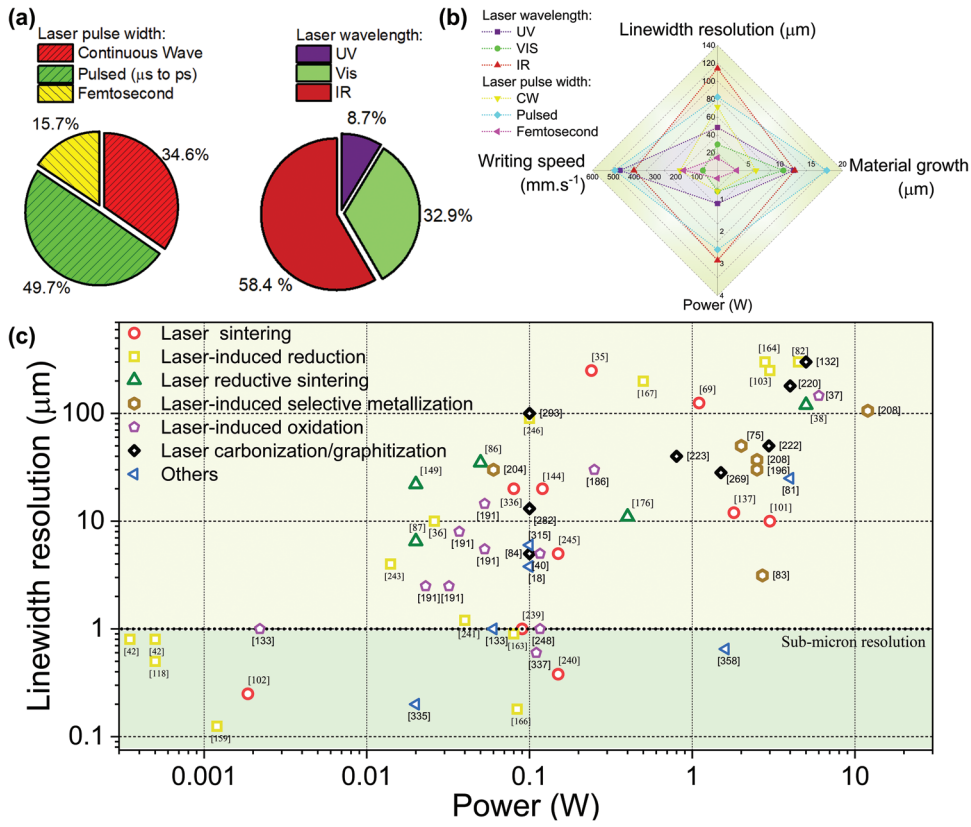


**Figure 18.** Literature analysis on laser systems, operational variables, resolution, and material growth figure of merit. a) Pie chart for statistical percentages of laser system in terms of beam time evolution and wavelength selection. b) Radar chart of operational irradiation parameters (Power and writing speed) and resolution outcomes (linewidth resolution and material growth thickness). Values are expressed as means of data reported for each laser category reported in the literature. c) Logarithmic plot of linewidth resolution (µm) versus operational power (W) for the reviewed DLW material synthesis and conversion mechanisms. The data is adopted from the literature in Tables 1–3 and the remaining works reporting linewidth resolution outcomes.

with femtosecond pulse width, designed for high-resolution metal writing. Thus, femtosecond lasers have the lowest requirement in terms of applied power, to reach efficient material processing for different processes, from laser-induced metal ion reduction,[42,118,159,160,166,241] laser nanoparticle sintering[240] and laser graphitization.[84,293] This also highlights the versatility of femtosecond lasers for participating in photochemical and photothermal processes, depending on the processable substrate. On the other hand, IR lasers are most used in the form of $CO_2$ laser systems, that ultimately participate in photothermal mechanisms, skewing the laser system's overall processing window to higher operating powers, along with lower pulse widths. Besides femtosecond lasers, CW lasers have also been a great tool for higher-resolution patterning at low power regimens (1.86 mW[102] to 250 mW),[186] usually paired with visible wavelength lasers, relying on finer regulation of writing speed to control laser-induced chemical changes, including SPA.[36,87,102,133,243,336]

Along with laser power, writing speed has a great influence in the resolution and material growth outcomes of laser material synthesis processes. The writing speed directly influences photon flux and cumulative photochemical and thermal interaction over the processing materials, but also dictates the throughput capabilities of laser processing and its suitability for different scale fabrication. As shown in Figure 18b, visible wavelengths, CW, and femtosecond lasers have been implemented with lower writing speeds, mostly in the micrometer per second regimen. Low speeds are usually associated with piezoelectric stages,[42,118,163] that limit the speed to around 100 µm $s^{-1}$.[118] Such writing speeds, paired with these pulsing capabilities and wavelengths, are associated with micrometer-range microfabrication of small area electronic components and conductive lines for circuit integration, being only compatible with implementation along microelectronics, for example within solution processable thin-film technologies.[8] Only at these scales, the low writing speeds are compatible with high throughput and fast fabrication of several components, and their possible seamless integration performed with laser tools. Notably, speed regimens going from 5 µm $s^{-1}$[42] to 10 mm $s^{-1}$[118] have allowed for high-resolution metallic conductor patterning by TPR mechanisms, showing that power and writing speed are not the sole variables. In this regard, several authors have demonstrated the synergistic dependence of precursor formulations, irradiation parameters, and optics hardware toward high throughput and high-resolution writing. For the optics hardware, sub-micron resolution is almost always accompanied by high numerical aperture (N. A.) and oil immersion lenses,[18,147,159,166] that focus the laser beam to sub-micron diameters. Using these optics hardware setups, resolution, thickness, and roughness of resulting laser-written microstructures can be

manipulated, even for other photochemical mechanisms, including single-photon photoreduction.[163] Regarding precursor formulations, mindful consideration of the target laser stimulus is needed, to provide efficient photon absorption or thermal accumulation for material writing. For TPR processes, the presence of surfactants and photosensitive reduction agents has been helpful in producing morphologically stable structures, with good fabrication throughput. An example is the work by Saha et al.,[118] where a silver metal ion ink with a photoresist as a photosensitive component increased the efficient writing speed to 10 mm $s^{-1}$ for TP-DLW of silver microstructures, increasing the throughput 1000-fold when compared to more common micrometer per second speeds. This greatly improves the prospect of scalability and large-cale microfabrication of electronic microcomponents, while still allowing for sub-diffraction writing.

For nanostructure-based ink precursors used in laser sintering and reductive sintering, nanoparticle size and their light absorption profiles are fundamental for efficient laser writing. Thus, for nanostructure inks and other liquid precursor formulations, pre-processing requirements are important. They encompass the synthesis of the ink components (e.g., homogeneously sized nanoparticle), control of ink viscosity, precursor concentration, surface tension, and weight ratios,[101] as well as the solution processing outcomes (e.g. resulting thickness of the precursor). After laser irradiation with a specific laser system, the combination of these factors dictates not only the writing resolution, but the material growth, in terms of its thickness (Figure 18b) and surface roughness. An example is the work by Barton et al.,[166] in which the use of an ionic surfactant (n-laurylsarcosine sodium) and a careful control of operational parameters of a femtosecond laser resulted in 30 nm thin silver structures with a surface roughness of 7 nm. For thermal-induced writing tasks, another aspect important for uniform material writing in terms of vertical resolution is the thermal diffusivity and conductivity of the support substrate, that can promote uniform heat distribution and flatter cross-sectional shapes.[149] Using these solution processing principles, higher material growth resolution has also been achieved for other mechanisms, such as laser-induced graphitization for LIG synthesis, employing liquid aromatic precursors, down to 590 nm.[79] Once again, material growth outcomes have also achieved the best resolution using femtosecond lasers, resulting in lower thicknesses after material synthesis and conversion.[18,166,240,337]

Grounded on specific method parameters and requirements for efficient laser writing of conductor and semiconductor materials, each specific mechanism has achieved varying figures of merit, in terms of resolution capabilities, reflected in the broad literature presented in the previous sections. A representation of these figures of merit is given in Figure 18c for the DLW material synthesis and conversion mechanisms presented in Section 3, relating the minimum linewidth resolution reported in several works, in relation to the operational power. A thorough analysis of the literature shows that sub-micron resolution has been achieved using different mechanisms, including laser-induced reduction, laser sintering, and laser-induced oxidation. Notably, most of the reports presenting sub-micron resolution are based on TPA and TPR mechanisms and resort to femtosecond lasers. The exception are the work by Komori et al.[163] and Geladari et al.,[102] where CW UV and visible lasers were employed for silver and gold writing, respectively. In terms of semiconductor writing, laser-induced oxidation mechanisms have less reports of sub-micron resolution. This may be a current bottleneck for miniaturization and large-scale fabrication of laser microelectronics solely by laser material synthesis or conversion methods. Associated with this, few reports have appeared where femtosecond lasers are used for laser-induced oxidation and metal oxide formation.[337] Besides laser-induced reduction by TP-DLW, laser sintering, and laser oxidation, no other mechanism in its different implementations has resulted in sub-micron resolutions. This is mostly due to the shift of dominance from photochemical to photothermal stimulus, such as in laser reductive sintering of oxide nanoparticles, laser-induced selective metallization, and laser carbonization/graphitization. Consequently, a trend of lower resolution with the increase of applied power is visible. Ultimately, a distinguishing feature between single/multi-photon absorption processes and photothermal dominant mechanisms can be set, regarding their implementation frameworks. For the former, the lower resolution capabilities indicate their better suitability with large-area applications, mostly for electrode fabrication or material doping, within energy harvesting or storage,[77,130,332,338–340] sensors and bioelectronic applications,[71,82,83,87,116,232] where micrometer features are more relevant in the vertical axis. The latter have shown better suitability for micrometer and sub-micrometer scale device fabrication, from metal contacts,[102,138] metal wiring[42,159] for connection and integrated circuitry and small semiconductor channels and heterostructures[36,37,337] for active functions within microfabricated electronic components and sensors.

## 5. DLW-Enabled Electronics

Because of the vast capability of synthesizing and engineering functional materials reviewed in the previous sections, DLW can be employed in the end-to-end prototyping and fabrication of several applications, including simple electrical interconnect designs and circuits, functional information processing components (transistors and memristors), energy harvesting and storage elements and sensing devices. In this section, recent progress in the application of material synthesis and conversion by DLW for the assembly of electronic devices is presented, divided by the most significant fields of application. The production of electronic devices was first based on clean room processes, however alternatives to these procedures have been widely explored in the past decades to shift into more time- and cost-effective processes. As such, the focus of the fabrication shifted from clean room to printing and coating processes, such as inkjet, flexography, gravure, screen printing and spray coating, doctor-blade, and dip-coating, respectively.[8,341–346] These approaches offer the possibility of depositing different materials on several rigid or flexible substrates. Furthermore, printing techniques allow patterning the materials while depositing them without material waste. However, depending on the printing process, limitations related to resolution, limited choice of materials to be deposited, and low printing speed may arise.[345] In this scope, DLW has gathered much attention as it offers the possibility of producing and simultaneously patterning different materials on several substrates with relatively good resolution in a short time without resorting to masks. In some application fields, DLW material synthesis and

growth is still in an early stage of development, and further research and breakthroughs are still needed to match conventional microfabrication technologies in terms of applicability. For other applications, large-scale DLW has already been established as a mature technology and there is extensive literature. As such, this section aims at i) expressing at what level DLW material growth principles have been implemented for specific application fields and what advantages are provided, ii) detailing which DLW synthesized materials have shown greater compatibility and functionality for each specific field, and iii) highlighting the most significant examples of implementation of DLW for each field of application, with an emphasis on significant breakthroughs regarding large-scale fabrication or high performance, noteworthy in the overall literature for each specific field.

### 5.1. Processing Electronics

#### *5.1.1. Thin-Film Transistors*

TFTs are a crucial component of microelectronic devices, switching or amplifying electronic signals. TFTs are three terminal field-effect devices, whose working principle relies on the modulation of the current flowing in a semiconductor placed between the source electrode and drain electrode. A dielectric layer is inserted between the semiconductor and a gate electrode, being the current modulation achieved by the capacitive injection of carriers close to the dielectric/semiconductor interface, known as the field effect.[347] In the last 15 years, reports of DLW employed in TFT fabrication have focused on fabricating constituent layers of those devices (mostly applied on contact electrode patterning) or improving their characteristics.[22,31,348–350,32,37,88,102,133,239,240,254] However, most of these works are from the last six years, showing a higher demand for low-cost production techniques and easier scale-up to large area manufacturing enabled by DLW paradigms.

In 2007, S. H. Ko et al. reported high-resolution organic TFT fabrication using selective laser sintering of inkjet-printed NP inks to produce the source and drain electrodes.[239] By applying this methodology, high-resolution TFTs with a small transistor channel length of 4.5 µm with a maskless lithographic method and ambient processing were achieved. These devices present a current on/off ratio of $10^4$ and a low saturation mobility of 0.01 $cm^2\ V^{-1}\ s^{-1}$. Four years later, Y. Son et al. published a novel arbitrary metal patterning method using a femtosecond laser to produce electrodes for TFTs by manipulating laser power and writing speed. Direct patterning of nanometer-range uniform metal lines with a minimum width of 380 nm was produced at 400 µm $s^{-1}$ and 150 mW, without mask processes or a nanoimprinting master mold.[240] This enables the fabrication of pentacene p-type TFTs with a channel length of 10 µm, showing an on/off current ratio of $10^5$. Also, J. Yeo et al. reported a non-vacuum, maskless, low-temperature NP ink laser digital direct metal patterning and their implementation on high-performance flexible organic field-effect transistor (FET) arrays, as depicted in **Figure 19a**.[88] To note the great retention achieved in the output (Figure 19b) and transfer characteristics (Figure 19c) of these flexible TFTs after 100 000 bending cycles, showing only slight drops in drain current, confirming the prospects for robust flexible TFT technologies based on this DLW strategy. P. J. Diemer et al. reported the first organic TFT in which the organic semiconductor layer was written using DLW, by photochemical conversion and annealing of a sol-gel indium nitrate precursor using a KrF excimer laser, to implement an $In_2O_3$ n-type channel made from this oxide semiconductor.[349] The laser-annealed $In_2O_3$ TFTs showed higher mobility (13 $cm^2\ V^{-1}\ s^{-1}$) when compared with the reference device annealed at a higher temperature (250 °C). In 2020, E. Carlos et al. tested the use of the same laser and similar procedure to produce a dielectric, aluminum oxide thin film, and implement it on indium gallium zinc oxide (IGZO) TFTs.[350] These devices presented great TFT properties, a high saturation mobility ($20.4 \pm 0.9\ cm^2\ V^{-1}\ s^{-1}$), a small subthreshold slope ($0.10 \pm 0.01\ V\ dec^{-1}$) and low operating voltage.

More recently, DLW has been applied to TFTs based on 2D materials.[22,102,133,254] In 2020, S. Park et al.[41] reported the writing of MoS2 and WS2 using spin-coated precursor for the fabrication of wafer-scale FET arrays. Relying on a linewidth resolution of 24.5 µm, the author employed an IR picosecond laser to pattern 40 × 40 array of rectangular MoS2 patterns (150 µm × 300 µm) over a $SiO_2$/Si wafer with varying thicknesses (2.2, 4.2 and 6.2 nm). Au/Ti contacts were used as source and drain electrodes in the FET construction (Figure 19d). The devices showed a great production yield of 90% and good performance characteristics (Figure 19d–e). These include a threshold voltage of 1.9 V, independent of the thickness of the semiconductor layer, on/off drain current ratios of $10^3$, and mobilities ranging from 2.17 to 6.39 $cm^{-2}\ V^{-1}\ s^{-1}$, depending on the thickness of $MoS_2$. Similarly, the same FET construction was replicated with a 7.2 nm thickness $WS_2$ layer, to construct p-type FET with a threshold voltage of −1.1 V and 1.2 $cm^{-2}\ V^{-1}\ s^{-1}$ mobility (Figure 19f). Besides the large area, wafer-scale fabrication, and high throughput fabrication (5 min at a writing speed of 5 mm $s^{-1}$), the authors demonstrated comparable performance with other conventional TMDC synthesis processes, such as CVD, regarding FET performance. In 2021, O. A. Abbas et al., reported a direct, spatially selective synthesis of solution-based single source precursors to pattern 2D TMDC ($MoS_2$, $WS_2$ films, and their heterostructures) by laser under ambient conditions for similar implementation in TFT channels.[254] In the same year, C. Zhu et al. demonstrated the use of laser irradiation (CW 532 nm laser) to control the p-type doping of $WSe_2$ to apply in TFTs and logic circuits. By optimizing the laser power density, scan speed, and the number of irradiation cycles, different levels of p-type doping can be reached.[22] Compared with other doping techniques of 2D materials, this laser doping methodology presents an easy and flexible approach for the fabrication of 2D logic circuits. In 2023, O. Geladari et al. showed the use of DLW to produce ink-based gold structures instead of silver.[102] DLW enabled electrical gold wiring of 2D van-der-Waals materials with sub-µm structures and 100 nm interspacing resolution. Then these materials were applied to the fabrication of photo switches and field-effect transistors on different substrates. Recently, the synthesis of metal oxides by DLW has gained traction with TFT fabrication. Wang et al. selectively oxidized vanadium sulfide films into $VO_2$ and used this localized oxidation to fabricate transistors composed of $V_5S_8$–$VO_2$–$V_5S_8$ Mott memristor and n-type $MoS_2$ channel.[133] Abrupt switching transfer characteristics were reported, due to the interfacing of the laser-written switchable memristor and the n-type TMDC channel. Bae et al. employed a photon-pen

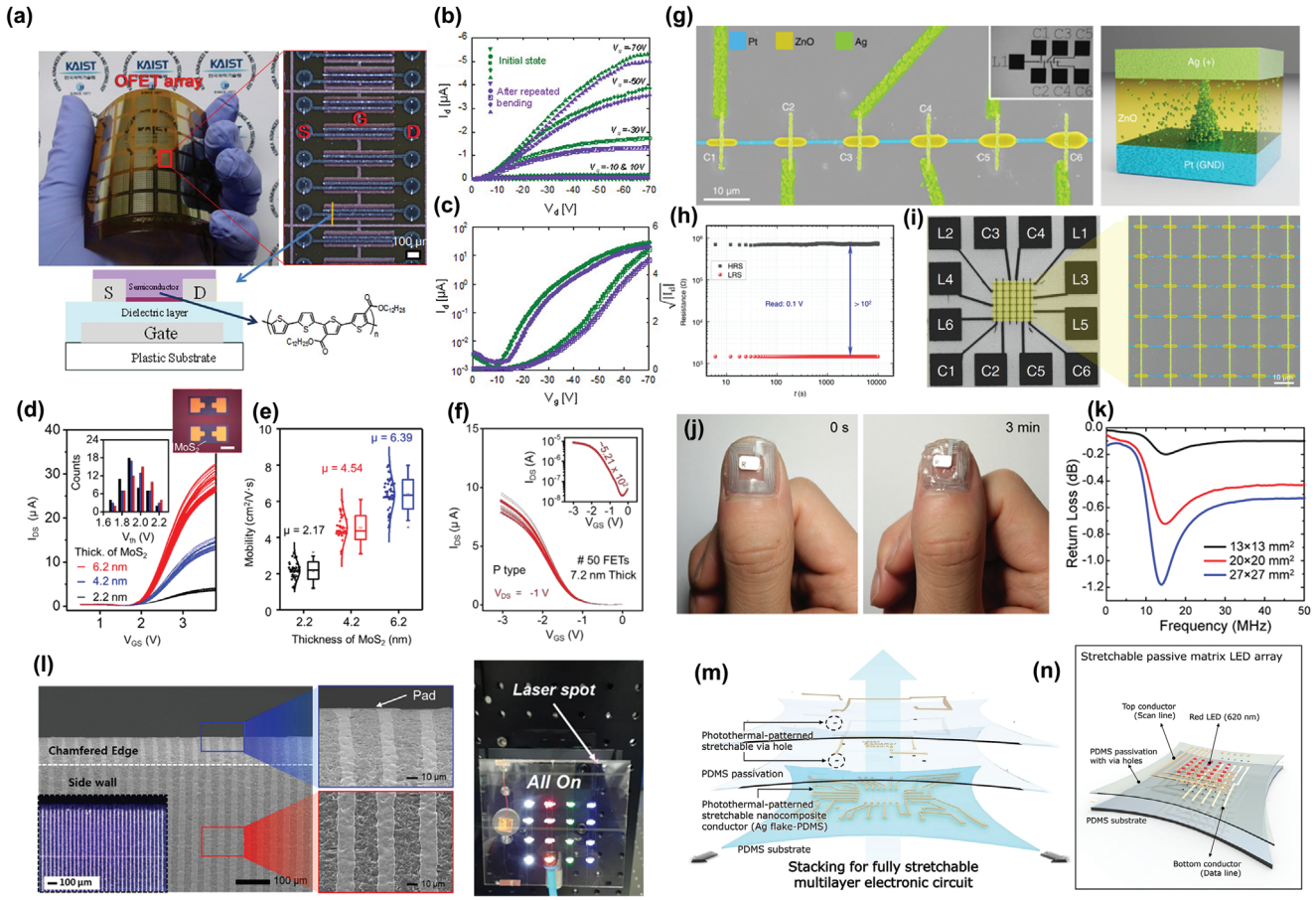


**Figure 19.** DLW microfabrication of information processing and electrical interconnect elements. a) Multilayer silver micropatterning of OFET arrays on PI and cross-sectional structure of the OFET. Output (b) and c) transfer characteristics of OFET before and after 100 000 bending cycles. Reproduced with permission.[88] d) Transfer curves of laser-written n-type $MoS_2$-based FET devices. e) Distribution of mobilities of n-type FETs. f) Transfer curve of laser-written p-type $WS_2$ FETs. Reproduced with permission.[41] Copyright 2020, American Chemical Society. g) 1 × 6 crossbar memristor array and corresponding work mechanism of memristors fabricated by DLW laser printing of Pt, Ag, and ZnO. h) Retention performance of high and low resistive states (HRS and LRS) of memristors on a time scale of $10^4$ seconds. i) 6 × 6 crossbar array for security circuit on a physically unclonable function. Reproduced with permission.[42] Copyright 2023, Springer Nature. j) Disintegration process of fingernail-sized NFC tag after a gentle spray of water. k) Return loss curve for MHz frequency range for different NFC tag dimension. Reproduced with permission.[69] Copyright 2019, American Chemical Society. l) Silver laser sintered electrical interconnects over the side wall and chamfered edge of glass substrates. k) Connection of LED array and lithium battery over both surfaces of glass substrate for lean electronics. Reproduced with permission.[101] Copyright 2020, American Chemical Society. m) Schematic of stretchable multilayer electronic circuits by DLW photothermal lithography of Ag flakes/PDMS ink and laser ablation for via hole patterning. n) Schematic illustration of the stretchable passive matrix LED array. Reproduced with permission.[35] Copyright 2023, American Chemical Society.

writing principle based on DLW of metal ion precursors to fabricate a ZnO channel in field-effect transistor architecture.[37] As it stands, DLW has been employed for the synthesis and fabrication of all the necessary constituents of TFTs, from source, drain, and gate electrodes,[351,352] dielectric layers to various semiconductor channel implementations. It is expected that further studies of DLW will improve the flexibility of transistor studies, based on all laser microfabricated, monolithically integrated TFTs. In addition, the high compatibility of DLW with solution-processing schemes, specifically spin-coating, will further promote the use of DLW in solution-based TFT processing[8] beyond micromachining or laser annealing. Along these processing lines, lasers present benefits when compared to conventional lithographic methods, such as photolithography, stencil lithography or electron-beam lithography, starting with not requiring subtractive processes, which can benefit throughput and allow the use of sensitive semiconductors and dielectrics. However, sequential DLW of TFT components and miniaturization of TFT features, such as channel lengths or gate-to-contact overlaps is still desirable to establish DLW material growth as full-scale fabrication tool, along with lithographic, solution processing, and printing techniques.[8,353]

### 5.1.2. Memristors

The memristor is a non-linear two-terminal device, which was predicted by Chua from the theoretical study of symmetries in electrical devices and circuits and is considered the fourth fundamental passive electrical element besides the resistor, capacitor, and inductor. This component relates to the electric charge and magnetic flux linkage.[354] Memristors are emerging electronic

devices that provide key features to combine memory and computational elements at the same location leading to higher densification and low power consumption.[355] These devices exploit the RS phenomena to store data. This feature consists of the change of their electrical resistivity between different stable levels when a specific electrical stress is applied. The RS present between two or more resistive states allows new types of devices for digital applications, such as neuromorphic and quantum computing.[356]

In 2012, DLW started to be implemented in memristors also called RS devices. In this work, H. Kim et al. studied the use of an excimer laser (KrF, 248 nm) annealing to produce solution-based NiO thin films and their application in memristors.[357] Specific areas of these films were exposed to laser irradiation for just 3 min, resulting in the fabrication of NiO memristors with a resistance window of $10^3$. More recently there has been a greater interest in using DLW on this kind of device due to their emergent and potential applications.[42,115,133,358–362] In 2023, Y. Dai et al. reported the use of femtosecond DLW to produce crystalline $Ge_2Sb_2Te_5$ nanobelts as active layer for the memristors.[358] The size and roughness of the nanobelts are strongly defined by the laser fluence. The best condition led to nanobelts with a width of ≈600 nm using the laser fluence of 15.4 mJ $cm^{-2}$ and was integrated into memristor devices. These devices present an on/off ratio of ≈7000, which is hundreds of times higher than the typical two-dimension GST films in the *fcc* phase. This work proves the capability to improve the performance of memristors with one-dimensional materials. In 2021, B. Wang et al. studied an ultrafast method to simultaneously synthesize and pattern $VO_2$ on the time scale of seconds under ambient conditions through DLW on a $V_5S_8$ "canvas".[133] The synthesis of $VO_2$ was possible due to the ultrafast local heating and cooling process, resulting in controlled freezing of the intermediate oxidation phase during the relatively long kinetic reaction. Afterward, this film was applied in a Mott memristor based on a $V_5S_8$–$VO_2$–$V_5S_8$ lateral heterostructure. In 2022, M. Chen et al. proposed a lateral Pt/GO/rGO memristor with rGO by DLW and Pt as electrodes and GO as function material. These devices present an ultralow energy consumption of 200 nW and were implemented in a memristor array (5 × 1). This was tested in a reservoir computing network leading to a 95.74% accuracy in digit recognition showing their potential neural network computing applications. Also, S. Han et al. studied the effect of laser annealing on Al/ZnO/Al flexible memristors. Applying DLW on the ZnO layer leads to higher crystallinity and the generation of additional oxygen vacancies and oxygen ions improving the device's performance. These memristors operate for more than $2.5 \times 10^3$ cycles, showing an on/off ratio window of $10^4$ and retention of $10^4$ s. In the same year, P. K. Enaganti et al. demonstrated a simple and low-cost fabrication of LIG and LIG/$MnO_2$ memristor devices on a polyamide substrate.[362] One year later, J. Jones et al. showed the possibility of producing memristors devices by DLW patterning of copper precursor coating on plastic substrates using a low-power fiber laser.[115] The results demonstrated that high laser energy densities resulted in highly conductive patterns of metallic copper, whereas lower energy patterns resulted in copper oxide-rich patterns with significantly lower conductivity. This method showed as a proof-of-concept the production of flexible memristors with low operating voltage (±0.7 V) and a window of $10^2$. Recently, L. Yang et al. introduced TP-DLW printing using semiconductor (ZnO) and metal (Pt and Ag) inks, as a facile process for fabricating printed functional electronic devices (diodes, transistors, and memristors) with minimum feature sizes below 1 µm.[42] In this work, special attention was given to the high-resolution Pt/ZnO/Ag memristor devices with an effective device area of ≈0.43 $µm^2$ (Figure 19g). These devices present a great performance (high endurance and retention time, Figure 19h) and were implemented on 6 × 6 memristor crossbar architecture, as shown in Figure 19i. The circuit was utilized as a physically unclonable function, which is a hardware-based security primitive. This function generates a unique response upon stimulation by a challenge, comparable to a human fingerprint. Notably, this work demonstrates a stride in the monolithic integration of DLW-processed metal electrodes and metal oxide semiconducting channels for microelectronics. Further research and use of these principles would greatly benefit monolithically integrated micro-components fabrication, of not only memristors, but also of TFTs, realizing high-vacuum free, maskless processing within the Front End of Line (FEOL).

#### 5.1.3. Antennas

Antennas are fundamental elements within communication modules, ideal for integration into devices for future technologies within the IoT, that require wireless access, efficient communication with miniaturized designs, and low power consumption.[363] DLW can benefit the fabrication of such communication elements, by engineering several conductive materials with considerate form factors, which can be advantageous to meet many requirements, including modulated antenna designs and assemblies for specific applications, optimization of response and signal transmission, and easy incorporation with other functional elements., optimization of response and signal transmission, and easy incorporation with other functional elements. Fabrication and optimization of antennas at a research level has posed significant challenges, associated with the inefficiency of traditional lithographic or wet etching techniques for patterning, and metallization via vacuum systems, such as sputtering or evaporation.[364] These challenges limit overall performance optimization in different antenna fabrication frameworks, for flexible and even transparent devices.[364,365] The high prototyping potential of DLW-based techniques allows for a much more efficient study and optimization of several design and operation requirements, such as operation frequency band, bandwidth, gain, and overall antenna efficiency, with low-cost and reliable methods. However, when compared to conventional techniques, such as lithographic fabrication, DLW also poses some challenges, mostly associated with synthesized material morphology, including the interface with the substrate and surface uniformity, relevant when designing and simulating antenna models.[341]

In 2018, E. Balliu et al. studied selective laser sintering of inkjet-printed silver NP inks on paper substrates. Highly conductive silver patterns were utilized to fabricate a fully functional hybrid near-field communication (NFC) tag on a paper substrate.[146] This research was a step closer to the production of large-area flexible electronics with hybrid printing and laser processing frameworks. In addition, the laser sintering process was compared to conventional oven sintering, showing a much

higher sintering efficiency using laser methods. The limited temperature tolerance of the paper substrate for oven sintering shows the higher compatibility of laser to process heat-sensitive substrates without damage. In the same year, Yang et al. showed the application of three-dimensional LISM technology with polymer coatings. To make this, the substrate was coated with a polymer by spray, reaching a thickness of 50 µm. Then a laser was used to define the conductor pattern and induce the catalyst in the polymer layer. After the electroless copper plating, the final pattern was metalized.[366] This methodology was applied to produce different products such as QR code stickers, mm-wave antenna, multi-layer NFC antenna, and humanoid robot finger, among others. Also, J. Cai et al. reported the application of DLW to metalize nickel-based circuits for integrated wireless devices by combining an NFC tag for harvesting signals and a commercial IC chip for data storage.[204] The carbon/Ni composite coil presented a resonant frequency of ≈101.2 MHz, however the resonant frequency shifted to ≈19.1 MHz after connecting the IC chip. Additionally, the coil nickel structure was also used to wirelessly charge a microsupercapacitor, showing comparable performance with a commercial copper-wire coil. In 2019, J. Zhang et al. studied a facile strategy for selective fabrication of precise metalized patterns onto polymer substrates through DLW technology using organo-copper compounds as sensitizers.[89] An NFC tag was fabricated, which was combined with a commercial IC chip. Efficient information communication between the NFC tag and the smartphone was implemented via smartphone. Recently S. Feng et al. reported an interesting approach using DLW patterning on zinc and iron microparticle inks to reach biodegradable conductors.[69] The laser sintering was quite effective in converting naturally oxidized microparticles into interconnected Zn conductors on flexible biodegradable substrates. These conductive features present an excellent conductivity of up to $\approx 2 \times 10^6$ S m$^{-1}$, mechanical flexibility, and fine feature resolution of ≈45 µm. To demonstrate the viability of this methodology, an NFC tag with miniaturized dimensions to fit on the fingernail was fabricated, as shown in Figure 19j. By easily varying the size of the sintered zinc NFC tag, different return loss signals could be obtained (Figure 19k), allowing for communication with a smartphone NFC reader. After utilization, the simple application of water easily disintegrates the NFC tag on the biodegradable substrates, showing potential for short-lifetime wearables, edible electronics, and implantable medical devices.

Besides metallic patterns processed by DLW, the fabrication of carbon-based planar antenna tags has also been pursued. In 2020, Abdul-Aziz et al. fabricated LIG-based coplanar waveguide-fed monopole antennas on glass substrates, as well as the same configuration but with $MoS_2$ TMDC modifying the carbon material.[367] The main finding was the enhancement of antenna gain by 30% when compared to a reference copper antenna. Furthermore, the authors compared LIG and LIG/$MoS_2$ heterostructure antennas with printed graphene-based antennas, showing comparable operating bandwidth (8 GHz) and gain. Rivadeneyra et al. fabricated antennas matching commercial designs in ultra-high frequency (UHF) radio frequency identification (RFID) band.[368] Graphitization of PI was compared with laser reduction and patterning of GO, achieving the expected resonance peak in the UHF band, according to simulations, but with a lower magnitude than reference copper antennas. This showed the potential for manufacturing cost-effective and eco-friendly UHF RFID tag antennas by DLW graphitization methods. Since then, several reports have expanded the exploration of LIG-based tag antenna designs for several purposes,[369,370] including for wireless sensing applications.[371] To note the work by Chietera et al.,[369] where a comparison was drawn between different fabrication methods, including fused filament 3D printing, aerosol jet printing, and laser graphitization. The same RFID tag design was fabricated, resulting in tag architectures with different conductive material and substrates. This results in different resistive behavior of conductive parts, ultimately resulting in substantial performance differences. However, the authors highlight the potential of LIG for sustainable RFID system fabrication with further research. Other precursor materials, such as cellulose substrates, have also been recently employed for LIG-based microchip patch antenna fabrication.[372]

### 5.2. Circuit Interconnects

Circuit interconnects are key when integrating several electronic components, either at BEOL processes for IC fabrication, as well as connecting ICs and other components, within a printed circuit board (PCB) design. In this regard, DLW has provided increased degrees of freedom for the seamless integration of these components, by allowing for the writing of several highly conductive materials, appropriate for low-power electronics integration, in several platforms, from rigid carriers to flexible substrates. In this regard, DLW processing of metal tracks has been the main approach, targeting useful metallic conductors such as copper,[75,137,169,196,199,246] silver,[35,42,101,118,163,336] platinum,[42] and liquid metals.[194,207,373] Has detailed in previous sections, attainable resolutions using these materials depend on several factors, including precursor formulations (e.g. NP, metal ion inks, or LISM), laser system, and underlying photochemical or photothermal mechanism for writing. This ultimately determines the compatibility of the writing process with BEOL processes or solely as PCB connectors. Nevertheless, several unique features have been developed for electrical interconnects fabricated through DLW. In the work by Kwon et al., the authors demonstrated the capability to pattern silver interconnects across the boundary edge of glass substrates (Figure 19l), capable of connecting both surfaces, with the intent to develop lean, space-efficient electronics.[101] By employing a laser sintering approach of AgNP coatings, the authors were able to establish interconnects through the side wall and chamfered edges of the glass, by optimizing laser parameters such as the laser spot aspect ratio, writing speed and wavelength (CW IR laser vs visible laser). The resulting sintered silver interconnects revealed a very good adhesion and mechanical resistance, effectively able to connect an LED array to a lithium battery fixed to the opposite surface, in a bezel and bonding-free approach (Figure 19l). Another capability of DLW for electrical interconnect establishment has been for flexible and stretchable circuits. The use of inherently stretchable conductors, such as liquid metals, has been a possibility, either through sintering approaches[373] or LISM.[194,207] To highlight the work of Hu et al., where the authors present an ultra-stretchable liquid metal circuit by laser activation of an elastomer substrate, designed to receive Galistan liquid metal alloy.[207] The fabricated circuit can

be stretched to 1000% strain, being ideal for several on-body applications in body parts with high stretching motion characteristics. Recently, another approach was presented for stretchable, multilayer circuit fabrication, based on simultaneous sintering of Ag flakes and PDMS curing.[35] In this work by Song et al., an IR nanosecond laser is used to develop the Ag/PDMS conductive tracks for each circuit layer, while a visible femtosecond laser is employed to fabricate via holes after circuit passivation, without damage to the conductive material beneath (Figure 19m). With this approach, the authors demonstrated the seamless, vertical assembly of a stretchable, passive LED array, that can withstand 1000 stretching cycles at 30% strain (Figure 19n). DLW also provides the capability to adapt circuit interconnects by writing, erasing, and rewriting cycles of several materials.[169,336,374] This has been mainly achieved by using a laser beam capable of erasing pre-written patterns or by changing irradiation parameters into ablative regimens. In the work by Zhou et al., the change of beam focus of an 808 nm CW diode laser shows the capability to erase and rewrite copper patterns from a copper nitrate/NMP/EG precursor, with the authors demonstrating the capability to adjust circuit interconnects to assemble LEDs in series and parallel.[169] Another recent work by Kim et al. demonstrated the same capability but using AgNP sintering for writing conductive material.[336] For the erasing step, UV laser ablation is performed, allowing in situ adjustment of circuit elements depending on the desired features and functionalities of the electronic system.

### 5.3. Energy Harvesting and Storage

#### *5.3.1. Triboelectric Nanogenerators*

The development of the IoT is accompanied by the increase in the number of electronic devices, such as wearable sensors, which increases the need for miniaturized, alternative energy sources.[253,272,302] To meet this need, triboelectric nanogenerators (TENGs) have been widely explored to harvest and convert mechanical energy into electrical signals and power electronics,[38,221] since mechanical is the most ubiquitous form of energy.[38] TENGs can operate in different configurations, but the most reported are contact separation and single-electrode mode.[272] Their working principle is based on the coupling of electrostatic induction and contact electrification.[38,253] In the contact separation mode, when two materials are pressed together, the material's surface with a higher ability to capture electrons (tribe-negative material) becomes negatively charged, whereas the other material will lose electrons and consequently acquire a positive charge (tribe-positive material) at the interface due to migration of charges between the surfaces.[221,253,302] When the external force is withdrawn, the materials separate, creating a potential difference within the gap, which will be nulled by a current generated in the external circuit. Repetition of mechanical stimuli leads to the sequential generation of electrical signals.[221,253,302] Electrostatic induction is thus the phenomenon behind the generation of current in the external circuit.[272] The attractiveness of TENGs resides in their simple layered configuration[302] and straightforward and cost-effective assembly processes.[38,253] Layer-by-layer stacking of high conductivity electrodes is desirable and has been performed by vacuum deposition techniques of metals, although the cost associated with these techniques only making such devices viable for high-end devices and performance.[38,272] Thus, flexible TENG assemblies have been explored by several alternative conventional techniques, including printing and coating techniques and 3D printing methods.[375,376] However, challenges associated with electrode-substrate adhesion and interfacial contact can arise, when pairing conductive electrode layers and triboelectric materials, that must withstand long-term mechanical stress.[272,376] DLW can benefit the construction of such devices, due to the easy customization of electrodes made from different highly conductive materials of interest, directly interfacing and adhering both positive and negative triboelectric surfaces. Simultaneously with TENG electrode material writing, inherent microstructuration resulting from DLW can also benefit the performance of TENGs in several cases, for improved output power.[253,338,377]

In this scope, metal electrodes have conventionally been employed as the working electrode in TENGs. Zhu et al. reported the fabrication of copper electrodes made from reductive sintering of a CuO ink, employed in a contact-separation mode device, using Nylon and PVDF-TrFe as positive and negative triboelectric materials, respectively (**Figure 20a**).[38] The TENGs were capable of efficiently harvesting low-frequency mechanical energy, reaching open-circuit voltages up to 200 V (Figure 20b), short-circuit currents of 27.4 μA and powers of 3 W $m^{-2}$, capable of powering different portable electronic devices. Furthermore, the TENGs were also coupled with electroluminescent (EL) devices, to self-power an EL emission layer, lighting up and displaying customizable information (Figure 20c). According to the authors, the high performance of the triboelectric assembly allowed for a very low operating frequency of mechanical stimulus of 0.3 Hz, improving on reported low-frequency TENGs. Besides metal electrodes, DLW has enabled an easy implementation of other electrode materials, promoting a shift from metal to efficient carbon electrodes. Several source materials have been used for this purpose, including PI,[272] cork,[272] paper,[338] and even carbonized MXene/MOFs mixtures to modify nylon fabrics and design non-contact mode TENGs.[377] TENGs based on LIG/PDMS composites with 0.33 $Wm^{-2}$ power density were incorporated into flip-flops and able to charge a capacitor at a rate of $2.4 \times 10^{-2}$ mJ $s^{-1}$ when contacted with the skin at a frequency of 2 Hz. Moreover, during a 1 km walk, the generated open-circuit voltage was ≈760 V, and 0.22 mJ of electrical energy was stored on a capacitor.[272] With a focus on the sustainability of the final device, TENGs based on LIG and carboxymethyl chitosan were developed, where the polymer was used as positive triboelectric material.[221] The devices exhibited a maximum peak power density of 2.48 mW $m^{-2}$, and when tested under increasing frequency (0.042–0.833 Hz), their output signal increased from 9.61 to 55.67 V. TENGs have also been explored for on-site power generation. The authors also related the porous morphology of chitosan-derived LIG with the output performance of TENGs, which is more favorable when long-fibrous microstructures are formed.

In this scope, Funayama et al.[302] developed a device based on LIG produced from lignin/poly(lactic acid) sheets, which generated a voltage of 1.5 V when a water droplet flowed on its surface. Additionally, contact with a plant leaf generated an output signal of about 1 V. These tests demonstrate the applicability of

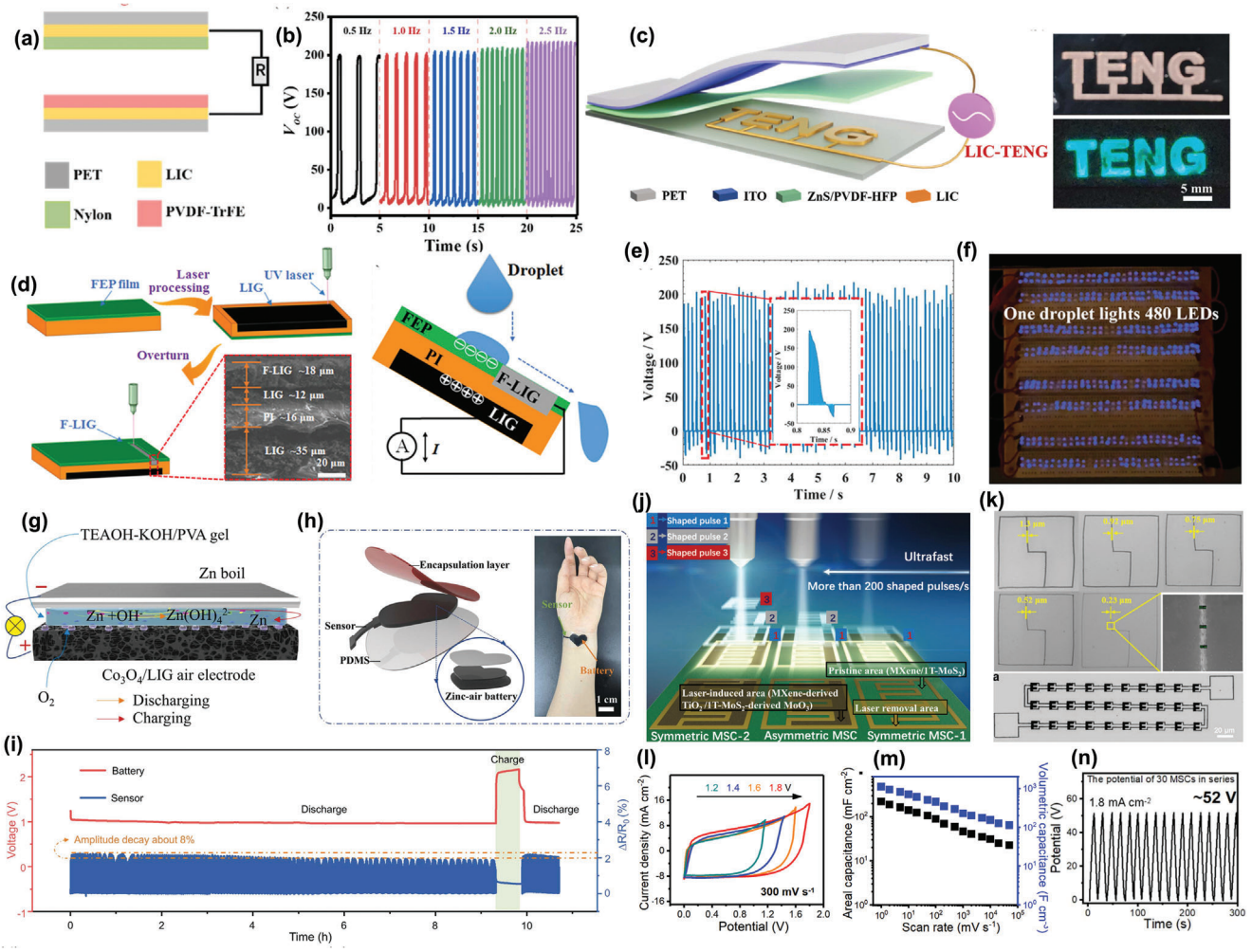


**Figure 20.** DLW microfabrication of energy harvesting and storage components. a) Copper-based TENG by reductive sintering of CuOx NPs ink, with Nylon and PVDF-TrFE positive and electric triboelectric materials, respectively. b) Open-circuit voltage output of TENGs at different contact frequencies. c) Connection of copper-based TENG to power EL layers and displays. Reproduced with permission.[38] Copyright 2022, Elsevier B.V. d) Fabrication of LIG-based double-sided TENG with fluorine-doped LIG surface, applied for DEG harvesting. e) Output voltage TENGs in response to dropping water droplets. f) Powering of 480 LEDs by DEG. Reproduced with permission.[378] Copyright 2021, Wiley-VCH. g) $Co_3O_4$/LIG air electrode for zinc–air battery system. h) Integration of zinc–air battery with strain sensors for a stand-alone sensing system placed on the wrist. i) Discharge voltage profile and strain sensor response of the integrated battery/strain sensor system. Reproduced with permission.[322] Copyright 2022, Elsevier B.V. j) Fabrication of multitype MSCs by beam shaping and irradiation of MXene/1T-$MoS_2$ thin film. k) Tailoring of MSC micrometer features and assembly capabilities. l) Cyclic voltammetry charge–discharge curves of asymmetrical MSCs. m) Areal and volumetric capacitance of asymmetrical MSCs for different scan rates (n) Galvanostatic charge-discharge curves of 30 MSCs assembled in series. Reproduced with permission.[335] Copyright 2023, Springer Nature.

TENGs processed by DLW for power generation in natural environments, helping decrease the reliance on common power sources. Similar high-performance energy harvesting methods can be employed, such as droplet-based electricity generators (DEG). Chen et al. developed DEGs capable of detecting the fall and sliding of water droplets, by producing LIG on both surfaces of PI, with one side being doped with fluorine (Figure 20d).[378] During the impact of 105 μL droplets, peak output voltages of 198 V (Figure 20e) and currents of 268.9 μA were achieved, with power varying with the external circuit load. The authors report a very high energy conversion efficiency of 2.29% resulting from the kinetic energy of water droplets, with the device showing a capability of lighting up 480 LEDs (Figure 20f) at a power density of 47.5 W m$^{-2}$. Regarding the morphology of TENG's layers, a study was conducted regarding the influence of surface roughness on device performance. Crumpled 2D $MoS_2$ layers exhibited higher work functions than flat layers, leading to improved performance.[253] As such, the performance of a TENG can be enhanced by tuning the work function of at least one of the triboelectric layers since it influences the electron transfer processes for the equalization of the Fermi levels upon contact. It is worth mentioning that the improved performance of crumpled layers was ascribed not only to electronic properties but also to its topology since it enhances contact electrification due to the improved surface contact area (friction and shear friction occur when in contact). The developed TENGs exhibited good performance ($V_{oc}$ of 25 V, $P_{max}$ of 2.25 μW, area equal to 10 × 10 mm$^2$) and were used to produce a touch sensor with multi-touch and

position-mapping capabilities.[253] Other studies also reported enhancing roughness to improve performance.[38,272] Besides roughness tailoring, multilayered TENGs have also been fabricated to increase their output power,[272] and pairing materials with opposing positions in the triboelectric series has also been pointed as an essential feature to produce high-efficiency devices.[272] Addressing devices with superior performance, TENGs based on molybdenum carbide/LIG composites exhibited remarkably high open circuit voltage (150 V) and short circuit current of 11 μA.[257] The devices' architecture comprised a polytetrafluoroethylene film sandwiched between molybdenum carbide/LIG electrodes. Salauddin et al. demonstrated the use of carbonized MXene/Zif-64 nanocomposites to build the intermediate layer of a fabric-based TENG. Outstanding power density of 65 $W.m^{-2}$ and peak voltage of 1.34 kV with a small dimension of 4 $cm^2$ were achieved, surpassing previous works. So far, the studies performed with TENGs fabricated with DLW approaches demonstrate their versatility and high efficiency, strengthening their implementation as portable energy harvesting alternatives in multifunctional platforms and wearable devices.

#### 5.3.2. Batteries

Batteries, especially lithium-ion batteries (LIB), are undoubtedly the power source for modern portable electronics. However, due to their rigid and bulky configurations, conventional batteries cannot be easily implemented in flexible technologies within the IoT. Additionally, lithium costs and electrolyte toxicity further hamper the application of LIB in flexible technologies.[322,379–383] Thus, thin film electrode battery cells have become increasingly desirable within this context, and laser processing has been employed over the years in several tasks, from electrode cutting, annealing, or structuring.[384] Alongside electrode processing by lasers, printing technologies have also been increasingly explored in thin battery concepts, for current collectors, electrolyte, and separator printing, to avoid physical vapor deposition under vacuum of metal electrode material (e.g., aluminum and copper).[342] Printing and solution processing technologies also benefit efficient monolithic integration of battery components. In this setting, DLW material growth introduces new methods for anode and cathode electrode patterning, while promoting the exploration of new, versatile battery configurations.

As was shown through this review, LIG electrodes can be induced in a plethora of flexible substrates, which can act as a current collector. In this case, heavy metallic foils are not required, significantly reducing the weight of the battery.[250] In a very elegant way, Yadav et al. address this issue, by assembling a flexible zinc-ion battery (ZIB) based on DLW-engineered current collectors followed by electrodeposition of active materials.[379,382] The team laser-scribed interdigitated electrodes on PI followed by the electrodeposition of vanadium oxide and zinc. The obtained aqueous rechargeable ZIB exhibited a high initial capacity of 556 mAh $g^{-1}$ at a current density of 0.1 A $g^{-1}$, even after considerable mechanical deformation tests,[379] showing comparable performance with other cells reported in the literature using other synthesis and assemblies methods. The cell exhibited a remarkable 0.0067% capacity loss per cycle over 5500 cycles at 2 A $g^{-1}$. Hu et al., fabricated a carbon-coated $Mo_2C$ nanofiber by spin-coating, which was successfully used as a LIB anode.[380] Notably, high current densities of 5 A $g^{-1}$ were reported, promoted by the carbon coating graphitization, showing improvements over other reported $Mo_2C$-based anode materials. Deng et al., irradiated a $Mn_7O_{13}{\cdot}5H_2O$/GO film, promoting oxygen vacancy defects on the $Mn_7O_{13}{\cdot}5H_2O$. The obtained composite was used as a ZIB binder-free cathode, achieving a relatively high specific capacity of 411.6 and 176.3 mAh $g^{-1}$ at current densities of 0.2 and 5 A $g^{-1}$, respectively. According to the authors, the larger number of active sites and oxygen defects over the metal oxide leads to higher capacity and longer cycle life, when compared with traditionally coated substrates. A 90.1% capacity retention was observed after 3500 cycles at 2 A $g^{-1}$.[381] The creation of oxygen vacancies on active materials is quite beneficial for battery applications and it is actively pursued by DLW.[381,385]

The examples shown so far describe the implementation of composite electrodes. However, DLW-synthesized graphene can also be implemented as both a current collector and active material. Graphite anodes are conventionally used in LIBs, although they cannot provide high-power densities, mostly due to slow-ion diffusion through their structure. LIG foams proved to enhance electron mobility in the anode, leading to a high reversible areal capacity of ≈280 μA h $cm^{-2}$ (against lithium metal) at a current density of 0.1 mA $cm^{-1}$.[386] DLW processing of alternative materials sources has also been proposed for battery anode production. Laser-sintered aluminum NPs for Al–air batteries have been reported, with areal discharge capacities of 1.5, 2.8, and 3.23 mAh $cm^{-2}$, for 1, 2, and 3 printed electrode layers, respectively.[152] Laser-scribed $Mo_2CT_x$ MXene (LS- $Mo_2CT_x$) has also been employed as an anode in LIBs, with boosted redox kinetics from the presence of $Mo_2C$ nanodots and lower oxidation degradation potential, both resulting from the laser irradiation process.[77]

Seamless assembly and integration of batteries along standalone platforms containing other functional elements have also been described. One example was demonstrated by Chen et al.[322] where, $Co_3O_4$ NPs are synthesized by laser irradiation, to act as active materials of ZIB battery electrode. As this procedure is conducted over the PI substrate, the resulting particles are in good contact with the conductive carbon phase, effectively doping the LIG, resulting in a $Co_3O_4$/LIG air electrode (Figure 20g). Then a LIG strain sensor is also engraved, followed by interconnection lines connecting both battery and sensor on the same support substrate (PDMS) (Figure 20h). The system was used as a wristband for monitoring vital signals up to 9h and 20 min, with a small decay of the measured strain signal associated with battery discharge (Figure 20i).[322] These simple and effective integration approaches demonstrate the potential of DLW for battery-based IoT systems.[39,322] LIG can also be implemented as a battery electrode stabilizer. For instance, sodium has been regarded as a safer, cheaper, and more environmentally friendly material for post-lithium-batteries.[387] However, dendritic growth represents a serious hazard to this type of technology. As such, sodiophilic particles anchored on LIG can prevent sodium nucleation and dendritic growth. Additionally, LIG's highly porous structure facilitates ion transportation kinetics, boosting the battery cyclability.[388] Anode-free batteries can also benefit from laser-derived carbon. Graphene oxygen groups provide lithiophilic sites, which promote lithium nucleation at paces

4–5 times faster than what is commonly observed in copper.[129] Although DLW implementation in batteries at a research level is underway, there are some challenges, and continued research is needed for DLW to be an attractive technique beyond electrode material writing and electrode functionalization. These are related to the different solid constituents of rechargeable batteries, such as binders, requiring multimaterial processing for monolithic integration. Thus, DLW may be integrated with other conventional manufacturing technologies in hybrid systems, taking advantage of the versatile material writing and functionalization capabilities of DLW for improved battery performances.

#### 5.3.3. Microsupercapacitors

Microsupercapacitors (MSCs) have been identified as a top-performing electrochemical power source for IoT components and miniaturized electronic systems.[130,268,305,389] A typical MSC consists of two high-surface-area electrodes in an electrolyte solution separated by a thin polymeric membrane, which stops the system from short-circuiting. These devices can be designed in several ways, being the in-plane, flat interdigitated configuration one of the most popular. It not only reduces the ionic path but also improves the efficiency of active electrode materials and their charge collection capabilities. Additionally, these architectures are easily on-chip integrated.[389,390] Several strategies have been employed to optimize the performance and expand the range of applications for MSCs. Notably, high-surface area, conductive nanomaterials (such as graphene and MXenes) hold promise in augmenting both energy and power densities.[300,305] Simultaneously, the advancement of fabrication techniques, with high resolution, facilitates the diffusion of ions, thereby promoting device cycle stability and further enhancing overall capacitance.[390] In this perspective, DLW material growth techniques have been established as versatile, high-throughput alternatives for MSC electrodes/current collector fabrication,[389] alongside ink printing technologies.[343] Moreover, it not only allows patterning the desired device design but also the conversion of precursors into electrode active materials.[305,389–391] The simplest laser-based MSCs are fabricated by directly converting a substrate into a conductive, porous carbon form with enhanced surface areas.[117,268,273,291] Carbon-based electrodes are very popular as active materials due to their high conductivity and cycling stability. The first LIG MScs were fabricated by chance on PI, but since then a whole range of substrates have been explored.[72] LIG has also been implemented in the design of high-surface-area 3D MSC architectures, by a layer-by-layer growth of graphene structures with macro properties.[218,392] Song et al. followed such an approach by depositing and carbonizing layers of microporous PES.[218] The resulting 3D graphene macrostructure is highly porous, and conductive, and exhibits a good capacitive behavior, obtaining a maximum specific capacitance, $C_A$, of 153 mF cm$^{-2}$ at a current density of 0.5 mA cm$^{-2}$. Additionally, it keeps 95% of its initial capacitance after 10 000 cycles at 2 mA cm$^{-2}$. Despite being suitable for MSCs, carbon-based materials suffer from low energy densities. This problem is usually addressed by using pseudocapacitive materials which can store more energy than carbon structures, or developing asymmetric MSCs, where anodic and cathodic electrode properties are individually designed with different charge storage materials.[391,393] In the work by Lei et al., lignin-derived LIG electrodes were modified with a Prussian blue analog in the positive electrode and a titanium carbide Mxene pseudocapacitive material in the negative electrode. The performance metrics of this MSC design were significantly higher than other reports of Mxene-based MSCs fabricated by other techniques, such as vacuum filtration, laser cutting, and extrusion printing, with a maximum energy density of 70.5 μW cm$^{-2}$, power density of 52 mW cm$^{-2}$, and high areal capacitance of 198 mF cm$^{-2}$. Xu et al. utilized a $CO_2$ laser to convert a $MnCl_2$/PAA film into a $MnO_2$/LIG composite.[394] While the PAA is converted into LIG, $MnCl_2$ is oxidized to $MnO_2$. In this case, $MnO_2$, a pseudocapacitive material, is distributed in a conductive structure formed by LIG, resulting in a large energy density of 1.22 mWh cm$^{-2}$ at a power density of 1.278 mW cm$^{-2}$. This type of architecture is commonly used in the fabrication of high-performance MSCs, in a variety of substrates, taking advantage of the synergies between both materials.[393] Similarly, DLW can also be used to dope LIG with heteroatoms, such as nitrogen (N), boron (B), phosphorus (P), sulfur (S), and fluorine (F). Doping carbon with these heteroatoms changes carbon energy levels thus enhancing conductivity, charge-storage properties, and pseudocapacitance.[305,319,395,396]

So far, the importance of LIG for MSC development has been shown. However, DLW has gone beyond carbon-based MSCs. Xie et al. prepared metal current collectors made from copper/nickel based on a LISM protocol. As an active material, the authors electrodeposited polypirrole (PPy) conductive polymer. Using this assembly, the authors improved the energy and power densities of the MSCs, when compared to other devices made from PPy active materials. Integration of four MSCs in series with a copper coil for wireless charging was also demonstrated, aiming for miniaturized energy storage devices. Besides direct current collector patterning, DLW has been used for functionalization. Hwang et al., followed a LIHG process to prepare $MnO_2$ nanowires. In this case a focused CW Nd:YAG (532 nm) laser beam irradiated a $MnO_2$ NP-seeded Au substrate, leading to the fabrication of flat in-planes MSCs,[397] exhibiting a $C_A$ of 227 mF cm$^{-2}$ at a current density of 1 mA cm$^{-2}$. More interestingly, these structures also exhibit high energy densities of 30.9 μWh cm$^{-2}$ at a power density of 1112.2 μW cm$^{-2}$. Similar examples have been reported for the sintering of silver NPs and metal oxide electrodes,[398] LIHG of iron oxide NPs,[193] or titanium carbide heterostructures.[130] In a stride to greatly improve the resolution and high throughput capabilities of DLW processing within MSCs fabrication, Yuan et al. used a femtosecond laser for the fabrication of multitype micron-sized (10 × 10 μm$^2$) MSCs.[335] Briefly, films of MXene/1T-$MoS_2$ were deposited onto a glass substrate and a shaped light field was used to selectively ablate and convert the MXene irradiation surface (Figure 20j). Differently shaped fs pulses were modulated by a Michelson interferometer, while a spatial light modulator was used to spatially shape the pulse into the desired laser writing geometry. Using these temporally and spatially shaped femtosecond pulses, synthesis, and machining of material can be easily performed in one step. With this method, the conversion of MXene/1T-$MoS_2$ into MXene-derived $TiO_2$/1T-$MoS_2$-derived $MoO_3$ was demonstrated. This effect opens the possibility for fabricating symmetric MXene/1T-$MoS_2$, MXene-derived $TiO_2$/1T-$MoS_2$-derived $MoO_3$ (same material for both

electrodes), and asymmetric MXene/1T-$MoS_2$//MXene-derived $TiO_2$/1T-$MoS_2$-derived $MoO_3$ (Figure 20j). The method presented by the authors offers several advantages for device mass production, including the tailored microfabrication of different types of electrode materials, precise manipulation and patterning of micrometer-size devices and their features (e.g., narrow gap separation between electrodes, Figure 20k, promoting more efficient charge ion transfers) and easy integration of MSC in series and parallel configurations. Many of these advances are still challenging for more established techniques, requiring multi-step fabrication strategies.[283] Furthermore, the fabrication of 6000 symmetric MSCs (or 3000 asymmetric MSCs) per minute was demonstrated, enabling device production at a large industrial scale. Employing $H_2SO_4$ aqueous electrolyte, symmetrical and asymmetrical MSC configurations were characterized by their capacitance characteristics under different charge and discharge settings (Figure 20l). For asymmetrical MSCs, area and volumetric capacitances of 220 mF $cm^{-2}$ and 1101 mF $cm^{-3}$ were reported, respectively (Figure 20m). The integration of MSCs in series was also demonstrated, showing a considerably enhanced voltage window of 52 V when 30 MSCs are interconnected (Figure 20n). Thus, Mxenes embedded in MSC architectures processed by DLW have recently been a focus of research to improve their performance.[334] Due to its versatility, simplicity, and eco-friendliness, DLW is expected to greatly benefit the sustainable development of high-performance MSCs, by efficient current collector engineering with plenitude of capacitive and pseudocapative materials. However, similarly to batteries, large-scale industrial implementation of DLW for MSCs fabrication would need to be accompanied by other technologies, such as printing[343] beyond electrode fabrication, especially for rational electrolyte inclusion. However, DLW has shown to be an ideal technology to develop high-performance MSCs, with several instances achieving comparable or improved performances when compared to other processing approaches[399] and commercial devices.[391]

### 5.4. Heaters

Flexible heaters can act as portable heating sources that can be used in several areas, including healthcare,[69] defense, and aerospace.[149] Generating thermal energy by Joule heating is considered a viable function to be integrated into thermotherapy pads, sensors, or smart windows.[149] Regarding healthcare-related applications, the potential of incorporating flexible heaters in thermotherapy has already been explored.[69] Thermotherapy is an approach used to accelerate blood flow to relieve pain perception and joint stiffness. In this scope, Feng et al. developed a heater based on a zinc grid on top of a PVA substrate that reached 45 °C under an applied voltage of 4 V.[69] Several groups have explored the deffoging ability of flexible heaters. The temperature of a serpentine based on bimetallic Cu-Ag increased from 40 to 130 °C as the supplied voltage varied from 3 to 8 V. The Cu-Ag-based heater could dry water (2 µL) dropped on its surface within 60 s.[164] Another heater based on copper patterns could also dry droplets sprayed on its glass substrate in 30 seconds under a 4 V power supply.[203] Solar thermal heating has gathered much attention since photothermal-based devices can provide on-site heating by absorbing solar light and converting it to thermal energy. In this scope, a heater based on carbonized chitin nanopaper whose temperature reached 77.7 °C under a 1 sun irradiation was produced, proving the possibility of using sun irradiation as a source for heating.[80] A flexible electrothermal element based on aluminum nanoparticles and LIG proved to have superior performance to other devices produced by laser irradiation, as it presented a transformation coefficient of $8.9 \times 10^{-2}$ K $mW^{-1}$. This heater reached a temperature higher than 112 °C when a power of 600 mW was applied, making it an interesting component for flexible electronics applications. The strategies reported for simple and time-effective production of heaters by DLW pave the way for integrating these flexible devices in various areas such as healthcare.

### 5.5. Sensors

#### 5.5.1. Photodetectors

Photodetectors are foundational devices in optoelectronics, designed to detect and convert incident light of different wavelengths into measurable electrical signals, for subsequent processing. Conventionally, lithographic methods have been used to pattern photodetectors based on inorganic semiconductors, but there has been a push for solution processing capable of accessing wet chemistry of broad range organic and inorganic semiconductors.[400] DLW can be useful alongside solution processing, due to its capability for synthesizing or doping several semiconductor materials with customizable bandgaps, resulting in tunable sensitivity in response to radiation. Furthermore, its great versatility allows for the customization of device architecture, beyond layer architectures, in cases where such versatility is not accessible by other manufacturing technologies. Different geometries, from interdigitated electrodes[209] to directly patternable heterojunctions[36] have been idealized. Metallic copper and other oxidation states can be tuned interchangeably using DLW, to construct both these types of device architectures. Zhang and co-authors employed a LISM framework to pattern interdigitated copper electrodes, using a subsequent coating of nanostructured ZnO as the photosensitive layer. ZnO presents a wide bandgap responding to UV radiation, in this case with low rise and decay time below 1 second.[209] In a similar study, the same group used this approach to develop photodetectors in cement materials, aiming at smart building applications. In the presence of a UV light source, the photodetectors are capable of generating a current of 300 µA for an incident intensity of 1500 mW $cm^{-2}$, capable of lighting an LED as an alarm signal.[211] In the work by Bae et al.,[37] fully laser processed, wafer-scale metal oxide photodetectors arrays were fabricated, using laser oxidation of write ITO electrodes and ZnO photosensitive channel. The authors demonstrated the positive advantages of implementing laser processing for metal oxide-based nanosensor development, when compared to coating and printing techniques and deep UV photosynthesis, namely the faster processing, unneeded annealing, and large-scale fabrication. In terms of performance, the photodetectors presented a peak photocurrent of 2.9 µA when exposed to UV radiation (254 nm), comparable to the figure of merit reported in the literature.

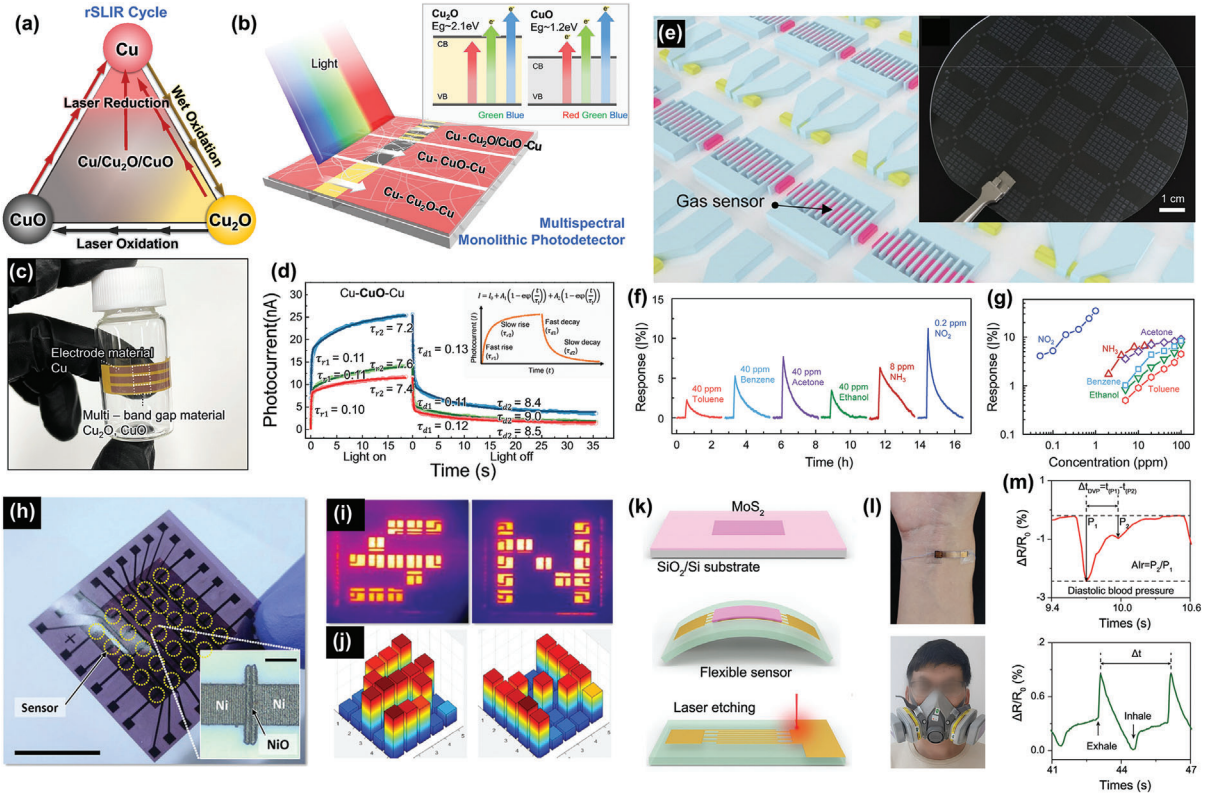


**Figure 21.** Sensor applications engineered by DLW. a) Process diagram of reversible laser-induced redox process for Cu and $CuO_x$ writing. b) Monolithic integration of multispectral photodetectors using different junctions. c) Flexible photodetector on a polyurethane acrylate substrate, composed of Cu electrodes and tunable multi-bandgap copper oxides detecting channel. Reprinted with permission.[36] Copyright 2022, Springer Nature. e) Conceptual illustration and optical image of wafer-scale gas and photodetector sensor arrays based on DLW fabricated ITO electrode and ZnO channels. f) Response of gas sensors to different volatiles. g) Comparison of linear response regimens of gas sensors to the same volatiles, portraying better sensitivity for $NO_2$ detection and quantification. Reproduced with permission.[37] Copyright 2022, Wiley-VCH. h) 5 × 5 thermistor array, based writing of Ni and NiOx through DLW monolithic reductive sintering. Thermographic image (i) and resulting thermistor temperature mapping (j) of the artificial thermoreceptor array. Reproduced with permission.[44] Copyright 2019, Wiley-VCH. k) Fabrication of flexible MoS2 film-based strain sensors. l) Implementation of MoS2 strain sensors in the wrist and in a face mask, to measure (m) pulse waveform and respiratory rate. Reproduced with permission.[252] Copyright 2021, Elsevier B.V.

Laser oxidation of copper films has been used to fabricate functional heterojunctions designed for photodetector implementation. In the report by Kwon et al., copper oxide compounds are patterned in different configurations directly on a copper film, to present specific location-dependent current response profiles, based on their specific photoconductivity.[187] CuO (bandgap of 1.3–2.1 eV) and $Cu_2O$ (bandgap 2.1–2.6 eV) can be patterned depending on the laser intensity, presenting a response to visible (532 nm) and near-infrared radiation (1064 nm). In a more recent study, the same group employed copper nanowires as the source copper material and demonstrated the capability to interchangeably oxidize and reduce the NW to specific copper oxide compounds.[36] This reversible selective laser-induced redox process (**Figure 21a**) operates by changing the reductive or oxidative capabilities of the irradiation process, by adding an ethylene glycol reducing agent, or direct laser oxidation employing a 532 nm wavelength laser. This allows for seamless interfacing of Cu, CuO, and $Cu_2O$, to develop flexible photodetectors with different sensitivities towards specific wavelengths in the visible spectrum (Figure 21b,c), namely their photocurrent and rise and decay constants (Figure 21d), showing the great potential of such devices for optoelectronic applications. Besides these approaches, DLW for semiconductor doping and bandgap tuning have been prolifically employed within photodetector microfabrication. Long et. Al deployed a ZnO and $SnO_2$ laser synthesis method based on sol–gel precursor formulations, leading to oxygen-vacancy-rich metal oxides, with good photocurrent generation potentials.[337] Another alternative has been the direct bandgap tuning of TMDCs within photodetector channel architectures, exemplary developed with molybdenum ditelluride ($MoTe_2$)[401] and tungsten diselenide ($WSe_2$).[402]

### 5.5.2. Gas Sensors

Similarly to photodetectors, the development of gas sensors using DLW techniques has benefited from the capability to pattern semiconductor materials with both n and p-type conductive behavior, giving selective responses to oxidizing or reducing gases. Generally, oxidizing gases increase resistance in n-type semiconductors, while reducing gases create the opposite response.[186] This way, DLW has been a suitable technique to selectively

synthesize semiconductor materials with selective response to specific gases, while also being capable of creating semiconductor mixtures and junctions that improve gas sensing responses, with much more straightforward fabrication approaches. Metal oxides engineered through DLW have been a beneficial resource for gas sensor development using DLW. Castonguay and co-authors have reported the fabrication of single metal-oxide (NiO and CuO), noble-metal doped metal oxide (Pt-doped $Fe_2O_3$), and mixed metal oxide (CuO/ZnO) patterns bridging pre-patterned gold electrodes, to fabricate gas sensors with tailored responses to volatiles such as ethanol, acetone, $NO_2$, $NH_3$, and $H_2S$.[186] Depending on the fabricated metal oxide, different resistance shifts are measured on the system, related to the nature of the measured gas, with the authors reporting significant comparative enhancements between single oxides versus doped or mixed oxides. Furthermore, low gas concentrations, down to 10 ppb for ethanol, can be measured using NiO. In another work by Bae et al., the full capability of DLW to pattern metal oxide-based devices was deployed, by writing of wafer-scale ZnO-based gas sensor interfaced with ITO electrodes[37] (Figure 21e). The developed nanosensors presented good responses for different gases, including toluene, benzene acetone, ethanol, and $NH_3$ (Figure 21f). However, the authors reported better sensitivity and selectivity of the nanosensors for $NO_2$ detection, down to 0.2 ppm (Figure 21g). In another work, Austin et al. selectively patterned molybdenum oxides ($MoO_2$ and $MoO_3$) and 2H-$MoS_2$ over an amorphous $MoS_2$ substrate by varying laser output, to develop planar gas sensing architectures, used for the sensing of $NH_3$.[256] Long et al. also developed a metal oxide-based gas sensor, using oxygen vacancy-rich ZnO and $SnO_2$.[337] These oxygen vacancies, promoted by the specific laser synthesis framework, reduce reaction thresholds between ZnO and $H_2S$ and between $SnO_2$ and $NO_2$, leading to improved response times and sensitivity comparatively with thermal annealing and other synthesis methods reported in the literature. Besides metal oxides, other semiconducting materials have been engineered by DLW for gas sensor development, including 2D TMDCs,[18] metal carbide/graphene interfaces,[216] and LIG.[39,283] To note the work by Wang et al. where Kevlar textile is used for LIG writing, allowing for the integration of a $NO_2$ gas sensor and a battery unit, for self-powered operation aiming at protective clothing.[39]

#### 5.5.3. Humidity and Temperature Sensors

Temperature sensing is employed in many areas since different information can be inferred based on temperature studies.[282] The architecture of temperature sensors, similarly to humidity sensors, comprises conductive electrodes on top of which the active layer is deposited. The latter detects external stimuli via changes in its properties.[279] Regarding applications of temperature sensors, Shin et al. developed a temperature sensor array composed of 5 × 5 sensors with nickel electrodes and a nickel oxide channel,[44] which was used to develop prototypes of artificial skin with the potential to replicate the human sense of touch (Figure 21h). The Ni/$NiO_x$ based-thermistor was operational between 25 and 70 °C, presenting a temperature coefficient of resistance (TCR) equal to 0.4% $°C^{-1}$ and a response time of less than 50 ms. Using the developed thermistor array, a network of densely distributed thermoreceptors was simulated, capable of mapping areal temperature profiles, aiming at functional e-skins (Figure 21i,j). An approach to produce in situ platinum film sensors with tunable geometry was proposed by Wang et al.[139] A resistive sensor and a thermocouple were produced on alumina substrates and exhibited an extended working range (30–920 °C) and a TCR and Seebeck coefficient of 2.46 × $10^{-3}$ $°C^{-1}$ and 9.7 μV $°C^{-1}$, respectively.[139] Among the temperature sensors produced by laser techniques reported in the literature, the devices with superior performance are those based on laser-induced porous carbon. The carbon-based structures produced on polyimide substrates were then transferred to starch film to produce the final sensor that exhibited an excellent sensitivity (1.08 $°C^{-1}$) for temperatures between 25 and 90 °C.[403] Humidity sensing is a critical feature in devices used in healthcare, wearables, food packaging, environmental monitoring,[175] and other industrial applications.[225,287] In particular, these sensors have an essential role in point-of-care diagnosis and non-contact human-machine interactions.[404] Hydrophilic materials such as cellulose[405] and chitosan[287] can be included in the architecture of humidity sensors to increase their sensitivity. In the scope of cellulose-based sensors, a device with a working range between 11 and 98% RH was developed using TEMPO-oxidized cellulose paper and LIG electrodes. The sensor presented a sensitivity of 1.19 × $10^5$, response and recovery times of 60 (RH 75%) and 90 s (RH 50%), and high versatility, and was used for monitoring plant transpiration, human-body sweating, and real-time nasal breathing. Human breathing and sweat evaporation monitoring was also performed using $Ga_2O_3$/liquid metal electrodes, with a working range between 30 and 95% RH and fast response (1.2 s).[404] The rapid and cost-effective techniques described in the literature enable the production of humidity and temperature sensors in a single step and on a sole substrate, thus allowing the creation of multifunctional platforms where different data can be monitored.

#### 5.5.4. Mechanical Sensors

As a core component of smart devices and systems, pressure and strain sensors have emerged at the forefront of innovation. These sensors convert mechanical stimuli into different electrical signals and can be classified as piezoresistive, capacitive, or piezoelectric according to their working mechanism.[406] With functionalities extending across health monitoring,[407] human-machine interfaces,[408,409] robotic systems,[410,411] and beyond, these versatile sensors provide accurate data on mechanical stress and pressure changes.[412] Several sensors based on LIG produced from different substrates such as PI,[403] Whatman Grade 1 paper,[284] spruce and beech veneers,[217] cork,[224] and textile polymeric yarns[413] have been reported, highlighting the adaptability of laser technology to diverse materials. Among these sensors, the one produced from Whatman Grade 1 modified with lignin that underwent a 3.3% strain engineering treatment was used to record the pulse wave and monitor physiological activities such as finger gestures, swallowing, and eye blinking. Moreover, this sensor exhibited gauge factor (GF) values of 201 and 91 for tension and compression values lower than 0.022% and a detection limit of 0.00088%, which, jointly with its extended working range

(0.00088 to 0.222%) and fast response (0.165 s and 0.631 s under strain and compression, respectively) pave the way for using similar devices in human–machine interaction applications.[284]

Sensors based on $MoS_2$ films have also been developed (Figure 21k,l).[41,252] Although these sensors present low GF values (95 and 51.2)[41,252] and limited working range (up to 1.67% strain), they provide high versatility as they can be used for several bio-related applications, including monitoring radial artery pressure, respiratory rate (Figure 21m), and speech recognition through recording of vocal cord vibration[252] or even for the development of a platform able to determine stress direction.[41] Additionally, resistive touch sensors based on platinum lines have been reported.[147] Sensors based on copper patterns were also developed and used for contact object contour mapping and contact position identification.[82] Silicon carbide-based devices stand out among strain sensors produced by laser techniques as they present superior performance. These strain sensors exhibited a gauge factor of $2.47 \times 10^5$ and a limit of detection equal to 0.05% during strain tests.[227] Regarding pressure sensors, superior performance can be achieved using graphitic carbon structures produced from laser irradiation of PDMS substrates.[293] The superior performance of these devices can be ascribed to the elasticity of the polymeric substrates and the improved conductivity of carbide layers. The versatility of pressure and strain sensors is one of the essential points behind the scientific community's growing interest in these devices. This versatility is reflected in the vast list of their applications, ranging from monitoring electrophysiological signals to determining the position of objects and contact points. DLW facilitates the incorporation of pressure and strain sensors into various circuits as it allows the synthesis of a wide variety of materials on various flexible substrates through a high-efficiency, scalable approach that enables precise control.[414]

### 5.6. Bioelectronics

#### *5.6.1. Electrochemical Sensors*

Because of the single-use and disposability requirements of many electrochemical biosensors, conventional techniques, such as metal electroplating or evaporation associated with lithographic techniques[415] have been progressively shifting to more accessible fabrication routes, alternative electrode materials, and greener substrates. DLW has been a great asset in the fabrication and prototyping of electrodes for electrochemical sensing tasks, mainly due to the possibility for form factor-free design and organization of electrodes in the same substrate or chip platform. This ultimately decreases the steps needed from design to fabrication and implementation of an electrochemical biosensor. In this scope, LIG has been fruitfully explored as an electrode material, presenting itself as fairly inert, while showing good charge transfer capabilities for redox, faradaic analytical detection processes.[232] Since the first reports, LIG derived from several precursor sources has been explored for three-electrode, integrated on-chip electrochemical sensor fabrication. PI has been the main aromatic polymer of choice,[416] but substrate choice has been extended to substrates such as lignin,[78,276] paper,[43,116,282] cork,[274] or chitosan.[288,289] Ultimately, precursor choice, allied with the irradiation scheme and electrode designs, dictates material and device performance, regarding the resulting charge transfer capabilities within specific biodetection schemes.[106] However, each specific substrate and its inherent properties may endow the resulting electrochemical biosensors with certain capabilities, related to mechanical flexibility, biocompatibility, and biodegradability. In this regard, the work by Bezinge et al.[43] employed paper substrates to integrate LIG-based electrochemical sensors within paper microfluidic devices, to automatize sample transport and uptake within the sensing electrodes. Using wax printing as the paper microfluidic channel patterning technique, the authors included the electrodes both within lateral (**Figure 22a**) and vertical (Figure 22b) flow injection devices, assembled with all the sample, buffer, and absorbent pads needed in these systems. For the lateral flow injection system, alkaline phosphatase was detected in low serum sample volumes of 5 and 500 µL of carrying buffer, with low limits of detection comparable with gold-standard benchtop analysis systems (Figure 22c). For the vertical flow device, the authors showed the capability to perform recombinase polymerase amplification paired with CRISPR/Cas12 signal generation in an automatized fashion, to detect the presence of HPV16 based on signal quenching mechanisms, at very low copy concentrations down to 1 copy $\mu L^{-1}$ (Figure 22d). This work demonstrates the capability of DLW and LIG to simplify biomolecular analysis through electrochemical devices. Another route explored through DLW has been the synthesis of LIG hybrid materials, that have been used in nonenzymatic sensing of small molecules of interest.[321] Concurrently, other materials and strategies have been employed for electrochemical sensor fabrication using DLW. Zhoe et al. reported the patterning of $Cu/Cu_2O$ electrodes from a copper nitrate/PVP precursor mixture, targeting the nonenzymatic detection of glucose, with a low limit of detection of 340 nM. Rodriguez et al.[259] employed the method of writing conductive AlC/graphene networks in PET for the development of three-electrode planar cells, showing their capability to track redox reactions. Wang et al.[173] integrated writing strategies to fabricate electrochemical sensors made of gold, by laser-induced reduction of $HAuCl_4$ over GO-modified paper substrates and subsequent electroless Au growth, envisioning R2R fabrication strategies based on this DLW setup. The authors demonstrated the capability of fabricated sensors for hydrogen peroxide detection in milk samples. Another type of bioelectronic device targeting electrochemical biosensing has been the organic electrochemical transistors (OECTs).[417,418] In this regard, recent developments have been made in LIG-based OECT fabrication for biochemical analysis, where LIG has been employed in planar patterning of source, drain, and gate electrodes, while conductive polymers such as PEDOT:PSS have been used as channel material.[417] Efficient detection of hydrogen peroxide and glucose has been implemented within these OECTs, by modification of the gate electrode with the necessary recognition elements, aiming at wearable sweat detection of these metabolites.[417]

#### *5.6.2. Wearable Bioelectronics*

The need for multifunctionality is a key factor in many bioelectronic applications, mostly the ones designed for deployment in in vivo scenarios. Devices such as e-skins, wearables for

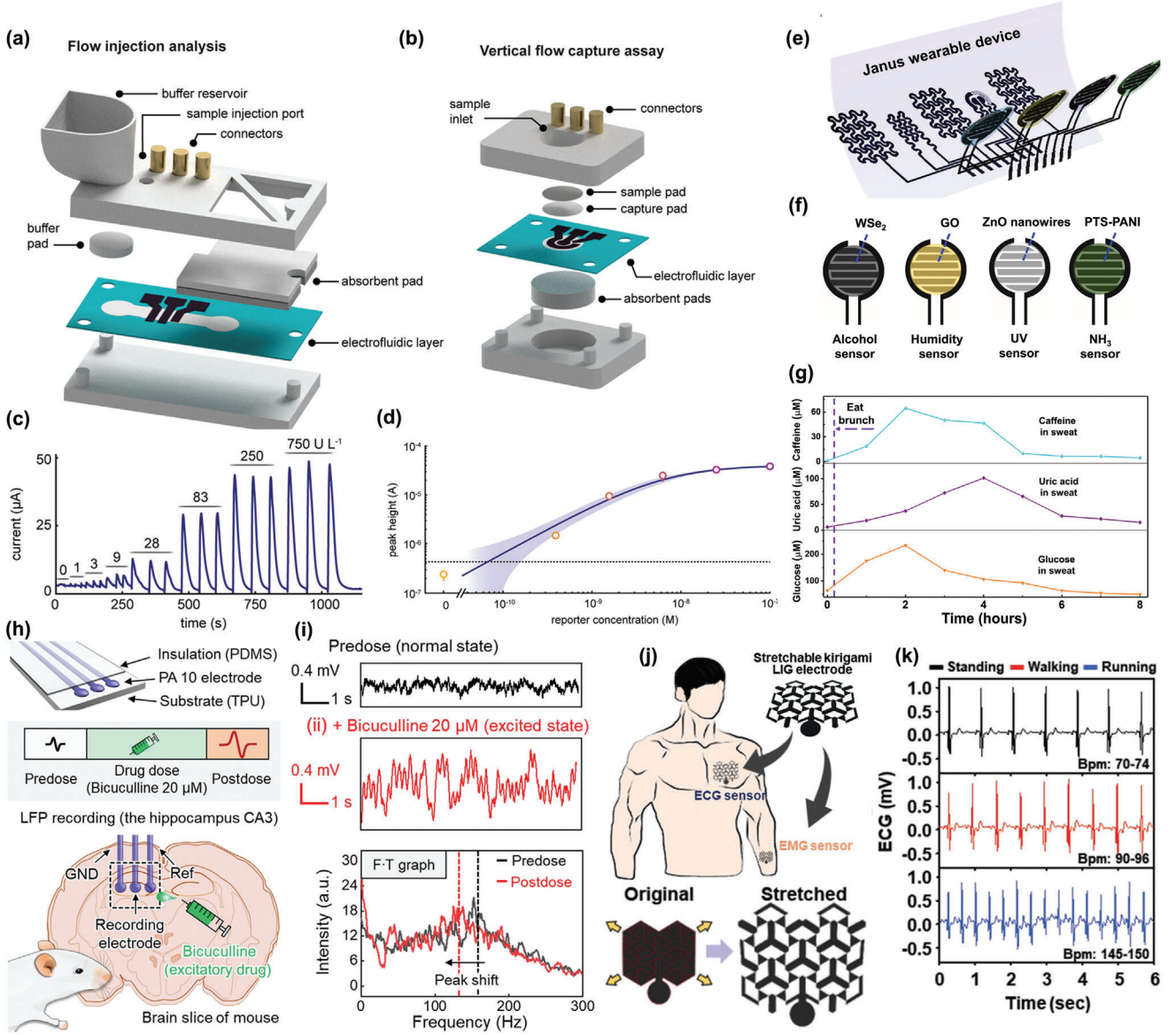


**Figure 22.** DLW fabrication of bioelectronics systems. Injection flow systems integrating paper-based electrochemical sensors with a) lateral and b) vertical flow. c) Alkaline phosphatase detection in spiked buffer samples. d) Response curve of CRISPR reporter for HPV16 detection. Reproduced with permission.[43] Copyright 2023, Wiley-VCH. e) Janus $MoO_2$ integrated wearable systems for the real-time monitoring of electrophysiological and biochemical signals. f) Sensing units for wearable electrochemical sensing. g) Continuous monitoring signals for caffeine, uric acid, and glucose detection in sweat using Janus $MoO_2$-based wearable system. Reproduced with permission.[70] Copyright 2022, American Association for the Advancement of Science. h) Neural recording device based on laser selective phase transformation of PEDOT:PSS and schematic in situ recording and neural stimulation of mice brain slice hippocampus. i) Local field potential signals of brain tissue and corresponding Fourier transform before and after stimulation with bicuculline. Reproduced with permission.[315] Copyright 2022, American Association for the Advancement of Science. j) Kirigami-inspired LIG electrodes produced from liquid crystal polymer and its stretching characteristics for biopotential measurements. k) ECG signals monitored for different activity states. Reproduced with permission.[71] Copyright 2023, Wiley-VHC.

human-machine interfacing, smart wound patches, or implantable electronics, require careful material selection, accommodating form factors, and several integrated functionalities, from sensing capabilities to energy management and connectivity.[419] DLW has greatly benefited the fabrication of such devices, due to the capability to fabricate functional components with straightforward, seamless interconnectivity, as presented in previous sections. A recent trend has been the use of laser processing for multimodal detection of different physiological information in integrated wearable devices. Yang and co-authors developed a wearable device that includes three functional components. An electrochemical sensing unit was integrated for biochemical monitoring of uric acid and tyrosine, while the remaining components were designed to detect biophysical signals, namely temperature and respiration rate.[420] The LIG-based electrochemical, temperature, and strain sensors

were all patterned in the same PI substrate, being interfaced with a laser-engraved microfluidic network, designed to sample and transport sweat for on-body biochemical sensing using this biofluid. Furthermore, the wearable sensing chip was connected to a flexible PCB, designed to analyze and transmit the retrieved physiological information. This was a breakthrough work, that showed the applicability of LIG-based, integrated bioelectronics for sweat metabolite detection, with full functionality for autonomous operation directly in the body. Since then, other LIG-based wearable devices for sweat biomarker analysis have been fabricated, including c-reactive protein,[421] cortisol,[422] essential amino acids and other metabolites,[423] and COVID-19 biomarkers.[424] A more relevant feature of some of these LIG wearable devices for wearable sweat electrochemical sensing is the inclusion of passive sweat induction, in the form of an integrated iontophoresis stimulation system.[421,423] The resulting wearables possess all the functional components for operation, from sample induction, collection, transportation, sensing, and analysis to data transmission, ready to be deployed in real-time analysis for diagnostic and health monitoring purposes. Since then, other DLW approaches aimed at developing wearable applications with several integrated functionalities have been presented. Zhao et al. developed $MoO_2$-based sensing components integrated into a wearable device on a porous SEBS membrane substrate (Figure 22e).[70] Electrode sensing components for alcohol, humidity, UV radiation, and $NH_3$ were patterned on one side of the substrate (Figure 22f), while temperature, electrophysiological, and sweat biochemical sensors (uric acid, glucose, and caffeine) were patterned on the opposite side of the substrate, in contact with the skin.[70] Interfacing with a FPCB allowed for the simultaneous and continuous measurement of these parameters, for daily-life activity monitoring over long periods (Figure 22g). Similarly, Sharifuzzaman et al. employed a carbonized MXene/fluoropolymer conductive material to pattern a hybrid bioelectronics textile over a breathable double-sided adhesive tape, aiming at multimodal physiological sensing.[317] Three components were fabricated, for electrochemical glucose and pH sensing and ECG biopotential detection, aiming for exercise monitoring. Real-time, on-body monitoring of sweat glucose was successfully implemented, with the calibration being adjusted by the measured pH values of sweat samples, while the ECG measuring system reliably captured changes in the frequency of ECG wave complexes associated with intense cycling. Other forms of wearable devices fabricated on textiles have also been reported, such as Kevlar[39,269] or commercial band-aids.[304] Recently, DLW has also been employed for the tailoring and management of wearable device functionality, by in-operando adaptation of component geometries and interconnection to control units. This was demonstrated by Kim et al., where the authors selectively laser-erased sensors using laser ablation and substitute them with other sensing and energy management elements, depending on the demand and use of the wearable device. With this approach, the authors could fabricate and connect temperature, UV, and humidity sensors interchangeably, as well as biopotential sensors and energy harvesters.

#### 5.6.3. Electrophysiological Sensing

Measurement of biopotential signals in biological systems and their stimulation are key when pursuing several functions for bioelectronic systems, such as human-machine interfaces, robotics, wearables, and implantable devices.[83,315] As such, flexible electrodes with good mechanical and electrical properties that can transport electrical stimulus are desired for applications such as the monitoring of electrophysiological signals or tissue stimulation.[83] Electrodes based on LIG, and conductive polymers have been explored for neuro-related applications, due to their good conductivity, low contact impedance, and overall biocompatibility.[71,315] Won et al. employed laser-induced phase separation processes, to improve conductivity and water-stability of PEDOT:PSS-based hydrogels and pattern neural recording and stimulation electrodes. Three electrode arrays were used to record neuronal signals on the hippocampus within a brane slice of mice, able to detect excited states of the local field potential signals of brain tissue after the delivery of an excitatory drug (bicuculline, 20 μM) (Figure 22h,i). Using low voltage, the same electrode array was used to stimulate the sciatic nerve, inducing significant leg motion.[315] Apart from neural stimulation, SiC electrodes produced by laser writing of PDMS were used to stimulate an ex vivo isolated heart that exhibited a slow atrioventricular node rhythm without stimulation, which synchronized with the stimulation frequency during the experiments. Additionally, a sheet of smooth muscle cells was stimulated using this SiC-based platform. After synchronization, enhanced contractility was detected, suggesting a possible therapeutic application of the developed composites in sphincter contraction or vasoconstriction.[260] Several LIG-based electrodes have also been used to record electrophysiological signals, using a myriad of substrates, from liquid crystal polymers,[71] Whatman Grade 1 paper,[220] and Kevlar textiles.[39] Notably, kirigami-inspired LIG electrodes were constructed from a liquid crystal aromatic polymer precursor, improving the operation of such electrodes under stretchable on-body applications (Figure 22j). The fabricated electrodes were used to monitor the EMG and ECG signals to distinguish physical activity intensities (Figure 22k).[71] The same precursor was used to fabricate LIG three electrode arrays for in-vivo recording of cortical potentials from the whisker somatosensory barrel cortex in mice, as well as allowing for motor cortex stimulation to induce hind limb movement.[71] Additionally, copper electrodes on PDMS substrates produced by LISM were used to record EMG signals to detect different finger gestures. The EMG signals were used to train a classifier, which then acted on a robot hand and allowed precise control over this tool. The results demonstrated the possibility of integrating the copper electrodes in human–machine interface applications.[83] Thus, recent developments of DLW have accessed time and cost-effective production of high-performance bioelectronic platforms for both wearable and in vivo, implantable bioelectronic applications, by engineering of low-impedance material writing on biocompatible, flexible substrate materials.

*5.6.4. Conclusions and Future Perspectives*

As presented in this review, DLW has found widespread applicability in the microfabrication of electrical and electronic components, needed for next-generation IoT technologies. This versatility arises mostly from the distinct stimulus provided by laser beams, either photochemical or photothermal, to perform ablative, additive, and transformative material processing tasks and construct functional elements and geometries. With the focus given in this review to additive and transformative laser-enabled material processing, DLW-based microfabrication presents itself as a straightforward, scalable production method with very high prototyping and iterative capabilities, poised for decreasing the time from laboratory to fabrication and final implementation. Laser material processing tools have become ubiquitous both in laboratories and in industrial processes, enabling a faster process-property optimization of both resulting laser-processed material properties and material integration and assembly, to reach next-generation consumable electronic and bioelectronic applications.

The very high material processability provided by laser-material interactions has enabled the synthesis and engineering of high-performance conductors, semiconductors, and insulator materials using DLW, virtually compatible with any rigid or flexible substrate material. This increases the cost-effectiveness of DLW when compared to other microfabrication technologies, since the same laser system may participate in very distinct manufacturing steps, providing end-to-end prototyping and fabrication capabilities for fully laser-processed applications. This is reflected in the recent progress in DLW-based microfabrication strategies gathered and reviewed here, which have progressively shown interest in researching lasers as reliable tools for material processing for electronics. Both comprehensive empirical and simulation studies have provided greater understanding and control over laser-material interactions and outcomes. The straightforward adjustability of laser stimulus, by manipulation of energy (e.g. beam energy, power), time/frequency (PRF, PW), and spatial (e.g., spot size, writing speed) fabrication parameters, enables the tuning of writing resolution, material thickness, uniformity and suitability for specific functional roles. Furthermore, tunable laser-processed material composition and resulting conductive or semiconductive properties allow for selective writing of integrated geometries with distinct capabilities from a common precursor, further highlighting the effortless, seamless integration potential of ADLW and TDLW processes. These aspects of DLW provide broad capabilities for application in the fabrication of sub-micron lines and components, suitable for several processes. Although fully laser-processed ICs have yet to be explored by DLW microfabrication approaches, the synthesis, and engineering of metals and semiconductors may enable FEOL processes for individual component development, to complement uses such as laser photolithography or laser annealing,[425] in cases where cost reduction and straightforward fabrication is preferred to high-standard performance. In this specific case, integrating the capability of TP-DLW processes for the high-resolution synthesis and printing of metal conductors and different types of semiconductor materials, from more accessible liquid precursor forms, is beginning to be a reliable tool for microscale fabrication, monolithic integration and seamless assembly of electronic components, towards laser fabricated microelectronics. More specifically, TPA for the synthesis of semiconductor materials, such as metal oxides or TMDCs, has been underreported, when compared to the synthesis and laser writing of metals, and has relied mostly on SPA and photothermal synthesis. Furthermore, because of the broad applicability of TP-DLW for microscale fabrication of 3D printed microstructures by photopolymerization, the fabrication of functional 3D micro components where structural materials and active conductive and semiconductive electronic components can be fabricated by the same laser tools. This may be achieved by exploring composite photoresists where different laser stimulus leads to the writing of dissimilar materials,[426] or sequential laser printing with different precursors.[42] Even though great advances on the fundamental principles and possible applications of TPA and TPR, continuous efforts will further promote the range of applications and future large-scale implementation of these processes for electronics microfabrication. BEOL processes may also be performed by DLW strategies for writing highly conductive metal lines. This is boosted by the appropriate selection of the laser system, its wavelength, and its suitability to meet the specific requirements of the target application. However, future studies could benefit these fabrication processes targeted by DLW, namely on the influence of laser irradiation on possible parasitic photon or thermal-induced effects on adjacent or subjacent materials, that must not be influenced by a DLW synthesis or conversion process.

Outside of wafer-scale microfabrication, large-area microfabrication of other functional elements, from electrodes, current collectors, semiconducting sensing channels, etc., has also benefited from the deployment of DLW, especially in the fields of energy harvesting and storage, sensors, and bioelectronics. Specifically, the capability to write multi-material electrode geometries with tailored properties and functionalities has been the most explored feature of DLW schemes. However, in this case, DLW still suffers from an important disadvantage when compared to other solution processing and printing technologies, related to the lower throughput, associated with some setups for material writing. For several printing processes, such as screen, flexographic, and gravure printing, S2S and R2R implementation for high-density fabrication of electronic components can be pursued, after full optimization of printed material properties. In contrast, DLW suffers from the characteristic line-by-line patterning associated with beam-directing systems, instead of the planar modality of printing technologies. Aiming at improving the fabrication throughput of optics and stage motion systems, the integration of multi-axis and multiple lasers for synchronized and simultaneous patterning could be explored to improve throughput and compatibility with S2S and R2R processes for large-area fabrication. Furthermore, as previously pointed out, optimizing DLW tasks for high scanning speed regimens, as well as the implementation of high-speed scanning systems can drastically improve the fabrication throughput of DLW. With further development of DLW microfabrication paradigms, a synergy between the continuous study of laser-material interactions and the development of laser systems would be beneficial for future industrial implementation, because most commercial laser systems are not specifically designed for material synthesis and conversion tasks. Thus, greater fine-tuning of applied laser stimulus with specialized lasers would decrease variability in material properties and

 

a greater overall reproducibility of DLW processes. In addition, most studies of DLW material growth focus on manipulating precursors for available lasers that researchers have access to, and not on designing laser tools with compatible properties for maximized irradiation outputs. Some recent instances in the literature have appeared, where tailoring the laser system hardware clearly benefits the laser synthesis processes and final device performance.[335] Thus, the final implementation of fully functional hardware for DLW setups would need to include appropriate laser sources, optics, and beam directing systems, while benefiting the nature of the irradiated precursor. For solution processing of precursors, the inclusion of laser hardware along solution dispensing units for coating or printing would greatly benefit future large-scale, high-throughput manufacturing, to perform pre- and post-processing stages in an integrated manner. For solid substrates, lasers could be included within extrusion instruments, for synchronous assembly of parts and laser writing of electronics. These hybrid additive manufacturing systems, with possible multi-beam wavelength, polarization implementation, will upgrade the range of sectors in which DLW could be present as a multifaceted manufacturing technology, to produce embedded electronics in several industries, including industrial manufacturing, medical devices and aerospace.[427]

DLW microfabrication and its additive and transformative modalities are becoming adaptable, multifaceted, and auspicious tools for the manufacturing of next-generation, flexible electronics for the IoT. By itself, or complementing other fabrication techniques within hybrid frameworks, alongside solution processing and printed electronics, future developments of DLW technology have the potential to impact electronics microfabrication. With the scope of different implementation levels, from material engineering, functional patterning, and system-level integration enabled by DLW, we anticipate future interest in research and industrial application, strengthened by the overview provided to readers in this review.

## Acknowledgements

This work was partially financed by FEDER funds through the COMPETE 2020 Programme and National funds from FCT – Fundação para a Ciência e a Tecnologia, I.P., in the scope of projects LA/P/0037/2020, UIDP/50025/2020 and UIDB/50025/2020 of the Associate Laboratory Institute of Nanostructures, Nanomodelling and Nanofabrication – i3N and project LIGHEART 2022.08597.PTDC. This work was also partially supported by the European Union's Horizon 2020 Research and Innovation Programme under Grant Agreement number 952169 (SYNERGY, H2020-WIDESPREAD-2020-5, CSA), 101008701 (EMERGE, H2020-INFRAIA-2020-1) and 101096021 (SUPERIOT, HORIZON-JU-SNS-2022-STREAM-B-01-03). T.P., M.M., and S.S also acknowledge funding from FCT – Fundação para a Ciência e a Tecnologia, through PhD grants 2020.08606.BD, 2022.13806.BD and SFRH/BD/149751/2019. J.C. and E.C. would also like to acknowledge funding from the National Foundation for Science and Technology through the project GAMBIT (2022.01493.PTDC). J.C. also acknowledges the funding from FCT – Fundação para a Ciência e a Tecnologia through the Individual CEEC contract (CEECIND/00880/2018) and thanks the EMERGIA Junta de Andalucia program (EMC21_00174).

## Conflict of Interest

The authors declare no conflict of interest.

## Keywords

bioelectronics, Direct laser writing, electronics, laser-material processing, lasers, material synthesis

Received: February 6, 2024
Revised: March 18, 2024
Published online: April 24, 2024

[1] J. Hecht, *Appl. Opt.* **2010**, *49*, F99.
[2] H. Jelínková, J. Šulc, in *Lasers Med. Appl.*, Elsevier, Cham **2013**, pp. 17–46.
[3] S. Affan Ahmed, M. Mohsin, S. M. Zubair Ali, *Def. Technol.* **2021**, *17*, 583.
[4] Y. Zhan, Y. Mei, L. Zheng, *J. Mater. Chem. C* **2014**, *2*, 1220.
[5] D. H. Kim, J. Xiao, J. Song, Y. Huang, J. A. Rogers, *Adv. Mater.* **2010**, *22*, 2108.
[6] L. Yin, J. Lv, J. Wang, *Adv. Mater. Technol.* **2020**, *5*, 2000694.
[7] M. Eslamian, *Nano-Micro Lett.* **2017**, *9*, 1.
[8] J. W. Park, B. H. Kang, H. J. Kim, *Adv. Funct. Mater.* **2020**, *30*, 1904632.
[9] E. Carlos, R. Branquinho, R. Martins, A. Kiazadeh, E. Fortunato, *Adv. Mater.* **2021**, *33*, 2004328.
[10] Y. Zhang, S. W. Ng, X. Lu, Z. Zheng, *Chem. Rev.* **2020**, *120*, 2049.
[11] Y. Pang, Y. Cao, Y. Chu, M. Liu, K. Snyder, D. MacKenzie, C. Cao, *Adv. Funct. Mater.* **2020**, *30*, 1906244.
[12] A. Zhakeyev, P. Wang, L. Zhang, W. Shu, H. Wang, J. Xuan, *Adv. Sci.* **2017**, *4*, 1700187.
[13] A. H. Espera, J. R. C. Dizon, Q. Chen, R. C. Advincula, *Prog. Addit. Manuf.* **2019**, *4*, 245.
[14] C. S. Buga, J. C. Viana, *Flex. Print. Electron.* **2022**, *7*, 043001.
[15] N. Divakaran, J. P. Das, A. Kumar P V, S. Mohanty, A. Ramadoss, S. K. Nayak, *J. Manuf. Syst.* **2022**, *62*, 477.
[16] Y. Khan, A. Thielens, S. Muin, J. Ting, C. Baumbauer, A. C. Arias, *Adv. Mater.* **2020**, *32*, 1905279.
[17] E. Yarali, C. Koutsiaki, H. Faber, K. Tetzner, E. Yengel, P. Patsalas, N. Kalfagiannis, D. C. Koutsogeorgis, T. D. Anthopoulos, *Adv. Funct. Mater.* **2020**, *30*, 1906022.
[18] Y. Xu, B. Jiao, Y. Wang, S. Xue, H. Gao, K. Yu, X. Fan, Y. Liu, Y. Tao, L. Deng, W. Xiong, *ACS Appl. Mater. Interfaces* **2022**, *14*, 5558.
[19] X. Tan, S. Wang, Q. Zhang, J. He, S. Chen, Y. Qu, Z. Liu, Y. Tang, X. Liu, C. Wang, Q. Wang, Q. Liu, *Nanoscale* **2023**, *15*, 9297.
[20] M. Carlotti, V. Mattoli, *Small* **2019**, *15*, 1902687.
[21] J. Chung, S. Ko, N. R. Bieri, C. P. Grigoropoulos, D. Poulikakos, in *American Society of Mechanical Engineeres Heat Transfer Division*, American Society Of Mechanical Engineers Digital Collection, New York **2003**, pp. 131–140.
[22] C. Zhu, X. Zhao, X. Wang, J. Chen, P. Yu, S. Liu, J. Zhou, Q. Fu, Q. Zeng, Y. He, J. H. Edgar, S. J. Pennycook, F. Liu, Z. Liu, *Adv. Funct. Mater.* **2021**, *31*, 2009549.
[23] J. Bian, L. Zhou, X. Wan, C. Zhu, B. Yang, Y. A. Huang, *Adv. Electron. Mater.* **2019**, *5*, 1800900.
[24] M. Kim, S. Osone, T. Kim, H. Higashi, T. Seto, *KONA Powder Part. J.* **2017**, *2017*, 80.
[25] A. Kumar, A. Kumar, A. Kumar, *Laser-Based Technologies for Sustainable Manufacturing*, CRC Press, Boca Raton, FL **2023**.
[26] Z. Chen, J. Yang, H. Liu, Y. Zhao, R. Pan, *Int. J. Adv. Manuf. Technol.* **2022**, *119*, 6919.
[27] K.-R. Kim, J.-H. Cho, N.-Y. Lee, H.-J. Kim, S.-H. Cho, H.-J. Park, B. Choi, *J. Manuf. Syst.* **2016**, *38*, 107.
[28] A. Balena, M. Bianco, F. Pisanello, M. De Vittorio, *Adv. Funct. Mater.* **2023**, *33*, 2211773.

[29] Z. Ahmadi, P. Fathi-Hafshejani, E. Kayali, M. Beidaghi, M. Mahjouri-Samani, *Nanotechnology* **2020**, *32*, 055302.
[30] Y. Ge, B. Huang, L. Li, Q. Yun, Z. Shi, B. Chen, H. Zhang, *ACS Nano* **2023**, *17*, 12935.
[31] C. Chen, G. Chen, H. Yang, G. Zhang, D. Hu, H. Chen, T. Guo, *J. Mater. Chem. C* **2017**, *5*, 9273.
[32] H. Yang, C. Chen, G. Zhang, S. Lan, H. Chen, T. Guo, *ACS Appl. Mater. Interfaces* **2017**, *9*, 3849.
[33] A. M. Ślusarz, K. Komorowska, T. Baraniecki, S. J. Zelewski, R. Kudrawiec, *ACS Sustain. Chem. Eng.* **2022**, *10*, 8196.
[34] S. Ravi-Kumar, B. Lies, X. Zhang, H. Lyu, H. Qin, *Polym. Int.* **2019**, *68*, 1391.
[35] S. Song, H. Hong, K. Y. Kim, K. K. Kim, J. Kim, D. Won, S. Yun, J. Choi, Y.-I. Ryu, K. Lee, J. Park, J. Kang, J. Bang, H. Seo, Y.-C. Kim, D. Lee, H. Lee, J. Lee, S.-W. Hwang, S. H. Ko, H. Jeon, W. Lee, *ACS Nano* **2023**, *17*, 21443.
[36] J. Bang, Y. Jung, H. Kim, D. Kim, M. Cho, S. H. Ko, *Nano-Micro Lett.* **2022**, *14*, 49.
[37] G. Bae, M. Kim, M. Jang, Y. M. Kwon, S. Yim, W. Song, S. Myung, S. S. Lee, T. Hasan, K. An, *Adv. Funct. Mater.* **2022**, *32*, 2204821.
[38] S. Zhu, Y. Xia, Y. Zhu, M. Wu, C. Jia, X. Wang, *Nano Energy* **2022**, *96*, 107116.
[39] H. Wang, H. Wang, Y. Wang, X. Su, C. Wang, M. Zhang, M. Jian, K. Xia, X. Liang, H. Lu, S. Li, Y. Zhang, *ACS Nano* **2020**, *14*, 3219.
[40] K. Brousse, S. Pinaud, S. Nguyen, P. F. Fazzini, R. Makarem, C. Josse, Y. Thimont, B. Chaudret, P. L. Taberna, M. Respaud, P. Simon, *Adv. Energy Mater.* **2020**, *10*, 1.
[41] S. Park, A. Lee, K.-H. Choi, S.-K. Hyeong, S. Bae, J.-M. Hong, T.-W. Kim, B. H. Hong, S.-K. Lee, *ACS Nano* **2020**, *14*, 8485.
[42] L. Yang, H. Hu, A. Scholz, F. Feist, G. Cadilha Marques, S. Kraus, N. M. Bojanowski, E. Blasco, C. Barner-Kowollik, J. Aghassi-Hagmann, M. Wegener, *Nat. Commun.* **2023**, *14*, 1103.
[43] L. Bezinge, J. M. Lesinski, A. Suea-Ngam, D. A. Richards, A. J. DeMello, C. J. Shih, *Adv. Mater.* **2023**, *35*, 2302893.
[44] J. Shin, B. Jeong, J. Kim, V. B. Nam, Y. Yoon, J. Jung, S. Hong, H. Lee, H. Eom, J. Yeo, J. Choi, D. Lee, S. H. Ko, *Adv. Mater.* **2020**, *32*, 1905527.
[45] M. I. Cohen, B. A. Unger, J. F. Milkosky, *Bell Syst. Tech. J.* **1968**, *47*, 385.
[46] J. Raamot, V. J. Zaleckas, *Appl. Opt.* **1974**, *13*, 1179.
[47] R. A. Becker, B. L. Sopori, W. S. C. Chang, *Appl. Opt.* **1978**, *17*, 1069.
[48] G. Hass, J. B. Ramsey, *Appl. Opt.* **1969**, *8*, 1115.
[49] V. Baranauskas, C. I. Z. Mammana, R. E. Klinger, J. E. Greene, *Appl. Phys. Lett.* **1980**, *36*, 930.
[50] J. C. C. Fan, H. J. Zeiger, *Appl. Phys. Lett.* **1975**, *27*, 224.
[51] H. Watanabe, H. Miki, S. Sugai, K. Kawasaki, T. Kioka, *Jpn. J. Appl. Phys.* **1994**, *33*, 4491.
[52] M. Bertolotti, *J. Sov. Laser Res.* **1985**, *6*, 395.
[53] J. C. Muller, E. Fogarassy, D. Salles, R. Stuck, P. M. Siffert, *IEEE Trans. Electron Devices* **1980**, *27*, 815.
[54] N. Misra, L. Xu, M. S. Rogers, S. H. Ko, C. P. Grigoropoulos, *Phys. Status Solidi Curr. Top. Solid State Phys.* **2008**, *5*, 3264.
[55] D. P. Norton, *Mater. Sci. Eng. R Reports* **2004**, *43*, 139.
[56] S. Y. Lee, E. S. Shim, H. S. Kang, S. S. Pang, J. S. Kang, *Thin Solid Films* **2005**, *473*, 31.
[57] P. M. Smith, P. G. Carey, T. W. Sigmon, *Appl. Phys. Lett.* **1997**, *70*, 342.
[58] E. D. Tsagarakis, C. Lew, M. O. Thompson, E. P. Giannelis, *Appl. Phys. Lett.* **2006**, *89*, 202910.
[59] J. Bohandy, B. F. Kim, F. J. Adrian, *J. Appl. Phys.* **1986**, *60*, 1538.
[60] A. Piqué, D. B. Chrisey, R. C. Y. Auyeung, J. Fitz-Gerald, H. D. Wu, R. A. McGill, S. Lakeou, P. K. Wu, V. Nguyen, M. Duignan, *Appl. Phys. A Mater. Sci. Process.* **1999**, *69*, S279.
[61] Z. Ur Rehman, F. Yang, M. Wang, T. Zhu, *Opt. Laser Technol.* **2023**, *160*, 109065.
[62] W. S. Wong, T. Sands, N. W. Cheung, M. Kneissl, D. P. Bour, P. Mei, L. T. Romano, N. M. Johnson, *Appl. Phys. Lett.* **1999**, *75*, 1360.
[63] Y. S. Liu, H. S. Cole, *MRS Proc.* **1988**, *129*, 579.
[64] L. Nánai, I. Hevesi, F. V. Bunkin, B. S. Luk'yanchuk, M. R. Brook, G. A. Shafeev, D. A. Jelski, Z. C. Wu, T. F. George, *Appl. Phys. Lett.* **1989**, *54*, 736.
[65] T. Tanaka, A. Ishikawa, S. Kawata, *Appl. Phys. Lett.* **2006**, *88*, 81107.
[66] Z. Chen, Y. Wei, C. Luo, K. Jiang, L. Zhang, Q. Li, S. Fan, J. Gao, *Appl. Phys. Lett.* **2007**, *90*, 133108.
[67] Y. Zhang, L. Guo, S. Wei, Y. He, H. Xia, Q. Chen, H. B. Sun, F. S. Xiao, *Nano Today* **2010**, *5*, 15.
[68] J. Liang, Y. Chen, Y. Xu, Z. Liu, L. Zhang, X. Zhao, X. Zhang, J. Tian, Y. Huang, Y. Ma, F. Li, *ACS Appl. Mater. Interfaces* **2010**, *2*, 3310.
[69] S. Feng, S. Cao, Z. Tian, H. Zhu, D. Kong, *ACS Appl. Mater. Interfaces* **2019**, *11*, 45844.
[70] G. Zhao, Y. Ling, Y. Su, Z. Z. Z. Chen, C. J. Mathai, O. Emeje, A. Brown, D. R. Alla, J. Huang, C. Kim, Q. Chen, X. He, D. Stalla, Y. Xu, Z. Z. Z. Chen, P. Y. Chen, S. Gangopadhyay, J. Xie, Z. Yan, *Sci. Adv.* **2022**, *8*, 9734.
[71] R. Park, D. H. Lee, C. S. Koh, Y. W. Kwon, S. Y. Chae, C. Kim, H. H. Jung, J. Jeong, S. W. Hong, *Adv. Healthc. Mater.* **2023**, *13*, 2301753.
[72] J. Lin, Z. Peng, Y. Liu, F. Ruiz-Zepeda, R. Ye, E. L. G. Samuel, M. J. Yacaman, B. I. Yakobson, J. M. Tour, *Nat. Commun.* **2014**, *5*, 5714.
[73] T. Jitsuno, K. Uno, in *Handb. Laser Micro- Nano-Engineering*, Springer International Publishing, Cham **2021**, pp. 1–23.
[74] X. Liu, D. Popa, N. Akhmediev, *Phys. Rev. Lett.* **2019**, *123*, 093901.
[75] J. Ren, D. Li, Y. Zhang, W. Yang, H. Y. Nie, Y. Liu, *ACS Appl. Electron. Mater.* **2021**, *4*, 2191.
[76] J. Zhang, R. Xu, J. Feng, Y. Xie, T. Zhou, *Ind. Eng. Chem. Res.* **2021**, *60*, 11161.
[77] Z. Bayhan, J. K. El-Demellawi, J. Yin, Y. Khan, Y. Lei, E. Alhajji, Q. Wang, M. N. Hedhili, H. N. Alshareef, *Small* **2023**, 2208253.
[78] H. Zhang, Y. Sun, Q. Li, C. Wan, *ACS Sustain. Chem. Eng.* **2022**, *10*, 11501.
[79] W. Yu, W. Zhao, S. Wang, Q. Chen, X. Liu, *Adv. Mater.* **2023**, *35*, 2209545.
[80] T. Yeamsuksawat, L. Zhu, T. Kasuga, M. Nogi, H. Koga, *RSC Adv.* **2023**, *13*, 17556.
[81] X. Zang, C. Jian, T. Zhu, Z. Fan, W. Wang, M. Wei, B. Li, M. Follmar Diaz, P. Ashby, Z. Lu, Y. Chu, Z. Wang, X. Ding, Y. Xie, J. Chen, J. N. Hohman, M. Sanghadasa, J. C. Grossman, L. Lin, *Nat. Commun.* **2019**, *10*, 3112.
[82] Y. Li, X. Zhou, J. Chen, W. Guo, S. He, S. Gao, P. Peng, *Adv. Mater. Interfaces* **2020**, *7*, 1901845.
[83] Y. Ji, Y. Liao, H. Li, Y. Cai, D. Fan, Q. Liu, S. Huang, R. Zhu, S. Wang, H. Wang, L. Guo, *ACS Appl. Mater. Interfaces* **2022**, *14*, 11971.
[84] F. Morosawa, S. Hayashi, M. Terakawa, *ACS Sustain. Chem. Eng.* **2021**, *9*, 2955.
[85] Y. Wei, J. Chen, L. Liang, J. Wang, H. Zeng, *ACS Appl. Nano Mater.* **2022**, *2022*, 11020.
[86] V. B. Nam, J. Shin, Y. Yoon, T. T. Giang, J. Kwon, Y. D. Suh, J. Yeo, S. Hong, S. H. Ko, D. Lee, *Adv. Funct. Mater.* **2019**, *29*, 1806895.
[87] V. Binh Nam, T. Thi Giang, D. Lee, *Appl. Surf. Sci.* **2021**, *570*, 151179.
[88] J. Yeo, S. Hong, D. Lee, N. Hotz, M. T. Lee, C. P. Grigoropoulos, S. H. Ko, *PLoS One* **2012**, *7*, 42315.
[89] J. Zhang, J. Feng, L. Jia, H. Zhang, G. Zhang, S. Sun, T. Zhou, *ACS Appl. Mater. Interfaces* **2019**, *11*, 13714.
[90] D. Moskal, J. Martan, M. Honner, *Micromachines* **2023**, *14*, 1241.
[91] R. Kumar, A. Pérez del Pino, S. Sahoo, R. K. Singh, W. K. Tan, K. K. Kar, A. Matsuda, E. Joanni, *Prog. Energy Combust. Sci.* **2022**, *91*, 100981.

[92] M. Devi, H. Wang, S. Moon, S. Sharma, V. Strauss, *Adv. Mater.* **2023**, 2211054.
[93] S. Chatani, C. J. Kloxin, C. N. Bowman, *Polym. Chem.* **2014**, *5*, 2187.
[94] H. Palneedi, J. H. Park, D. Maurya, M. Peddigari, G. T. Hwang, V. Annapureddy, J. W. Kim, J. J. Choi, B. D. Hahn, S. Priya, K. J. Lee, J. Ryu, *Adv. Mater.* **2018**, *30*, 1705148.
[95] P. I. C. Claro, T. Pinheiro, S. L. Silvestre, A. C. Marques, J. Coelho, J. M. Marconcini, E. Fortunato, L. H. C. Mattoso, R. Martins, P. I. Pedro, T. Pinheiro, S. L. Silvestre, A. C. Marques, J. Coelho, J. M. Marconcini, E. Fortunato, L. H. Luiz, R. Martins, *Appl. Phys. Rev.* **2022**, *9*, 041305.
[96] C. Song, M. Guan, Y. Jia, D. Chen, J. Xu, C. Zhang, S. Meng, *npj Comput. Mater.* **2023**, *9*, 1.
[97] I. Bunaziv, O. M. Akselsen, X. Ren, B. Nyhus, M. Eriksson, *Metals (Basel)* **2021**, *11*, 1150.
[98] H. Nishiyama, K. Umetsu, K. Kimura, *Sci. Rep.* **2019**, *9*, 1.
[99] G. E. Lio, A. Ferraro, T. Ritacco, D. M. Aceti, A. De Luca, M. Giocondo, R. Caputo, *Adv. Mater.* **2021**, *33*, 2008644.
[100] Y. Bougdid, I. Maouli, A. Rahmouni, K. Mochizuki, I. Bennani, M. Halim, Z. Sekkat, *J. Micromech. Microeng.* **2019**, *29*, 035018.
[101] S. G. Kwon, J. Kang, S. Back, B. Kang, *ACS Sustain. Chem. Eng.* **2020**, *8*, 11348.
[102] O. Geladari, M. Eberle, A. Maier, F. Fetzer, T. Chassé, A. J. Meixner, M. Scheele, A. Schnepf, K. Braun, *Small Methods* **2023**, *7*, 2201221.
[103] S. Bai, S. Zhang, W. Zhou, D. Ma, Y. Ma, P. Joshi, A. Hu, *Nano-Micro Lett.* **2017**, *9*, 1.
[104] Y. Chyan, R. Ye, Y. Li, S. P. Singh, C. J. Arnusch, J. M. Tour, *ACS Nano* **2018**, *12*, 2176.
[105] J. Yun, M. Yang, B. Kang, *ACS Sustain. Chem. Eng.* **2018**, *6*, 4940.
[106] T. Pinheiro, A. Rosa, C. Ornelas, J. Coelho, E. Fortunato, A. C. Marques, R. Martins, *Carbon Trends* **2023**, *11*, 100271.
[107] T. Zhang, C. Wu, Y. Rong, M. Li, Y. Huang, G. Zhang, *Mater. Manuf. Process.* **2022**, *37*, 809.
[108] M. Abdulhafez, G. N. Tomaraei, M. Bedewy, *ACS Appl. Nano Mater.* **2021**, *4*, 2973.
[109] J. Zhang, J. Han, G. Peng, X. Yang, X. Yuan, Y. Li, J. Chen, W. Xu, K. Liu, Z. Zhu, W. Cao, Z. Han, J. Dai, M. Zhu, S. Qin, K. S. Novoselov, *Light Sci. Appl.* **2020**, *9*, 174.
[110] D. J. Joe, S. Kim, J. H. Park, D. Y. Park, H. E. Lee, T. H. Im, I. Choi, R. S. Ruoff, K. J. Lee, *Adv. Mater.* **2017**, *29*, 1606586.
[111] A. Bajpai, P. Kumbhakar, C. S. Tiwary, K. Biswas, *ACS Sustain. Chem. Eng.* **2021**, *12*, 20.
[112] A. Shahbazi, A. Koohian, K. Madanipour, *Laser Phys.* **2017**, *27*, 016101.
[113] C.-C. Yang, M.-W. Hung, H.-Y. Tsai, W.-N. Chuang, K.-C. Huang, *Appl. Phys. A* **2016**, *122*, 441.
[114] F. Antolini, F. Limosani, R. Carcione, *Nanomaterials* **2022**, *12*, 1551.
[115] J. Jones, M. R. Snowdon, S. Rathod, P. Peng, *Flex. Print. Electron.* **2023**, *8*, 015008.
[116] T. Pinheiro, S. Silvestre, J. Coelho, A. C. Marques, R. Martins, M. G. F. Sales, E. Fortunato, *Adv. Mater. Interfaces* **2021**, *8*, 2101502.
[117] J. Coelho, R. F. Correia, S. Silvestre, T. Pinheiro, A. C. Marques, M. R. P. Correia, J. V. Pinto, E. Fortunato, R. Martins, *Microchim. Acta* **2023**, *190*, 40.
[118] S. K. Saha, B. Au, J. S. Oakdale, *Adv. Eng. Mater.* **2019**, *21*, 1900583.
[119] E. H. Waller, S. Duran, G. von Freymann, *Nanophotonics* **2023**, *12*, 1549.
[120] R. Murray, M. Burke, D. Iacopino, A. J. Quinn, *ACS Omega* **2021**, *6*, 16736.
[121] B. Guo, J. Sun, Y. Hua, N. Zhan, J. Jia, K. Chu, *Nanomanufacturing Metrol.* **2020**, *3*, 26.
[122] G. Raciukaitis, *IEEE J. Sel. Top. Quantum Electron.* **2021**, *27*, 1.
[123] Y.-S. Chen, C.-C. Wang, J.-L. You, C.-P. Chang, B.-W. Lai, M.-D. Ger, *Int. J. Electrochem. Sci.* **2021**, *16*, 21112.
[124] E. Greenberg, N. Armon, O. Kapon, M. Ben-Ishai, H. Shpaisman, *Adv. Mater. Interfaces* **2019**, *6*, 1900541.
[125] R. Ye, Y. Chyan, J. Zhang, Y. Li, X. Han, C. Kittrell, J. M. Tour, *Adv. Mater.* **2017**, *29*, 1702211.
[126] Z. Zhang, W. Yang, L. Cheng, W. Cao, M. Sain, J. Tan, A. Wang, H. Jia, *ACS Sustain. Chem. Eng.* **2020**, *8*, 17629.
[127] M. Mizoshiri, K. Yoshidomi, *Materials (Basel)*. **2021**, *14*, 3285.
[128] Z. Zhang, L. Song, L. Cheng, J. Tan, W. Yang, *ACS Sustain. Chem. Eng.* **2022**, *10*, 8086.
[129] M. Wable, M. Furquan, M. Paygude, A. Shetti, S. Ogale, A. Banerjee, *ACS Appl. Energy Mater.* **2022**, *5*, 10940.
[130] Z. Zhang, Z. Wang, F. Wang, T. Qin, H. Zhu, P. Liu, G. Zhao, X. Wang, F. Kang, L. Wang, C. Yang, *Small* **2023**, *19*, 2300747.
[131] R. Rahimi, S. Shams Es-haghi, S. Chittiboyina, Z. Mutlu, S. A. Lelièvre, M. Cakmak, B. Ziaie, *Adv. Healthc. Mater.* **2018**, *7*, 1800231.
[132] S. Lee, S. Jeon, *ACS Sustain. Chem. Eng.* **2019**, *7*, 2270.
[133] B. Wang, R. Peng, X. Wang, Y. Yang, E. Wang, Z. Xin, Y. Sun, C. Li, Y. Wu, J. Wei, J. Sun, K. Liu, *ACS Nano* **2021**, *15*, 10502.
[134] J. P. Kruth, X. Wang, T. Laoui, L. Froyen, *Assem. Autom.* **2003**, *23*, 357.
[135] S. Agarwala, G. L. Goh, T. S. Dinh Le, J. An, Z. K. Peh, W. Y. Yeong, Y. J. Kim, *ACS Sensors* **2019**, *4*, 218.
[136] A. A. Serkov, H. V. Snelling, S. Heusing, T. M. Amaral, *Sci. Rep.* **2019**, *9*, 1773.
[137] H. Min, B. Lee, S. Jeong, M. Lee, *Opt. Laser Technol.* **2017**, *88*, 128.
[138] N. Hayati-Roodbari, A. Wheeldon, C. Hendler, A. Fian, R. Trattnig, *Nanotechnology* **2021**, *32*, 225205.
[139] Y. Wang, T. Ouyang, L. Meng, L. Wu, W. Bai, S. Zhang, X. Zeng, *ACS Appl. Mater. Interfaces* **2023**, *15*, 19209.
[140] Y. Yang, Z. Li, S. Yang, Y. Li, J. Huang, *Int. J. Heat Mass Transf.* **2020**, *159*, 120110.
[141] A. Sharif, N. Farid, P. McGlynn, M. Wang, R. K. Vijayaraghavan, A. Jilani, G. Leen, P. J. McNally, G. M. O'Connor, *J. Phys. D. Appl. Phys.* **2023**, *56*, 075102.
[142] A. I. Titkov, O. A. Logutenko, A. M. Vorobyev, T. A. Borisenko, N. V. Bulina, A. S. Ulihin, S. G. Baev, V. P. Bessmeltsev, N. Z. Lyakhov, *Mater. Today Proc.* **2020**, *25*, 447.
[143] J. Kwon, H. Cho, Y. D. Suh, J. Lee, H. Lee, J. Jung, D. Kim, D. Lee, S. Hong, S. H. Ko, *Adv. Mater. Technol.* **2017**, *2*, 1600222.
[144] J. Kwon, H. Cho, H. Eom, H. Lee, Y. D. Suh, H. Moon, J. Shin, S. Hong, S. H. Ko, *ACS Appl. Mater. Interfaces* **2016**, *8*, 11575.
[145] R. van Dommelen, R. I. Haque, O. Chandran, S. Lani, D. Briand, *Flex. Print. Electron.* **2021**, *6*, 045003.
[146] E. Balliu, H. Andersson, M. Engholm, T. Öhlund, H.-E. Nilsson, H. Olin, *Sci. Rep.* **2018**, *8*, 10408.
[147] Y. Y. Y. Chen, S. F. Hung, W. K. Lo, Y. Y. Y. Chen, Y. Shen, K. Kafenda, J. Su, K. Xia, S. Yang, *Nat. Commun.* **2020**, *11*, 5334.
[148] J. Noh, J. Ha, D. Kim, *Appl. Surf. Sci.* **2020**, *511*, 145574.
[149] V. B. Nam, J. Shin, A. Choi, H. Choi, S. H. Ko, D. Lee, *J. Mater. Chem. C* **2021**, *9*, 5652.
[150] W. Shou, B. K. Mahajan, B. Ludwig, X. Yu, J. Staggs, X. Huang, H. Pan, *Adv. Mater.* **2017**, *29*, 1700172.
[151] S. Feng, Z. Tian, J. Wang, S. Cao, D. Kong, *Adv. Electron. Mater.* **2019**, *5*, 1800693.
[152] Y. Yu, M. Chen, S. Wang, C. Hill, P. Joshi, T. Kuruganti, A. Hu, *J. Electrochem. Soc.* **2018**, *165*, A584.
[153] A. Sharif, N. Farid, G. M. O'Connor, *Results Eng.* **2022**, *16*, 100731.
[154] L. Yang, Y. Gan, Y. Zhang, J. K. Chen, *Appl. Phys. A Mater. Sci. Process.* **2012**, *106*, 725.
[155] Y. Zhang, L. Wu, X. Guo, Y.-G. Jung, J. Zhang, *Comput. Mater. Sci.* **2016**, *125*, 105.
[156] S. Tabrizi, Y. Cao, H. Lin, B. Jia, *Sci. China Physics, Mech. Astron.* **2017**, *60*, 034201.
[157] T. Lipateva, A. Lipatiev, S. Lotarev, G. Shakhgildyan, S. Fedotov, V. Sigaev, *Materials (Basel)* **2022**, *15*, 6867.

[158] T. Palmer, E. H. Waller, H. Andrä, K. Steiner, G. von Freymann, *ACS Appl. Nano Mater.* **2021**, *4*, 8872.
[159] B.-B. Xu, H. Xia, L.-G. Niu, Y.-L. Zhang, K. Sun, Q.-D. Chen, Y. Xu, Z.-Q. Lv, Z.-H. Li, H. Misawa, H.-B. Sun, *Small* **2010**, *6*, 1762.
[160] M. Cui, T. Huang, R. Xiao, *Appl. Surf. Sci.* **2022**, *588*, 152915.
[161] M. Cui, T. Huang, Z. Peng, L. Xing, Z. Zhou, L. Guo, J. Wang, J. Xu, R. Xiao, *Adv. Mater. Technol.* **2023**, *8*, 2201610.
[162] E. H. Waller, J. Karst, G. von Freymann, *Light Adv. Manuf.* **2021**, *2*, 228.
[163] T. Komori, T. Furukawa, M. Iijima, S. Maruo, *Opt. Express* **2020**, *28*, 8363.
[164] X. Zhou, W. Guo, Q. Sun, L. Sun, P. Peng, *ACS Appl. Electron. Mater.* **2023**, *5*, 3780.
[165] K. Setoura, S. Ito, M. Yamada, H. Yamauchi, H. Miyasaka, *J. Photochem. Photobiol. A Chem.* **2017**, *344*, 168.
[166] P. Barton, S. Mukherjee, J. Prabha, B. W. Boudouris, L. Pan, X. Xu, *Nanotechnology* **2017**, *28*, 505302.
[167] W. Zhou, S. Bai, Y. Ma, D. Ma, T. Hou, X. Shi, A. Hu, *ACS Appl. Mater. Interfaces* **2016**, *8*, 24887.
[168] X. Zhou, W. Guo, Y. Yao, R. Peng, P. Peng, *Adv. Eng. Mater.* **2021**, *23*, 1.
[169] X. Zhou, W. Guo, P. Peng, *Nano-Micro Lett.* **2021**, *13*, 184.
[170] J. Liao, W. Guo, P. Peng, *Opt. Lasers Eng.* **2021**, *142*, 106605.
[171] X. Zhou, W. Guo, J. Fu, Y. Zhu, Y. Huang, P. Peng, *Appl. Surf. Sci.* **2019**, *494*, 684.
[172] E. A. Avilova, E. M. Khairullina, A. Y. Shishov, E. A. Eltysheva, V. Mikhailovskii, D. A. Sinev, I. I. Tumkin, *Nanomaterials* **2022**, *12*, 1127.
[173] C. Wang, Z. Zhao, R. Wu, X. Shi, G. F. Payne, X. Wang, *ACS Sustain. Chem. Eng.* **2023**, *11*, 9782.
[174] S. Moussa, G. Atkinson, M. SamyEl-Shall, A. Shehata, K. M. AbouZeid, M. B. Mohamed, *J. Mater. Chem.* **2011**, *21*, 9608.
[175] J. Zhao, Z. Yu, Z. Tu, H. Bian, *Micromachines* **2022**, *13*, 992.
[176] B. Kang, S. Han, J. Kim, S. Ko, M. Yang, *J. Phys. Chem. C* **2011**, *115*, 23664.
[177] Y. Huang, X. Xie, M. Li, M. Xu, J. Long, *Opt. Express* **2021**, *29*, 4453.
[178] M. Mizoshiri, S. Hata, *Res. Rev. J. Mater. Sci.* **2016**, *04*, 47.
[179] D. Paeng, D. Lee, J. Yeo, J. H. Yoo, F. I. Allen, E. Kim, H. So, H. K. Park, A. M. Minor, C. P. Grigoropoulos, *J. Phys. Chem. C* **2015**, *119*, 6363.
[180] M. Mizoshiri, K. Yoshidomi, N. Darkhanbaatar, E. M. Khairullina, I. I. Tumkin, *Nanomaterials* **2021**, *11*, 3356.
[181] M. Mizoshiri, S. Hata, *Appl. Phys. A* **2018**, *124*, 64.
[182] M. Mizoshiri, K. Nishitani, S. Hata, *Micromachines* **2018**, *9*, 264.
[183] Z. Wan, E. W. Streed, M. Lobino, S. Wang, R. T. Sang, I. S. Cole, D. V. Thiel, Q. Li, *Adv. Mater. Technol.* **2018**, *3*, 1700315.
[184] V. P. Veiko, A. G. Poleshchuk, in *Springer Ser. Mater. Sci.*, Springer Verlag, Berlin **2014**, pp. 149–171.
[185] H. Bandhu, P. Ashok, D. P. Khandapu, A. Verma, *Opt. Laser Technol.* **2023**, *167*, 109673.
[186] A. C. Castonguay, N. Yi, B. Li, J. Zhao, H. Li, Y. Gao, N. N. Nova, N. Tiwari, L. D. Zarzar, H. Cheng, *ACS Appl. Mater. Interfaces* **2022**, *14*, 28163.
[187] H. Kwon, J. Kim, K. Ko, M. J. Matthews, J. Suh, H.-J. Kwon, J.-H. Yoo, *Appl. Surf. Sci.* **2021**, *540*, 148333.
[188] L. Nánai, R. Vajtai, T. F. George, *Thin Solid Films* **1997**, *298*, 160.
[189] O. De Melo, F. Agulló-Rueda, V. Torres-Costa, *J. Mater. Chem. C* **2021**, *9*, 6579.
[190] W. Zheng, P. Li, Z. Wang, N. H. Golshan, K. S. Ziemer, M. Su, *J. Magn. Magn. Mater.* **2019**, *489*, 165419.
[191] C. Kindle, A. Castonguay, S. McGee, J. A. Tomko, P. E. Hopkins, L. D. Zarzar, *ACS Appl. Nano Mater.* **2019**, *2*, 2581.
[192] J. Yeo, S. Hong, G. Kim, H. Lee, Y. D. Suh, I. Park, C. P. Grigoropoulos, S. H. Ko, *ACS Nano* **2015**, *9*, 6059.
[193] H. Kong, H. Kim, S. Hwang, J. Mun, J. Yeo, *ACS Appl. Nano Mater.* **2022**, *5*, 4102.
[194] C. Xiao, J. Feng, H. Xu, R. Xu, T. Zhou, *ACS Appl. Mater. Interfaces* **2022**, *14*, 20000.
[195] H. Xu, J. Zhang, J. Feng, T. Zhou, *Ind. Eng. Chem. Res.* **2021**, *60*, 8821.
[196] H. Xu, J. Feng, C. Xiao, R. Xu, Y. Xie, T. Zhou, *ACS Appl. Mater. Interfaces* **2022**, *14*, 31411.
[197] T.-H. Lee, S.-M. Hwang, M.-J. Yoo, *J. Eur. Ceram. Soc.* **2020**, *40*, 1390.
[198] B. Yan, X. Huang, X. Song, L. Kang, Q. Le, K. Jiang, *J. Electrochem. Sci. Eng.* **2018**, *8*, 331.
[199] J. Zhang, T. Zhou, L. Wen, A. Zhang, *ACS Appl. Mater. Interfaces* **2016**, *8*, 33999.
[200] M. Gedvilas, K. Ratautas, A. Jagminiene, I. Stankevičiene, N. Li Pira, S. Sinopoli, E. Kacar, E. Norkus, G. Račiukaitis, *RSC Adv.* **2018**, *8*, 30305.
[201] B. Yoo, D. Bowen, N. Lazarus, D. Pines, *ACS Appl. Mater. Interfaces* **2022**, *14*, 18854.
[202] J. Zhang, T. Zhou, Y. Xie, L. Wen, *Adv. Mater. Interfaces* **2017**, *4*, 1700937.
[203] Y. Huang, X. Xie, J. Cui, W. Zhou, J. Chen, J. Long, *Opt. Express* **2022**, *30*, 19544.
[204] J. Cai, C. Lv, A. Watanabe, *ACS Appl. Mater. Interfaces* **2018**, *10*, 915.
[205] Y. Xie, H. Zhang, J. Zhang, T. Zhou, *Energy Storage Mater.* **2022**, *51*, 139.
[206] M. K. Camargo, M. Uebel, M. Kurniawan, K. F. Ziegler, M. Seiler, R. Grieseler, U. Schmidt, A. Barz, J. Bliedtner, A. Bund, *Adv. Eng. Mater.* **2022**, *24*, 2100933.
[207] G. Hu, H. Zhu, H. Guo, S. Wang, Y. Sun, J. Zhang, Y. Lin, D. Kong, *ACS Appl. Mater. Interfaces* **2023**, *15*, 28675.
[208] H. Xu, J. Feng, F. Yu, J. Huang, T. Zhou, *Ind. Eng. Chem. Res.* **2023**, *62*, 395.
[209] H. Zhang, J. Zhang, G. Su, T. Zhou, A. Zhang, *Compos. Sci. Technol.* **2020**, *190*, 108045.
[210] C. Dupas-Bruzek, P. Dréan, D. Derozier, *J. Appl. Phys.* **2009**, *106*, 74913.
[211] K. Li, Y. Wang, Z. Jiang, H. S. Wong, T. Zhou, J. Wu, J. Zhang, A. Zhang, *Cem. Concr. Compos.* **2022**, *128*, 104423.
[212] L. Wang, Z. Fu, R. Suess-Wolf, N. Travitzky, P. Greil, J. Franke, R. Suess-Wolf, N. Travitzky, P. Greil, J. Franke, *Adv. Eng. Mater.* **2019**, *21*, 1900096.
[213] F. Zhao, C. Jiao, D. Xie, B. Lu, M. Qiu, X. Yi, J. Liu, C. Wang, L. Shen, Z. Tian, *RSC Adv.* **2020**, *10*, 44015.
[214] F. Liu, D. Xie, C. Jiao, D. Bai, H. Wu, L. Shen, Z. Tian, J. Zhao, *J. Mater. Sci.* **2022**, *57*, 1506.
[215] A. Vashisth, M. Kowalik, J. C. Gerringer, C. Ashraf, A. C. T. Van Duin, M. J. Green, *ACS Appl. Nano Mater.* **2020**, *3*, 1881.
[216] H. Wang, S. Delacroix, A. Zieleniewska, J. Hou, N. V Tarakina, D. Cruz, I. Lauermann, A. J. Ferguson, J. L. Blackburn, V. Strauss, *Adv. Funct. Mater.* **2021**, *31*, 2104061.
[217] C. H. Dreimol, H. Guo, M. Ritter, T. Keplinger, Y. Ding, R. Günther, E. Poloni, I. Burgert, G. Panzarasa, *Nat. Commun.* **2022**, *13*, 3680.
[218] Y. Song, N. Li, S. Han, S. Zhang, L. Chen, Z. Li, X. Yu, C. Liu, M. Xi, G. Wu, W. Wang, Z. Wang, *Adv. Funct. Mater.* **2023**, *33*, 2305191.
[219] J. I. Raffel, J. F. Freidin, G. H. Chapman, *Appl. Phys. Lett.* **1983**, *42*, 705.
[220] T. Pinheiro, R. Correia, M. Morais, J. Coelho, E. Fortunato, M. G. F. Sales, A. C. Marques, R. Martins, *ACS Nano* **2022**, *16*, 20633.
[221] Q.-M. Huang, H. Yang, S. Wang, X. Liu, C. Tan, A. Luo, S. Xu, G. Zhang, H. Ye, *ACS Appl. Nano Mater.* **2023**, *6*, 10453.
[222] Y. Huang, L. Zeng, C. Liu, D. Zeng, Z. Liu, X. Liu, X. Zhong, W. Guo, L. Li, *Small* **2018**, *14*, 1803143.
[223] T. D. Le, S. Park, J. An, P. S. Lee, Y. Kim, *Adv. Funct. Mater.* **2019**, *29*, 1902771.

[224] A. F. Carvalho, A. J. S. Fernandes, R. Martins, E. Fortunato, F. M. Costa, *Adv. Mater. Technol.* **2020**, *5*, 2000630.
[225] B. Kulyk, B. F. R. Silva, A. F. Carvalho, P. Barbosa, A. V. Girão, J. Deuermeier, A. J. S. Fernandes, F. M. L. Figueiredo, E. Fortunato, F. M. Costa, *Adv. Mater. Technol.* **2022**, *7*, 2101311.
[226] A. Imbrogno, J. Islam, C. Santillo, R. Castaldo, L. Sygellou, C. Larrigy, R. Murray, E. Vaughan, M. K. Hoque, A. J. Quinn, D. Iacopino, *ACS Appl. Electron. Mater.* **2022**, *4*, 1541.
[227] Y. Gao, Q. Li, R. Wu, J. Sha, Y. Lu, F. Xuan, *Adv. Funct. Mater.* **2019**, *29*, 1806786.
[228] A. F. Carvalho, A. J. S. Fernandes, C. Leitão, J. Deuermeier, A. C. Marques, R. Martins, E. Fortunato, F. M. Costa, *Adv. Funct. Mater.* **2018**, *28*, 1805271.
[229] M. Terakawa, in *Handb. Laser Micro- Nano-Engineering*, Springer International Publishing, Cham **2021**, pp. 857–878.
[230] Y. Chen, J. Long, S. Zhou, D. Shi, Y. Huang, X. Chen, J. Gao, N. Zhao, C. Wong, *Small Methods* **2019**, *3*, 1900208.
[231] M. Wang, Y. Yang, W. Gao, *Trends Chem.* **2021**, *3*, 969.
[232] P. Nayak, N. Kurra, C. Xia, H. N. Alshareef, *Adv. Electron. Mater.* **2016**, *2*, 1600185.
[233] T. S. D. Le, H. P. Phan, S. Kwon, S. Park, Y. Jung, J. Min, B. J. Chun, H. Yoon, S. H. Ko, S. W. Kim, Y. J. Kim, *Adv. Funct. Mater.* **2022**, *32*, 2205158.
[234] F. M. Vivaldi, A. Dallinger, A. Bonini, N. Poma, L. Sembranti, D. Biagini, P. Salvo, F. Greco, F. Di Francesco, *ACS Appl. Mater. Interfaces* **2021**, *13*, 30245.
[235] L. Huang, J. Su, Y. Song, R. Ye, *Nano-Micro Lett.* **2020**, *12*, 1.
[236] K. Muzyka, G. Xu, *Electroanalysis* **2022**, *34*, 574.
[237] Y. Li, D. X. Luong, J. Zhang, Y. R. Tarkunde, C. Kittrell, F. Sargunaraj, Y. Ji, C. J. Arnusch, J. M. Tour, *Adv. Mater.* **2017**, *29*, 1700496.
[238] A. Dallinger, F. Steinwender, M. Gritzner, F. Greco, *ACS Appl. Nano Mater.* **2023**, *6*, 16201.
[239] S. H. Ko, H. Pan, C. P. Grigoropoulos, C. K. Luscombe, J. M. J. Fréchet, D. Poulikakos, *Appl. Phys. Lett.* **2007**, *90*, 141103.
[240] Y. Son, J. Yeo, H. Moon, T. W. Lim, S. Hong, K. H. Nam, S. Yoo, C. P. Grigoropoulos, D. Yang, S. H. Ko, *Adv. Mater.* **2011**, *23*, 3176.
[241] W. Di Cianni, M. de la Mata, F. J. Delgado, G. Desiderio, S. I. Molina, A. S. de León, M. Giocondo, *Int. J. Mol. Sci.* **2021**, *22*, 7465.
[242] J. Lim, J. Ham, W. Lee, E. Hwang, W. Lee, S. Hong, *Nanomaterials* **2021**, *11*, 1921.
[243] E. Edri, N. Armon, E. Greenberg, S. Moshe-Tsurel, D. Lubotzky, T. Salzillo, I. Perelshtein, M. Tkachev, O. Girshevitz, H. Shpaisman, *ACS Appl. Mater. Interfaces* **2021**, *13*, 36416.
[244] A. Soltani, B. Khorramdel Vahed, A. Mardoukhi, M. Mäntysalo, *Nanotechnology* **2015**, *27*, 035203.
[245] G. Yang, G. Xu, Q. Li, Y. Zeng, Y. Zhang, M. Hao, C. Cui, *J. Phys. D. Appl. Phys.* **2021**, *54*, 375304.
[246] D. Shestakov, E. Khairullina, A. Shishov, S. Khubezhov, S. Makarov, I. Tumkin, L. Logunov, *Opt. Laser Technol.* **2023**, *167*, 109777.
[247] H. Lee, M. Yang, *Appl. Phys. A* **2015**, *119*, 317.
[248] K. Brousse, S. Nguyen, A. Gillet, S. Pinaud, R. Tan, A. Meffre, K. Soulantica, B. Chaudret, P. L. Taberna, M. Respaud, P. Simon, *Electrochim. Acta* **2018**, *281*, 816.
[249] J. Zhang, Y. Zou, S. Eickelmann, C. Njel, T. Heil, S. Ronneberger, V. Strauss, P. H. Seeberger, A. Savateev, F. F. Loeffler, *Nat. Commun.* **2021**, *12*, 1.
[250] K. Brousse, P. L. Taberna, P. Simon, *J. Electrochem. Soc.* **2022**, *169*, 070534.
[251] S. Manzeli, D. Ovchinnikov, D. Pasquier, O. V. Yazyev, A. Kis, *Nat. Rev. Mater.* **2017**, *2*, 17033.
[252] M. Xu, J. Gao, J. Song, H. Wang, L. Zheng, Y. Wei, Y. He, X. Wang, W. Huang, *iScience* **2021**, *24*, 103313.
[253] S. Park, J. Park, Y. Kim, S. Bae, T.-W. Kim, K.-I. Park, B. H. Hong, C. K. Jeong, S.-K. Lee, *Nano Energy* **2020**, *78*, 105266.
[254] O. A. Abbas, A. H. Lewis, N. Aspiotis, C. C. Huang, I. Zeimpekis, D. W. Hewak, P. Sazio, S. Mailis, *Sci. Rep.* **2021**, *11*, 1.
[255] A. V. Averchenko, I. A. Salimon, E. V. Zharkova, S. Lipovskikh, P. Somov, O. A. Abbas, P. G. Lagoudakis, S. Mailis, *Mater. Today Adv.* **2023**, *17*, 100351.
[256] D. Austin, K. Gliebe, C. Muratore, B. Boyer, T. S. Fisher, L. K. Beagle, A. Benton, P. Look, D. Moore, E. Ringe, B. Treml, A. Jawaid, R. Vaia, W. Joshua Kennedy, P. Buskohl, N. R. Glavin, *Mater. Today* **2021**, *43*, 17.
[257] X. Zang, C. Shen, Y. Chu, B. Li, M. Wei, J. Zhong, M. Sanghadasa, L. Lin, *Adv. Mater.* **2018**, *30*, 1800062.
[258] X. Zang, D. Xing, W. Tang, L. Lu, Y. Xie, K. Siong Teh, M. Sanghadasa, L. Lin, *Mater. Lett.* **2020**, *271*, 127784.
[259] R. D. Rodriguez, S. Shchadenko, G. Murastov, A. Lipovka, M. Fatkullin, I. Petrov, T. H. Tran, A. Khalelov, M. Saqib, N. E. Villa, V. Bogoslovskiy, Y. Wang, C. G. Hu, A. Zinovyev, W. Sheng, J. J. Chen, I. Amin, E. Sheremet, *Adv. Funct. Mater.* **2021**, *31*, 2008818.
[260] V. Nair, J. Yi, D. Isheim, M. Rotenberg, L. Meng, F. Shi, X. Chen, X. Gao, A. Prominski, Y. Jiang, J. Yue, C. T. Gallagher, D. N. Seidman, B. Tian, *Sci. Adv.* **2020**, *6*, aaz2743.
[261] L. Lu, D. Zhang, Y. Xie, H. He, W. Wang, *Adv. Mater. Technol.* **2022**, *7*, 2200441.
[262] M. Bowden, D. J. Gardiner, J. M. Southall, *J. Appl. Phys.* **1992**, *71*, 521.
[263] I. A. Salama, N. R. Quick, A. Kar, *J. Appl. Phys.* **2003**, *93*, 9275.
[264] I. A. Salama, N. R. Quick, A. Kar, *J. Laser Appl.* **2004**, *16*, 92.
[265] R. You, Y. Q. Liu, Y. L. Hao, D. D. Han, Y. L. Zhang, Z. You, *Adv. Mater.* **2020**, *32*, 1901981.
[266] M. Tavakkoli Gilavan, M. S. Rahman, A. Minhas-Khan, S. Nambi, G. Grau, *ACS Appl. Electron. Mater.* **2021**, *3*, 3867.
[267] A. Z. Yazdi, I. O. Navas, A. Abouelmagd, U. Sundararaj, *Macromol. Rapid Commun.* **2017**, *38*, 1700176.
[268] R. Correia, J. Deuermeier, M. R. Correia, J. Vaz Pinto, J. Coelho, E. Fortunato, R. Martins, *ACS Appl. Mater. Interfaces* **2022**, *14*, 46427.
[269] D. Yang, H. K. Nam, T.-S. D. Le, J. Yeo, Y. Lee, Y.-R. Kim, S.-W. Kim, H.-J. Choi, H. C. Shim, S. Ryu, S. Kwon, Y.-J. Kim, *ACS Nano* **2023**, *17*, 18893.
[270] G. Wang, L.-Q. Q. Tao, Z. Peng, C. Zhu, H. Sun, S. Zou, T. Li, P. Wang, X. Chen, T.-L. L. Ren, *Carbon N. Y.* **2022**, *193*, 68.
[271] X. Sun, H. Jin, W. Qu, *RSC Adv.* **2021**, *11*, 19695.
[272] M. G. Stanford, J. T. Li, Y. Chyan, Z. Wang, W. Wang, J. M. Tour, *ACS Nano* **2019**, *13*, 7166.
[273] S. L. Silvestre, T. Pinheiro, A. C. Marques, J. Deuermeier, J. Coelho, R. Martins, L. Pereira, E. Fortunato, *Flex. Print. Electron.* **2022**, *7*, 035021.
[274] E. Vaughan, C. Santillo, M. Setti, C. Larrigy, A. J. Quinn, G. Gentile, M. Lavorgna, D. Iacopino, *Adv. Sens. Res.* **2023**, *2*, 2300026.
[275] W. Zhang, Y. Lei, F. Ming, Q. Jiang, P. M. F. J. Costa, H. N. Alshareef, *Adv. Energy Mater.* **2018**, *8*, 1801840.
[276] Y. Lei, A. H. Alshareef, W. Zhao, S. Inal, *ACS Appl. Nano Mater.* **2020**, *3*, 1166.
[277] F. Mahmood, H. Zhang, J. Lin, C. Wan, *ACS Omega* **2020**, *5*, 14611.
[278] S. Yang, Y. Ling, Q. Wu, H. Zhang, Z. Yan, G. Huang, J. Lin, C. Wan, *J. Mater. Chem. C* **2022**, *10*, 11730.
[279] J. Edberg, R. Brooke, O. Hosseinaei, A. Fall, K. Wijeratne, M. Sandberg, *npj Flex. Electron.* **2020**, *4*, 17.
[280] H. Park, M. Kim, B. G. Kim, Y. H. Kim, *ACS Appl. Nano Mater.* **2020**, *3*, 6899.
[281] B. Kulyk, B. F. R. R. Silva, A. F. Carvalho, S. Silvestre, A. J. S. A. J. S. Fernandes, R. Martins, E. Fortunato, F. M. Costa, *ACS Appl. Mater. Interfaces* **2021**, *13*, 10210.
[282] Y. Jung, J. Min, J. Choi, J. Bang, S. Jeong, K. R. Pyun, J. Ahn, Y. Cho, S. Hong, S. Hong, J. Lee, S. H. Ko, *Appl. Mater. Today* **2022**, *29*, 101589.

[283] N. Zhao, H. Zhang, S. Yang, Y. Sun, G. Zhao, W. Fan, Z. Yan, J. Lin, C. Wan, *Small* **2023**, *19*, 2300242.
[284] L. Shen, S. Zhou, B. Gu, S. Wang, S. Wang, *Adv. Eng. Mater.* **2023**, *25*, 2201882.
[285] P. I. C. Claro, A. C. Marques, I. Cunha, R. F. P. Martins, L. M. N. Pereira, J. M. Marconcini, L. H. C. Mattoso, E. Fortunato, *ACS Appl. Nano Mater.* **2021**, acsanm1c01453.
[286] B. Kulyk, M. Matos, B. F. R. Silva, A. F. Carvalho, A. J. S. Fernandes, D. V. Evtuguin, E. Fortunato, F. M. Costa, *Diam. Relat. Mater.* **2022**, *123*, 108855.
[287] J. Zikulnig, L. Neumaier, M. Lenzhofer, S. Carrara, J. Kosel, *IEEE Sensors Lett.* **2023**, *2*, 1.
[288] C. Larrigy, M. Burke, A. Imbrogno, E. Vaughan, C. Santillo, M. Lavorgna, L. Sygellou, G. Paterakis, C. Galiotis, D. Iacopino, A. J. Quinn, *Adv. Mater. Technol.* **2023**, *8*, 2201228.
[289] E. Vaughan, C. Santillo, A. Imbrogno, G. Gentile, A. J. Quinn, S. Kaciulis, M. Lavorgna, D. Iacopino, *ACS Sustain. Chem. Eng.* **2023**, *11*, 13574.
[290] T. Vićentić, I. Greco, C. S. Iorio, V. Miskovic, D. Bajuk-Bogdanovic, I. Pasti, K. Radulović, S. Klenk, T. Stimpel-Lindner, G. S. Duesberg, M. Spasenović, *Nanotechnology* **2023**, *35*, 115103.
[291] R. Miyakoshi, S. Hayashi, M. Terakawa, *Adv. Electron. Mater.* **2023**, *9*, 2201277.
[292] Y. Zhu, H. Cai, H. Ding, N. Pan, X. Wang, *ACS Appl. Mater. Interfaces* **2019**, *11*, 6195.
[293] S. Hayashi, F. Morosawa, M. Terakawa, *Adv. Eng. Mater.* **2021**, *23*, 2100457.
[294] P. Zaccagnini, C. Ballin, M. Fontana, M. Parmeggiani, S. Bianco, S. Stassi, A. Pedico, S. Ferrero, A. Lamberti, *Adv. Mater. Interfaces* **2021**, *8*, 2101046.
[295] Z. Li, L. Lu, Y. Xie, W. Wang, Z. Lin, B. Tang, N. Lin, *Adv. Eng. Mater.* **2021**, *23*, 2100195.
[296] Y. Li, Z. Zeng, S. Zhang, L. Yi, D. Guo, Y. Zhao, F. Liu, *Chem. Eng. J.* **2023**, *475*, 146330.
[297] M. Khandelwal, C. Van Tran, J. Bin In, *Appl. Surf. Sci.* **2022**, *576*, 151714.
[298] Y. J. Kim, D. Yang, H. K. Nam, T. S. D. Le, Y. Lee, S. Kwon, *CIRP Ann.* **2022**, *71*, 473.
[299] T. D. Le, Y. A. Lee, H. K. Nam, K. Y. Jang, D. Yang, B. Kim, K. Yim, S. Kim, H. Yoon, Y. Kim, *Adv. Funct. Mater.* **2021**, 2107768.
[300] Y. Lei, W. Zhao, Y. Zhu, U. Buttner, X. Dong, H. N. Alshareef, *ACS Nano* **2022**, acsnano1c06552.
[301] X. Sun, X. Liu, F. Li, *Appl. Surf. Sci.* **2021**, *551*, 149438.
[302] R. Funayama, S. Hayashi, M. Terakawa, *ACS Sustain. Chem. Eng.* **2023**, *11*, 3114.
[303] F. Mahmood, C. Zhang, Y. Xie, D. Stalla, J. Lin, C. Wan, *RSC Adv.* **2019**, *9*, 22713.
[304] M. Yuan, F. Luo, Z. Wang, J. Yu, H. Li, X. Chen, *Chem. Eng. J.* **2023**, *453*, 139898.
[305] M. Yuan, Z. Wang, Y. Rao, Y. Wang, B. Gao, J. Yu, H. Li, X. Chen, *Carbon N. Y.* **2023**, *202*, 296.
[306] Y. Yao, X. Duan, M. Niu, J. Luo, R. Wang, T. Liu, *Cellulose* **2019**, *26*, 7423.
[307] Y. Chyan, J. Cohen, W. Wang, C. Zhang, J. M. Tour, *ACS Appl. Nano Mater.* **2019**, *2*, 3007.
[308] M. Reynolds, L. M. Duarte, W. K. T. Coltro, M. F. Silva, F. J. V. Gomez, C. D. Garcia, *Microchem. J.* **2020**, *157*, 105067.
[309] Y. Kalachyova, O. Guselnikova, P. Postnikov, P. Fitl, L. Lapcak, V. Svorcik, O. Lyutakov, *RSC Adv.* **2018**, *8*, 11198.
[310] X. Wang, Y. Feng, K. Sun, N. Chai, B. Mai, S. Li, X. Chen, W. Zhao, Q. Zhang, *ENERGY Environ. Mater.* **2023**, 12650.
[311] Z. Luo, Y. Liu, Z. Liu, D. Wang, Z. Gan, C. Xie, *Nanotechnology* **2020**, *31*, 255301.
[312] N. Agarwal, H. Ryu, M. Mangang, W. Pfleging, J. Kim, *RSC Adv.* **2017**, *7*, 38565.
[313] C. Yun, J. W. Han, S. Kim, D. C. Lim, H. Jung, S.-H. Lee, J.-W. Jang, S. Yoo, K. Leo, Y. H. Kim, *Mater. Horizons* **2019**, *6*, 2143.
[314] T. Pflug, A. Anand, S. Busse, M. Olbrich, U. S. Schubert, H. Hoppe, A. Horn, *ACS Appl. Electron. Mater.* **2021**, *3*, 2825.
[315] D. Won, J. Kim, J. Choi, H. J. Kim, S. Han, I. Ha, J. Bang, K. K. Kim, Y. Lee, T. S. Kim, J. H. Park, C. Y. Kim, S. H. Ko, *Sci. Adv.* **2022**, *8*, 3209.
[316] Y. Wang, Y. Dou, Z. Wu, Y. Tian, Y. Xiong, J. Zhao, D. Fang, F. Huang, Y.-B. Cheng, J. Zhong, *Front. Chem. Sci. Eng.* **2023**, *17*, 206.
[317] M. Sharifuzzaman, M. A. Zahed, M. S. Reza, M. Asaduzzaman, S. H. Jeong, H. Song, D. K. Kim, S. Zhang, J. Y. Park, *Adv. Funct. Mater.* **2023**, *33*, 2208894.
[318] C. Hegde, C. H. J. Lim, T. H. Teng, D. Liu, Y. Kim, Q. Yan, H. Li, *Small* **2022**, *18*, 2203126.
[319] Q. Zhang, F. Zhang, X. Liu, Z. Yue, X. Chen, Z. Wan, *Adv. Mater. Technol.* **2023**, *8*, 2300244.
[320] X. Han, R. Ye, Y. Chyan, T. Wang, C. Zhang, L. Shi, T. Zhang, Y. Zhao, J. M. Tour, *ACS Appl. Nano Mater.* **2018**, *1*, 5053.
[321] S. J. Kang, J. J. Pak, *ChemElectroChem* **2022**, *9*, 202200328.
[322] X. Chen, Z. Hou, G. Li, W. Yu, Y. Xue, G. Niu, M. Xin, L. Yang, C. Meng, S. Guo, *Nano Energy* **2022**, *101*, 107606.
[323] H. Yang, S. Wang, Q. Huang, C. Tan, C. Gao, S. Xu, H. Ye, G. Zhang, *Appl. Surf. Sci.* **2023**, *636*, 157772.
[324] N. T. D. Thuy, G. Zhao, X. Wang, E. Awuah, L. Zhang, *Electroanalysis* **2023**, *35*, 202200194.
[325] H. Wang, P. Jiménez-Calvo, M. Hepp, M. A. Isaacs, C. Otieno Ogolla, I. Below-Lutz, B. Butz, V. Strauss, *ACS Appl. Nano Mater.* **2023**, *6*, 966.
[326] L. Yang, J. Yan, C. Meng, A. Dutta, X. Chen, Y. Xue, G. Niu, Y. Wang, S. Du, P. Zhou, C. Zhang, S. Guo, H. Cheng, *Adv. Mater.* **2023**, *35*, 2210322.
[327] W. Liu, Q. Chen, Y. Huang, D. Wang, L. Li, Z. Liu, *Carbon N. Y.* **2022**, *190*, 245.
[328] J. He, S. Wang, L. Jiang, X. Li, Q. Hong, W. Zhu, J. Sun, X. Zhang, Z. Xu, *Adv. Mater. Technol.* **2022**, *7*, 2200210.
[329] X. Yu, J. Zhang, N. Li, Y. Song, J. Kang, S. Zhang, C. Liu, Z. Li, J. Pu, N. Hong, M. Xi, Z. Wang, *J. Alloys Compd.* **2023**, *969*, 172435.
[330] R. Ma, H. Jiang, C. Wang, C. Zhao, H. Deng, *Chem. Commun.* **2020**, *56*, 2715.
[331] H. Jiang, S. Jin, C. Wang, R. Ma, Y. Song, M. Gao, X. Liu, A. Shen, G. J. Cheng, H. Deng, *J. Am. Chem. Soc.* **2019**, *141*, 5481.
[332] W. Zhang, R. Li, H. Zheng, J. Bao, Y. Tang, K. Zhou, *Adv. Funct. Mater.* **2021**, *31*, 2009057.
[333] X.-Y. Fu, Y.-Y. Zhang, C.-J. Ma, H.-B. Jiang, *Opt. Lett.* **2022**, *47*, 1502.
[334] S. Deshmukh, K. Ghosh, M. Pykal, M. Otyepka, M. Pumera, *ACS Nano* **2023**, *17*, 20537.
[335] Y. Yuan, X. Li, L. Jiang, M. Liang, X. Zhang, S. Wu, J. Wu, M. Tian, Y. Zhao, L. Qu, *Nat. Commun.* **2023**, *14*, 3967.
[336] K. K. Kim, J. Choi, J. Kim, S. Nam, S. H. Ko, *Adv. Funct. Mater.* **2022**, *32*, 2106329.
[337] J. Long, X. Chen, T. Mao, S. Xue, Y. Wang, Y. Xu, W. Pi, J. Lu, W. Luo, W. Xiong, *ACS Nano* **2022**, *17*.
[338] P. Zhao, G. Bhattacharya, S. J. Fishlock, J. G. M. Guy, A. Kumar, C. Tsonos, Z. Yu, S. Raj, J. A. McLaughlin, J. Luo, N. Soin, *Nano Energy* **2020**, *75*, 104958.
[339] H. Chen, W. Yang, P. Huang, C. Li, Y. Yang, B. Zheng, C. Zhang, R. Liu, Y. Li, Y. Xu, J. Wang, Z. Li, *Sustain. Energy Fuels* **2021**, *5*, 3737.
[340] N. Kamboj, B. B. Upreti, N. Kumar, R. S. Dey, *ACS Sustain. Chem. Eng.* **2023**, *11*, 5451.
[341] J. Žemgulytė, M. Sadauskas, P. Ragulis, R. Trusovas, K. Ratautas, R. Simniškis, Ž. Kancleris, G. Račiukaitis, *Sci. Rep.* **2023**, *13*, 22510.
[342] B. Clement, M. Lyu, E. Sandeep Kulkarni, T. Lin, Y. Hu, V. Lockett, C. Greig, L. Wang, *Engineering* **2022**, *13*, 238.

[343] H. Li, J. Liang, *Adv. Mater.* **2020**, *32*, 1805864.
[344] T. Delipinar, A. Shafique, M. S. Gohar, M. K. Yapici, *ACS Omega* **2021**, *6*, 8744.
[345] K. Singh, S. Sharma, S. Shriwastava, P. Singla, M. Gupta, C. C. Tripathi, *Mater. Sci. Semicond. Process.* **2021**, *123*, 105581.
[346] Z. E. Jeroish, K. S. Bhuvaneshwari, F. Samsuri, V. Narayanamurthy, *Biomed. Microdevices* **2022**, *24*, 3.
[347] E. Fortunato, P. Barquinha, R. Martins, *Adv. Mater.* **2012**, *24*, 2945.
[348] S. Dellis, I. Isakov, N. Kalfagiannis, K. Tetzner, T. D. Anthopoulos, D. C. Koutsogeorgis, K. Tetzner, T. D. Anthopoulos, D. C. Koutsogeorgis, *J. Mater. Chem. C* **2017**, *5*, 3673.
[349] P. J. Diemer, A. F. Harper, M. R. Niazi, A. J. Petty, J. E. Anthony, A. Amassian, O. D. Jurchescu, *Adv. Mater. Technol.* **2017**, *2*, 1.
[350] E. Carlos, S. Dellis, N. Kalfagiannis, L. Koutsokeras, D. C. Koutsogeorgis, R. Branquinho, R. Martins, E. Fortunato, *J. Mater. Chem. C* **2020**, *8*, 6176.
[351] A. Perinot, P. Kshirsagar, M. A. Malvindi, P. P. Pompa, R. Fiammengo, M. Caironi, *Sci. Rep.* **2016**, *6*, 38941.
[352] A. Perinot, M. Giorgio, V. Mattoli, D. Natali, M. Caironi, *Adv. Sci.* **2021**, *8*, 2001098.
[353] U. Zschieschang, H. Klauk, J. W. Borchert, *Adv. Mater. Technol.* **2023**, *8*, 2201888.
[354] D. B. Strukov, G. S. Snider, D. R. Stewart, R. S. Williams, *Nature* **2008**, *453*, 80.
[355] R. A. Martins, E. Carlos, J. Deuermeier, M. E. Pereira, R. Martins, E. Fortunato, A. Kiazadeh, *J. Mater. Chem. C* **2022**, *10*, 1991.
[356] E. Carlos, R. Branquinho, R. Martins, A. Kiazadeh, E. Fortunato, *Adv. Mater.* **2021**, *33*, 2004328.
[357] H.-K. Kim, J.-H. Bae, T.-H. Kim, K.-W. Song, C.-W. Yang, *Appl. Microsc.* **2012**, *42*, 207.
[358] Y. Dai, H. Wang, H. Tao, W. Li, W. Li, C. Yang, *Phys. E Low-dimensional Syst. Nanostructures* **2019**, *114*, 113577.
[359] F. J. Romero, A. Toral-Lopez, A. Ohata, D. P. Morales, F. G. Ruiz, A. Godoy, N. Rodriguez, *Nanomaterials* **2019**, *9*, 897.
[360] M. Chen, Z. Wan, H. Dong, Q. Chen, M. Gu, Q. Zhang, *Natl. Sci. Open* **2022**, *1*, 20220020.
[361] S. W. Han, M. W. Shin, *J. Alloys Compd.* **2022**, *908*, 164658.
[362] P. K. Enaganti, A. Kothuru, S. Goel, *J. Mater. Res.* **2022**, *37*, 3976.
[363] R. Roges, P. K. Malik, *Int. J. Commun. Syst.* **2021**, *34*, e4940.
[364] O. R. Alobaidi, P. Chelvanathan, S. K. Tiong, B. Bais, M. A. Uzzaman, N. Amin, *IEEE Access* **2022**, *10*, 12286.
[365] S. G. Kirtania, A. W. Elger, M. R. Hasan, A. Wisniewska, K. Sekhar, T. Karacolak, P. K. Sekhar, *Micromachines* **2020**, *11*, 847.
[366] C. Yang, M.-C. Chou, T.-H. Kao, M.-C. Huang, in 2018 13th Int. Congr. Molded Interconnect Devices, IEEE, Piscataway, NJ **2018**, pp. 1–6.
[367] M. R. R. Abdul-Aziz, S. A. Mohassieb, N. A. Eltresy, M. M. K. Yousef, B. Anis, S. O. Abdellatif, A. S. G. Khalil, *IEEE Trans. Nanotechnol.* **2020**, *19*, 269.
[368] A. Rivadeneyra, J. F. Salmeron, N. Rodriguez, D. P. Morales, R. Colella, F. P. Chietera, L. Catarinucci, in *2020 50th Eur. Microw. Conf.*, IEEE, Piscataway, NJ **2021**, pp. 812–815.
[369] F. P. Chietera, R. Colella, A. Verma, E. Ferraris, C. E. Corcione, C. L. Moraila-Martinez, D. Gerardo, Y. H. Acid, A. Rivadeneyra, L. Catarinucci, *IEEE J. Radio Freq. Identif.* **2022**, *6*, 601.
[370] A. Mostaccio, G. Antonelli, C. Occhiuzzi, E. Martinelli, G. Marrocco, 2022 IEEE 12th Int. Conf. RFID Technol. Appl. RFID-TA 2022, IEEE, Piscataway, NJ **2022**, p. 51.
[371] B. Sindhu, A. Kothuru, P. Sahatiya, S. Goel, S. Nandi, *IEEE Trans. Electron Devices* **2021**, *68*, 3189.
[372] M. Ahmad, G. Cantarella, M. A. C. Angeli, M. Madagalam, C. Ebner, M. Ciocca, R. Riaz, P. Ibba, M. Petrelli, I. Merino, N. Cohen, P. Lugli, L. Petti, in *2021 IEEE Int. Flex. Electron. Technol. Conf.* , IEEE, Piscataway, NJ **2021**, pp. 0044–0046.
[373] S. Liu, M. C. Yuen, E. L. White, J. W. Boley, B. Deng, G. J. Cheng, R. Kramer-Bottiglio, *ACS Appl. Mater. Interfaces* **2018**, *10*, 28232.
[374] M. Tsukamoto, R. Nishii, Y. Muraki, T. Shinonaga, M. Yoshida, M. Takahashi, N. Abe, *Appl. Surf. Sci.* **2014**, *313*, 730.
[375] G. Liu, Y. Gao, S. Xu, T. Bu, Y. Xie, C. Xu, H. Zhou, Y. Qi, C. Zhang, *EcoMat* **2021**, *3*, 12130.
[376] S. Korkmaz, İ. A. Kariper, *Synth. Met.* **2021**, *273*, 116692.
[377] M. Salauddin, S. S. Rana, M. Sharifuzzaman, S. H. Lee, M. A. Zahed, Y. Do Shin, S. Seonu, H. S. Song, T. Bhatta, J. Y. Park, *Nano Energy* **2022**, *100*, 107462.
[378] Y. Chen, B. Xie, J. Long, Y. Kuang, X. Chen, M. Hou, J. Gao, S. Zhou, B. Fan, Y. He, Y. Zhang, C. Wong, Z. Wang, N. Zhao, *Adv. Mater.* **2021**, *33*, 2104290.
[379] P. Yadav, N. Sanna Kotrappanavar, P. B. Naik, H. K. Beere, K. Samanta, N. S. Reddy, J. S. Algethami, M. Jalalah, F. A. Harraz, D. Ghosh, *ACS Appl. Energy Mater.* **2023**, *6*, 1799.
[380] H. Hu, H. Li, Z. Zhang, W. Chen, J. Wang, L. Lian, W. Yang, L. He, Y.-F. Song, *ACS Appl. Mater. Interfaces* **2023**, *15*, 45725.
[381] Z. Li, L. Deng, T. Wei, H. Zhao, C. Wang, X. Wei, *Appl. Surf. Sci.* **2023**, *639*, 158219.
[382] P. Yadav, P. B. Naik, H. K. Beere, N. S. Reddy, K. Samanta, N. Sanna Kotrappanavar, J. S. Algethami, M. Faisal, F. A. Harraz, D. Ghosh, *Langmuir* **2022**, *38*, 16203.
[383] M. Ren, J. Zhang, M. Fan, P. M. Ajayan, J. M. Tour, *Adv. Mater. Interfaces* **2019**, *6*, 1901035.
[384] W. Pfleging, *Nanophotonics* **2018**, *7*, 549.
[385] J. Shang, C. Xu, Q. Wang, S. Wang, J. Chen, X. Wang, *ACS Appl. Energy Mater.* **2022**, *5*, 12427.
[386] S. Aslam, R. U. R. Sagar, Y. Liu, T. Anwar, L. Zhang, M. Zhang, N. Mahmood, Y. Qiu, *Appl. Mater. Today* **2019**, *17*, 123.
[387] W. Zhang, W. Yan, H. Jiang, C. Wang, Y. Zhou, F. Ke, H. Cong, H. Deng, *ACS Sustain. Chem. Eng.* **2020**, *8*, 335.
[388] H. Xiao, Y. Li, W. Chen, T. Xie, H. Zhu, W. Zheng, J. He, S. Huang, *Small* **2023**, *19*, 2303959.
[389] H. Liu, Z. Sun, Y. Chen, W. Zhang, X. Chen, C.-P. Wong, *ACS Nano* **2022**, *16*, 10088.
[390] X. Wang, Q. Zhang, *J. Energy Storage* **2021**, *34*, 101994.
[391] L. Lu, D. Zhang, Y. Xie, W. Wang, *J. Energy Storage* **2022**, *51*, 104458.
[392] X. Sun, X. Hou, X. Mei, Y. Han, B. Liu, Q. Li, Z. Wang, W. Tang, Y. Wu, W. Wang, J. Cui, *ACS Sustain. Chem. Eng.* **2023**, *11*, 7357.
[393] C. Zhu, X. Dong, X. Mei, M. Gao, K. Wang, D. Zhao, *J. Mater. Sci.* **2020**, *55*, 17108.
[394] R. Xu, Z. Wang, L. Gao, S. Wang, J. Zhao, *Appl. Surf. Sci.* **2022**, *571*, 151385.
[395] G. Yuan, T. Wan, A. BaQais, Y. Mu, D. Cui, M. A. Amin, X. Li, B. Bin Xu, X. Zhu, H. Algadi, H. Li, P. Wasnik, N. Lu, Z. Guo, H. Wei, B. Cheng, *Carbon N. Y.* **2023**, *212*, 118101.
[396] S. P. Singh, Y. Li, J. Zhang, J. M. Tour, C. J. Arnusch, *ACS Nano* **2018**, *12*, 289.
[397] S. Hwang, T. Hwang, H. Kong, S. Lee, J. Yeo, *Appl. Surf. Sci.* **2021**, *552*, 149382.
[398] J. Lee, J. Y. Seok, S. Son, M. Yang, B. Kang, *J. Mater. Chem. A* **2017**, *5*, 24585.
[399] J. Tang, W. Yi, X. Zhong, C. (John) Zhang, X. Xiao, F. Pan, B. Xu, *Energy Storage Mater.* **2020**, *32*, 418.
[400] F. P. García de Arquer, A. Armin, P. Meredith, E. H. Sargent, *Nat. Rev. Mater.* **2017**, *2*, 16100.
[401] J. Chen, J. Zhu, P. Li, X. M. Wu, R. Liu, J. Wan, T. L. Ren, *IEEE Trans. Electron Devices* **2021**, *68*, 4485.
[402] J. Chen, Q. Wang, Y. Sheng, G. Cao, P. Yang, Y. Shan, F. Liao, Z. Muhammad, W. Bao, L. Hu, R. Liu, C. Cong, Z.-J. Qiu, *ACS Appl. Mater. Interfaces* **2019**, *11*, 43330.
[403] H. Liu, H. Xiang, Z. Li, Q. Meng, P. Li, Y. Ma, H. Zhou, W. Huang, *ACS Sustain. Chem. Eng.* **2020**, *8*, 527.

[404] S. Cui, Y. Lu, D. Kong, H. Luo, L. Peng, G. Yang, H. Yang, K. Xu, *Opto-Electronic Adv.* **2023**, *6*, 220172.
[405] L. Zhu, X. Li, T. Kasuga, K. Uetani, M. Nogi, H. Koga, *J. Mater. Chem. C* **2022**, *10*, 3712.
[406] X. Liu, Y. Wei, Y. Qiu, *Micromachines* **2021**, *12*, 695.
[407] Y. Li, Y. Wei, Y. Yang, L. Zheng, L. Luo, J. Gao, H. Jiang, J. Song, M. Xu, X. Wang, W. Huang, *Research* **2022**, *2022*, 0002.
[408] H. Zhang, W. Han, K. Xu, H. Lin, Y. Lu, H. Liu, R. Li, Y. Du, Z. Nie, F. Xu, L. Miao, J. Zhu, W. Huang, *Adv. Funct. Mater.* **2021**, *31*, 2009466.
[409] B. Nie, R. Huang, T. Yao, Y. Zhang, Y. Miao, C. Liu, J. Liu, X. Chen, *Adv. Funct. Mater.* **2019**, *29*, 1808786.
[410] M. Xie, M. Zhu, Z. Yang, S. Okada, S. Kawamura, *Nano Energy* **2021**, *79*, 105438.
[411] L.-Y. Hsiao, L. Jing, K. Li, H. Yang, Y. Li, P.-Y. Chen, *Carbon N. Y.* **2020**, *161*, 784.
[412] G. Liu, Z. Zhang, Z. Li, L. Guo, L. Ning, *2D Mater.* **2023**, *10*, 022002.
[413] M. Parmeggiani, S. Stassi, M. Fontana, S. Bianco, F. Catania, L. Scaltrito, A. Lamberti, *Smart Mater. Struct.* **2021**, *30*, 105007.
[414] W. Liu, Y. Huang, Y. Peng, M. Walczak, D. Wang, Q. Chen, Z. Liu, L. Li, *ACS Appl. Nano Mater.* **2020**, *3*, 283.
[415] A. M. Baracu, L. A. Dinu Gugoasa, *J. Electrochem. Soc.* **2021**, *168*, 037503.
[416] A. A. Lahcen, S. Rauf, T. Beduk, C. Durmus, A. Aljedaibi, S. Timur, H. N. Alshareef, A. Amine, O. S. Wolfbeis, K. N. Salama, *Biosens. Bioelectron.* **2020**, *168*, 112565.
[417] G. Ren, H. Fan, L. Zhang, S. He, C. Zhu, K. Gao, Y. Zhang, J. Wang, X. Kang, Y. Song, Z. Gong, G. Li, G. Lu, H. D. Yu, *J. Mater. Chem. C* **2023**, *11*, 4916.
[418] M. Nazeri, M. Ghalamboran, G. Grau, *Adv. Mater. Technol.* **2023**, *8*, 2300188.
[419] Y. Luo, M. R. Abidian, J.-H. Ahn, D. Akinwande, A. M. Andrews, M. Antonietti, Z. Bao, M. Berggren, C. A. Berkey, C. J. Bettinger, J. Chen, P. Chen, W. Cheng, X. Cheng, S.-J. Choi, A. Chortos, C. Dagdeviren, R. H. Dauskardt, C. Di, M. D. Dickey, X. Duan, A. Facchetti, Z. Fan, Y. Fang, J. Feng, X. Feng, H. Gao, W. Gao, X. Gong, C. F. Guo, et al., *ACS Nano* **2023**, *17*, 5211.
[420] Y. Yang, Y. Song, X. Bo, J. Min, O. S. Pak, L. Zhu, M. Wang, J. Tu, A. Kogan, H. Zhang, T. K. Hsiai, Z. Li, W. Gao, *Nat. Biotechnol.* **2020**, *38*, 217.
[421] J. Tu, J. Min, Y. Song, C. Xu, J. Li, J. Moore, J. Hanson, E. Hu, T. Parimon, T.-Y. Wang, E. Davoodi, T.-F. Chou, P. Chen, J. J. Hsu, H. B. Rossiter, W. Gao, *Nat. Biomed. Eng.* **2023**, *7*, 1293.
[422] R. M. Torrente-Rodríguez, J. Tu, Y. Yang, J. Min, M. Wang, Y. Song, Y. Yu, C. Xu, C. Ye, W. W. IsHak, W. Gao, *Matter* **2020**, *2*, 1.
[423] M. Wang, Y. Yang, J. Min, Y. Song, J. Tu, D. Mukasa, C. Ye, C. Xu, N. Heflin, J. S. McCune, T. K. Hsiai, Z. Li, W. Gao, *Nat. Biomed. Eng.* **2022**, *6*, 1225.
[424] R. M. Torrente-Rodríguez, H. Lukas, J. Tu, C. Xu, H. B. Rossiter, W. Gao, *Matter* **2020**, *3*, 1981.
[425] T. Tabata, F. Rozé, L. Thuries, S. Halty, P.-E. Raynal, I. Karmous, K. Huet, *Electronics* **2022**, *11*, 2636.
[426] L. Yang, F. Mayer, U. H. F. Bunz, E. Blasco, M. Wegener, *Light Adv. Manuf.* **2021**, *2*, 1.
[427] L. Li, in *Advances in Laser Materials Processing*, Elsevier, Cham **2010**, pp. 20–39.

**Tomás Pinheiro** obtained his B.E. (2016) and M.S. (2018) degrees in Biomedical Engineering from Nova School of Science and Technology, Lisbon, Portugal. He is currently a Ph.D. student in Nanoscience and Nanotechnology program in the Materials Science Department. His research interests include laser-material processing for bioelectronics and wearable device research, plasmonic and electrochemical biosensors, and integrated bioelectronics systems for health.

**Elvira Fortunato** full professor at FCT-NOVA, former Minister of Science Technology and Higher Education of Portugal; former vice-rector at NOVA University of Lisbon; subdirector of the Materials Research Center CENIMAT and of the Associated Laboratory i3N, the Institute of Nanostructures, Nanomodeling and Nanofabrication and QiuShi Chair Visiting Professor at Zhejiang University. She is an elected member of the Academy of Engineering, the European Academy of Sciences, the Lisbon Academy of Sciences, and Academia Europaea. Elvira Fortunato is among the 20 Hidden Inventors of Europe due to her work on transparent electronics and paper electronics. Her list of prizes and distinctions awarded is outstanding, going above 30 from which we highlight Advanced Material Frontier Award (2022), WFEO GREE International Engineering Prize (2022); Career and Scientific Merit Award Given by the Portuguese Materials Research Society (2022); Human Rights by the Portuguese Parliament (2021); FEMS Materials Innovation Prize (2021); PESSOA Prize (the highest science Portuguese distinction 2021); Horizon Impact Award 2020, 2017 Czochralski award 2016 Blaise Pascal Medal by the European Academy of Sciences, among others.

**Rodrigo Martins** is full professor at FCT-NOVA, director of the Materials Research Center (CENIMAT) and of the Associated Laboratory i3N, the Institute of Nanostructures, Nanomodeling and Nanofabrication; president of the European Academy of Sciences; former President of International Union of Materials Research Society - IUMRS; former Member of the Scientific Council of the European Research Council; President of the administration board of the Portuguese cluster in Advanced Materials (NANOMAT); member of the administration board of the Portuguese cluster on Batteries (BatPower); Chair of the European Committee Affairs of European Materials Research Society. Member of the committee of King Jaume I award for Basic Research. He is a member of the Portuguese Academy of Engineering and of the Portuguese Order of Engineers, OE, and of the Board of Admission and Qualification of OE. QiuShi Chair Visiting Professor at Zhejiang University; Honorary Professor of Heife Institutes of Physical Sciences of the Chinese Academy of Sciences (CAS); Honorary Professor of the Technical University of Wuhan. In 2023 selected as PIFI Distinguished Scientist of Chinese Academy of Sciences, the highest honour for overseas talents. He got more than 15 distinctions and awards. In 2021 he got the Career and Recognition Award given by the Portuguese Society of Materials and the Research Nova-Altice Award.